



Thermally Activated Delayed Fluorescence Emitters based on a DioxaBoranaphthaAnthracene (DBA) Acceptor Unit

Master Thesis

by

Marvin Manz

Born on 9th November 1996

In Worms

Mainz, August 2023

This thesis was written between 03/01/2023 and 08/31/2023 at the Max Planck Institute for Polymer Research (MPI-P) in Mainz under the supervision of Dr. Jasper Michels and Dr. Yungui Li, in the Molecular Electronics Division, headed by Prof. Dr. Paul Blom. The presented results were obtained in cooperation with Oskar Sachnik and Xin Zhou and are jointly used.

First supervisor: Dr. Jasper Michels

Second supervisor: Prof. Dr. Sebastian Seiffert

**Masterarbeit im Studiengang Chemie oder Biomedizinische Chemie
an der Johannes Gutenberg - Universität Mainz**

Ich, Marvin Manz, Matrikelnummer 2729474
versichere, dass ich meine Masterarbeit selbstständig verfasst und keine anderen als
die angegebenen schriftlichen und elektronischen Quellen sowie andere Hilfsmittel
benutzt habe. Alle Ausführungen, die anderen Schriften wörtlich oder sinngemäß
entnommen wurden, habe ich kenntlich gemacht.

Alzey, 31.08.2023
(Ort, Datum)

M. Manz
(Unterschrift)

Acknowledgments

First of all, I'd like to thank Prof. Dr. Paul Blom for giving me the opportunity to do my Master Thesis in his working group and granting me the chance to gain a better understanding of the field of organic semiconductors.

Furthermore, I'd like to thank Dr. Jasper Michels for supervising my work and helping me with challenges I had to face.

I'd like to thank Prof. Dr. Sebastian Seiffert for accepting my request for second supervision to take his time to read and evaluate my work.

I'd also love to give special props to Oskar Sachnik, who took care of me during my work and always took his time to help me, give me introductions, show me how to process and evaluate data and so much more. Even though he had so much work to do himself, I could always ask him for advice. Thank you very much, Oskar, you are a wonderful person.

Apart from that, I'd also like to thank Xin Zhou who helped me with any kind of photophysical experiment. Thank you for taking your time to show me how to do the experiments and how to evaluate the data!

Moreover, I'd also like to thank Dr. Yungui Li, Xiao Tan, David Trieb for helping me with different measurement setups. Then, I'd like to thank the technicians Sirma Koynova, Michelle Beuchel, Christian Bauer and Frank Keller who were always providing help. And I'd like to thank everybody of the working group for always being friendly, helpful and providing a very pleasing and healthy working environment.

Last but not least, I'd like to thank my entire family: my mother Ursula, my father Bernd, my brother Aron, my aunt Inge, my grandmother Anneliese and my girlfriend Antonia. They are always there for me when I need help, have time for me, support me with my decisions and never let me down.

Contents

1. Introduction	2
2. Motivation	4
3. Theory	7
3.1. Organic Light-Emitting Diodes (OLEDs).....	7
3.1.1. Basic Functioning of an OLED	7
3.1.2. Multi-layer OLEDs	10
3.1.3. Single-layer OLEDs	11
3.1.4. Single-Carrier Devices (Electron-Only EO and Hole-Only HO).....	12
3.2. Development of Materials in OLEDs.....	15
3.2.1. Fluorescent Materials	15
3.2.2. Phosphorescent Materials	15
3.2.3. TADF Materials	16
4. Results and Discussion	19
4.1. Theoretical TD-DFT (time-dependent density-functional theory) simulations.....	19
4.1.1. Singlet and Triplet Energy Levels and (ΔEST)	19
4.1.2. Synthetic route	20
4.1.3. HOMO and LUMO Energies.....	21
4.2. Photophysical Properties	23
4.2.1. UV/Vis Absorption and Emission	23
4.2.2. Solvatochromism	25
4.2.3. Time-resolved photoluminescence (TRPL).....	26
4.2.4. Ellipsometry.....	27
4.2.5. Angular Dependency.....	28
4.3. Device Characteristics.....	28
4.3.1. Electron- and Hole-only Devices.....	28
4.3.2. OLED Devices	29
5. Summary and Conclusion	33
6. Experimental Part	35
6.1. Synthesis	35
6.2. Methods.....	38
7. References	40
8. List of Figures	45
9. List of Tables	46
10. Appendix.....	47
11. Deutsche Zusammenfassung.....	59

List of Abbreviations

CT	Charge-Transfer
DF	Delayed Fluorescence
DFT	Density Function Theory
EA	Electron Affinity
EBL	Electron-Blocking Layer
EIL	Electron-Injection Layer
EML	Emissive Layer
EO	Electron-only
EQE	External Quantum Yield
ETL	Electron-Transporting Layer
FWHM	Full Width at half Maximum
HBL	Hole-Blocking Layer
HIL	Hole-Injection Layer
HO	Hole-only
HOMO	Highest Occupied Molecular Orbital
HTL	Hole-Transporting Layer
IE	Ionization Energy
IQE	Internal Quantum Yield
ISC	Intersystem Crossing
ITO	Indium Tin Oxide
LCD	Liquid Crystal Display
LUMO	Lowest Unoccupied Molecular Orbital
MR-TADF	Multi-Resonance Thermally Activated Delayed Fluorescence
NMR	Nuclear Magnetic Resonance
OLED	Organic Light-Emitting Diode
PF	Prompt Fluorescence
rISC	Reverse Intersystem Crossing
SOC	Spin-Orbit Coupling
SPP	Surface Plasmon Polariton
TADF	Thermally Activated Delayed Fluorescence
TD-DFT	Time-Dependent Density Function Theory
TDM	Transition Dipole Moment
TRPL	Time-Resolved Photoluminescence

1. Introduction

Organic light-emitting diodes (OLEDs) have been commercialized for application in smartphones, flat panel displays and solid-state lighting technology and thus have become an indispensable part of our everyday lives. The conventional liquid crystal display (LCD) technology has been used in computer and TV screens, being the commercial market leader since 2007.^[1] In comparison to LCD, OLEDs exhibit several advantages: The pixels within an OLED screen are self-emitting. Therefore, no background lighting is needed as in a LCD screen. This yields not only a lower power consumption but also a higher contrast and a better color purity.^[2] Moreover, OLEDs are produced more environmentally friendly and cheaper than LCD screens.^[3] Nowadays, more energy-efficient light-emitting diodes (LEDs) are also widely used for lighting, gradually replacing the light bulb.^[4,5] The extraction of silicon for the use in inorganic LEDs and LCDs has a high energy consumption and therefore is economically unfavorable. However, it also is environmentally harmful because one ton of silicon produces up to 900 kg dust waste that damage the environment and has a negative effect on human health, especially on respiratory organs.^[6] As a result, a more environmentally friendly technology is desired.

Among different technologies, OLED is one of the most promising candidates for the next generation lighting and display applications. However, at the moment, the organic LED is not fully developed yet and cannot compete with its inorganic counterpart in efficiency and stability.^[7] In order to compete with LCDs and inorganic LEDs, OLED research has come a long way: In OLEDs, a crucial parameter is the internal quantum efficiency (IQE) which is limited to 25% in conventional fluorescence-based OLEDs, because under electrical excitation only one of four excitations leads to a singlet exciton that can be harvested.^[8,9] The other 75% of electrically generated energy is dissipated as heat and recombine via non-radiative processes. Therefore, the development of phosphorescent emitters has significantly enhanced the device efficiency.^[10] The utilization of phosphorescent emitters containing heavy metals (Ir, Pt, Os, and Au) in the organic aromatic frameworks enhances the intersystem crossing (ISC) and the following triplet radiation by strong spin-orbit coupling (SOC).^[9,11] As a result, not only singlet excitons but also triplet excitons can be harvested, leading to IQEs of up to 100%.^[11,12] However, the latter comes along with the major drawbacks of a high cost, limited global resources and toxicity of the heavy metals. Meanwhile, the lifetimes of blue phosphorescent OLEDs (PhOLEDs) are shorter compared to green and red devices due to weak metal-ligand coordination bonds.^[13-15] To overcome this challenge, purely organic aromatic compounds with a small energy gap ΔE_{ST} between the lowest singlet and triplet state were used as emitters.^[16] These can transfer non-radiative triplet excitons to emissive singlet excitons by a reverse intersystem crossing (rISC) process that is assisted by thermal energy. This will be explained in detail in Chapter 3. Such compounds are referred to as thermally activated delayed fluorescence (TADF) materials. Typically, such materials are obtained via a structure containing an electron donor (D) and an electron acceptor (A) moiety with a small energy difference between T_1 and S_1 of well below 0.1 eV. On a molecular basis, this can be achieved by separating the highest occupied molecular orbital (HOMO) and lowest unoccupied molecular orbital (LUMO). This is a prerequisite for obtaining a TADF material with low ΔE_{ST} that enables the fabrication of cost-effective OLEDs that can also reach an IQE of up to 100%.^[16] Figure 1.1 displays the structure of 5-(5,9-dioxa-13b-boranaphtho[3,2,1-de]anthracen-7-yl)-10,15-diphenyl-10,15-dihydro-5H-diindolo[3,2- α :3',2'-c]carbazole (DI-DBA) and its electron density distribution for the HOMO and LUMO. It can be observed that the LUMO is located on the acceptor (DioxaBoranaphthoAnthracene DBA) moiety whereas the HOMO is located on the donor (diphenyl-dihydro-DiIndolo-carbazol) moiety. This behavior is typical for the frontier molecular orbitals of a TADF emitter.

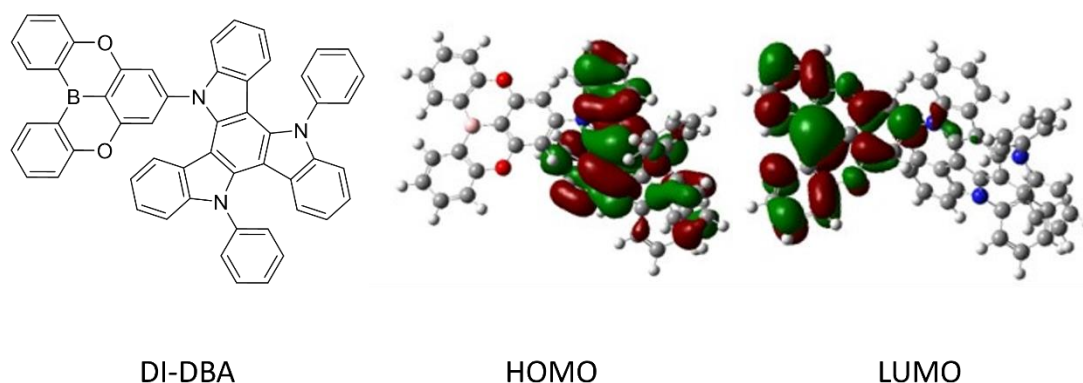


Figure 1.1. DI-DBA molecule and electron density for HOMO and LUMO orbital.

The spatial separation of HOMO and LUMO leads to a TADF-typical property: The positive solvatochromism in solution, meaning a bathochromic shift in the emission with increasing solvent polarity. This is caused by a positive solvatochromic effect and is primarily a result of different dielectric constants of different solvent molecules. These exhibit different effects on the electronic ground state as well as on the excited states of the solute.^[17,18] This yields a spectral shift of the emission because the solute exhibits different dipole moments for ground and excited state which arises from the redistribution of electronic density in an excited state of charge-transfer (CT) character.^[18,19] Therefore, the solvatochromism can also be used as evidence for the presence of CT states. Another characteristic of the emission from excited states with a CT-character is that the spectrum is well resolved for low-polarity solvents because apolar solvents stabilize locally excited (LE) states rather than CT states. Therefore, the CT is less simply pronounced in an apolar solvent. However with increasing solvent polarity, the spectrum becomes increasingly structureless approaching a Gaussian shape because the CT states are stabilized and not the LE states.^[20]

The discovery of TADF happened in 1961, when the first purely organic TADF material eosin Y dye was found.^[21] Almost twenty years later in 1980, TADF was observed in a metal-containing material, a Cu(I)-complex.^[22] Since the pioneering work for the application of purely organic molecules in photoelectric devices in 1987, impressive progress has been made.^[23] The first reported attempt to apply TADF materials in OLEDs appeared in 2009 with Sn⁴⁺-porphyrin complexes.^[24] Back then, the device required a rather high onset of current injection around 10 V. The research on TADF OLEDs climaxed in 2012 after the work of Adachi and co-workers, who synthesized metal-free highly efficient TADF molecules, reaching a comparable performance to the best reported PhOLEDs.^[16]

Conventional multi-layer OLED devices are widely used as they are stable and efficient.^[25] However, in such a device, many different layers are incorporated, which leads to higher costs and longer time in their production. Recently, our research group fabricated an efficient and long-living OLED based on the TADF material 5,10-Bis(4-(9H-carbazol-9-yl)-2,6-dimethylphenyl)-5,10-dihydroboranthrene (CzDBA) in an unconventional single-layer device configuration.^[26] In this device architecture, the widely used electron and hole blocking and transport layers, as well as co-evaporated guest-host layers are not needed.^[26–28] A neat film of CzDBA (75 nm) was sandwiched between two Ohmic contacts,^[29,30] which yields a device with a maximum external quantum efficiency of 19%.^[26]

A detailed comparison between a conventional multi-layer OLED and a single-layer OLED device will be provided in Chapter 3 (compare Figure 3.5 and Figure 3.7).

In this work, exclusively single-layer OLEDs are fabricated and analyzed. For this approach, an EML (95 nm) is evaporated on top of an indium tin oxide (ITO) substrate with a spin-coated layer of Poly(3,4-ethylenedioxythiophene): polystyrene sulfonate: perfluorinated ionomer (PEDOT:PSS:PFI). The used PFI forms an Ohmic contact with the emitter, which replaces any other layer and greatly simplifies the architecture of the device. On top of an evaporated EML, a thin interlayer of 2,2',2''-(1,3,5-Benzinetriyl)-tris(1-phenyl-1-H-benzimidazole (TPBi) (4 nm) was evaporated to form an Ohmic contact with the Al cathode (100 nm).^[26]

2. Motivation

It is essential to investigate the effect of emitter design and structure on photophysical and device properties in order to understand the structure–property relation and then be able to molecularly modify and synthesize blue emitters for the use in OLEDs. Therefore, studies on the electronic and photophysical properties of TADF molecules are indispensable. Recently, electron-deficient boron-based acceptor units in blue TADF materials have been researched due to their excellent photophysical and electrochemical properties and electron-accepting character as the vacant p -orbital of the boron atom leads to its electron-deficient Lewis acidic nature.^[31] This electron-deficient boron enables a three-coordinate boron acceptor moiety to interact through its empty p_z orbital with the π -orbital of a carbon-carbon conjugated bond. This is schematically presented in Figure 2.1.

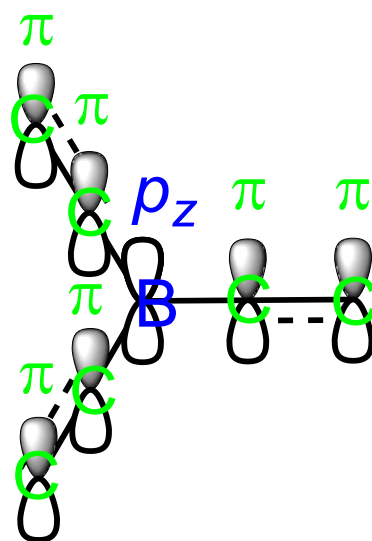


Figure 2.1. Simplified bondage configuration of p_z - π conjugation of B–C bond in organic conjugated π -systems.

As the boron exhibits an sp^2 hybridized trigonal planar geometry, yielding a rigid molecular structure, non-radiative decay is suppressed in these materials.^[32–34] In general, boron-based emitters exhibit a blue emission because of their large band gap that comes from their weak acceptor nature. Even though, by molecular design strategies, different color emissions from blue to red depending on the acceptor moiety could be achieved.^[35,36] This shows the great potential of boron-based acceptor moieties in TADF emitters. As a result, many TADF materials with boron-based acceptors and good device performances have been reported.

To achieve a narrower emission spectrum and therefore a better color purity, new molecular design approaches based on the multi-resonance (MR) effect are used to obtain a high external quantum efficiency (EQE) (for further explanation see Chapter 3.1.3) with an ultrapure blue or green emission in a TADF molecule (MR-TADF).^[37,38] The molecule consists of a triphenyl boron species that was rigidified with heteroatoms (Nitrogen/Oxygen) containing phenyl groups to construct a rigid polycyclic aromatic framework (see Figure 2.2).^[38] In this rigid structure that is typical for a MR-TADF material, HOMO and LUMO could be separated due to the opposite resonance effects of boron and nitrogen atoms in the backbone structure.^[38] As a result, a TADF material is obtained without the necessity of an electron donating and an electron withdrawing moiety. This way, a high EQE of up to 34.4% for the blue TADF emitter (doped in a host matrix) with a very small FWHM of 18 nm could be achieved through structural modifications. Since conventional blue TADF emitters cannot provide long enough

device lifetimes for commercial applications, boron-based rigid molecular designs have excellent potential to provide stable, efficient but also color-pure TADF emitters.

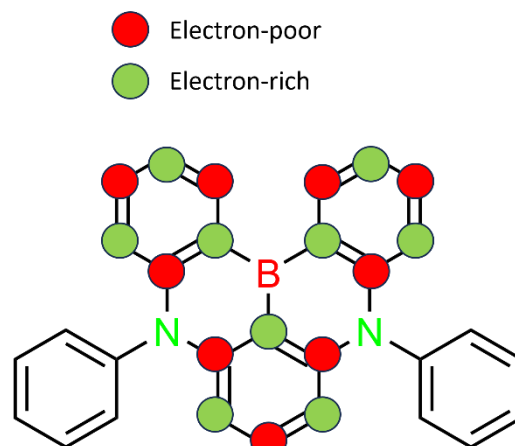


Figure 2.2. Principle of MR-TADF compounds.

The aim of this work is the synthesis, investigation of structure-property relations and comparison of different blue emitting TADF materials sharing the same 5-(5,9-dioxa-13*b*-boranaphtho[3,2,1-*de*]anthracen-7-yl) (DBA) acceptor moiety that is quite similar to the MR-TADF material in Figure 2.2. This acceptor moiety paired with a suitable donor moiety exhibited an exceptional EQE of 28% in a doped OLED device.^[39] Figure 2.3 displays the molecular structures of the TADF materials studied in this project. The 5-(5,9-dioxa-13*b*-boranaphtho[3,2,1-*de*]anthracen-7-yl)-10,15-diphenyl-10,15-dihydro-5*H*-diindolo[3,2-*a*:3',2'*c*]carbazole (DI-DBA) was commercially obtained whereas the 10-(5,9-dioxa-13*b*-boranaphtho[3,2,1-*de*]anthracen-7-yl)-10*H*-spiro[acridine-9,9'-fluorene (SpiroAc-DBA) as well as the 9-[1,4]Benzoxaborino[2,3,4-*kl*]phenoxaborin-7-yl-1,3,6,8-tetramethyl-9*H*-carbazole (TMCz-DBA) were synthesized. As Figure 2.3 points out, the three blue MR-TADF emitters share the same acceptor moiety with the donor moiety being varied. The DI-DBA has a large π -system containing three carbazole units around the same phenyl ring with one carbazole-nitrogen being connected to the acceptor moiety and the other two to phenyl groups. The TMCz-DBA has only one carbazole as donor moiety but with additional methyl groups in 1,3 and 6,8 positions. These enable better spatial separation of HOMO and LUMO due to the increased sterical hindrance. The SpiroAc-DBA achieves the separation of HOMO and LUMO via a fixed separation caused by a spiro center. Molecularly, the donor unit contains an acridine part that is connected to a fluorene part by a four-coordinated carbon atom.

By varying the donor moiety while maintaining the acceptor moiety, the impact of the donor structure on the HOMO and LUMO levels and photophysical properties were investigated. Moreover, charge transport properties and device performance were analyzed, using single-carrier devices (Electron-only EO and Hole-only HO, explained in detail in Chapter 3.1.4) and double-carrier devices (OLEDs, Chapter 3.1). The comparison of EO and HO was performed to get an overview of possible charge transport imbalances of the compounds. The OLED devices were analyzed in order to understand the structure-property relations by investigating the influence of different donor moieties on the device performance. This way, we intend to obtain a more extensive insight into the relationship between donor and acceptor moiety and the impact on optoelectronic properties.

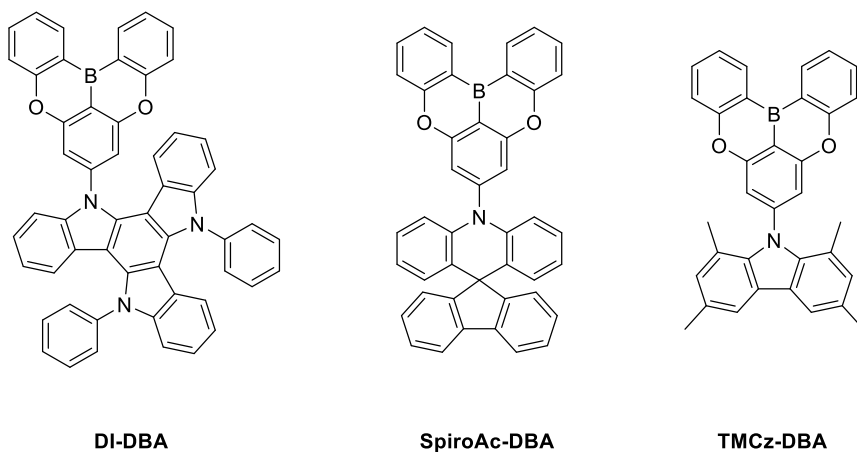


Figure 2.3. Target molecules DI-DBA, SpiroAc-DBA and TMCz-DBA.

3. Theory

3.1. Organic Light-Emitting Diodes (OLEDs)

3.1.1. Basic Functioning of an OLED

The charge transport and light output properties of an OLED device are typically characterized by a JVL (Current vs. Voltage/Luminance) plot. Such a JVL plot is displayed in Figure 3.1 for CzDBA. It can be separated into three sections:

At low voltages, the current density exhibits a linear dependence on the voltage ($J \sim V$). This regime is called the *leakage regime*. The leakage current is caused by parasitical currents without major defects between the electrodes.^[40] With major defects, short circuits would arise that lead to a much higher leakage current.^[41] At intermediate voltages, the current density is dominated by diffusion of charges. This leads to the *diffusion regime* with an exponential dependence on the voltage ($J \sim e^V$) that can be described by the Shockley diode equation 3.1.^[42]

$$J = J_0 \left[e^{\left(\frac{V}{\eta V_T}\right)} - 1 \right] \quad (3.1)$$

In Equation 3.1, J_0 is the saturation current density and η the ideality factor with values of $1 \leq \eta \leq 2$. $\eta = 1$ corresponds to a trap-free charge transport whereas $\eta = 2$ marks a highly trap-assisted recombination.^[43] Trap-free means that the charges (electrons or holes) can move freely without hindrance and recombine to form a bound excited state of an electron-pair called exciton. This is further explained in Chapter 3.1.1.3. V_T is the thermal voltage that describes the potential needed for an electron to gain the thermal temperature $k_B T$. Within the diffusion regime, the current density exhibits a strong temperature dependence that arises from the temperature dependence of the saturation current density J_0 as well as the ideality factor η .^[40,44] At voltages higher than the built-in voltage V_{bi} , the current density is space charge limited and shows a squared dependence on the voltage ($J \sim V^2$). This regime is called the *drift current regime*,^[40] and is described by the Mott-Gurney law (see Eq. 3.3 in Chapter 3.1.4). For a trap-limited emitter, an even higher current density dependence on the voltage is obtained ($J \sim V^k$ with $k > 2$).

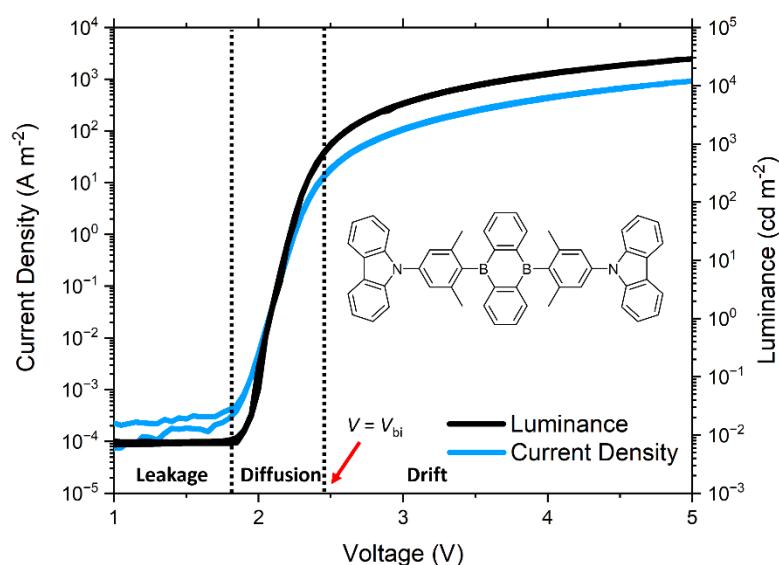


Figure 3.1. Current density versus Voltage Luminance (JVL) plot for a single-layer OLED of 5,10-Bis(4-(9H-carbazol-9-yl)-2,6-dimethylphenyl)-5,10-dihydroboranthrene (CzDBA) in semi-log scale. Data provided by Oskar Sachnik.

3.1.1.1. Charge injection

At the cathode, negative charges (electrons) are injected whereas at the anode positive charges (electron-holes) are injected. For an efficient charge injection, the work function of the injecting electrode and the EML need to be aligned. Usually, this is not given for conventional electrodes, resulting in a charge injection barrier. In order to overcome this barrier, an activation energy is needed. In practice, this is usually achieved by the application of an increased external voltage. However, this comes with the major drawback that higher voltages decrease the device stability and lifetime because a higher energy can cause degradation processes within the organic layers. This might be prevented by introduction of charge injection layers. It is assumed that these layers simplify the injection.

3.1.1.2. Charge transport

After charge injection from the electrodes, the charges have to be transported to the EML. For this purpose, the work functions of the two charge injection layers and the EML have to be aligned. This can be achieved by the application of charge transport layers between the charge injection layers and the EML. Charge transport layers are introduced to confine electrons and holes exclusively inside the EML.^[46]

3.1.1.3. Charge Recombination

Inside the EML of an OLED device, electrons and holes meet and form a bound excited state of electron-hole pairs that are called excitons. Ideally, the relaxation of this exciton leads to the emission of a photon. The efficiency of this desired emissive relaxation process is further explained in Chapter 3.2.

Figure 3.2 displays a Jablonski scheme for the exciton formation after the electrical excitation of electrons. One out of four excitations yields a singlet state (S_1) whereas three out of four excitations result in a triplet state (T_1). This is caused by spin statistics: The possible combinations of the half-integer spins of holes ($s = \frac{1}{2}$) and excitons ($s = \frac{1}{2}$) lead to one possibility of a system with a total spin ($S = \sum_i s_i$) of $S = 0$ (Singlet state) and three systems with a total spin of $S = 1$ (Triplet state). This is schematically presented in Figure 3.3.^[47]

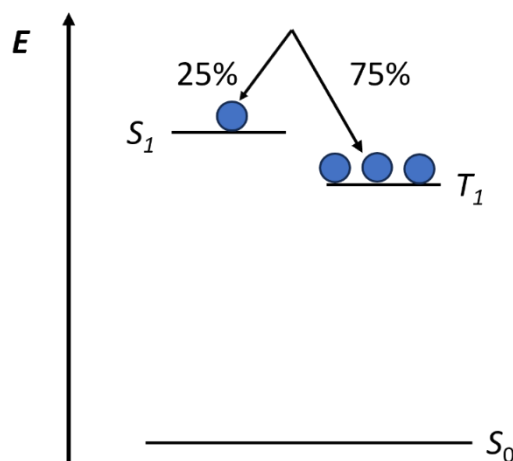


Figure 3.2. Jablonski diagram for electrical excitation of electrons.

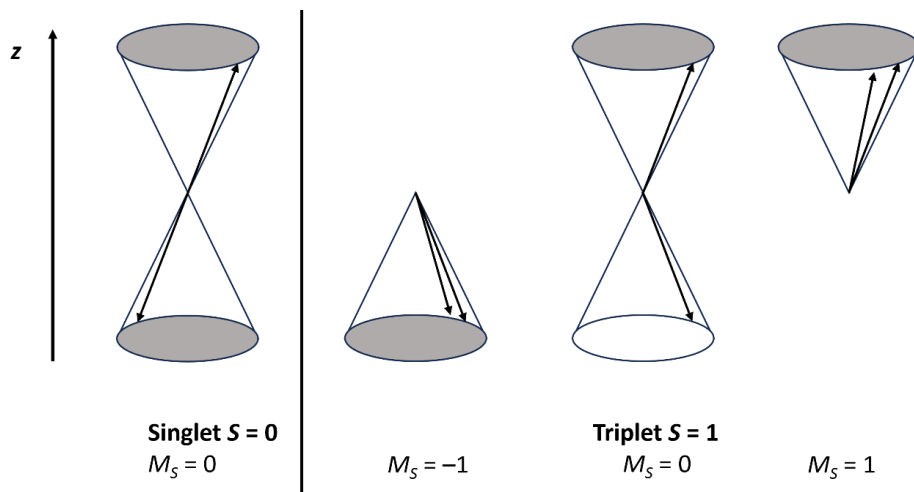


Figure 3.3. Spin statistics for exciton formation as a result of charge recombination of two species with spin $\frac{1}{2}$ (electrons and electron holes). Reproduced according to Ref. [47].

In Figure 3.3, S refers to the total spin of the system that is the sum of the individual spins s_i (e.g. for the only singlet state $S = \sum_i s_i = s_1 + s_2 = -\frac{1}{2} + \frac{1}{2}$) and M_S is the total magnetic spin quantum number of the system that also is a sum of the individual values of the magnetic spin quantum numbers $m_{s,i}$.^[47]

Depending on the balance of charge transport (electrons and electron-holes), charge recombination can either be balanced or unbalanced. Figure 3.4 displays the energy diagram with a comparison of centered electron-hole charge recombination (balanced charge transport) and shifted recombination (unbalanced charge transport). An evaluation of how well the charge transport of a material will be balanced is a comparison of hole and electron trap density. The trap-free window is a guideline for the trapping of charge transport: On the one hand, materials with an ionization energy (IE) of less than -6 eV behave trap-free regarding hole transport.^[30] On the other hand, materials with an electron affinity (EA) of more than -3.6 eV behave trap-free regarding electron transport. Materials with trap-free charge transport exhibit a squared dependence of current density on voltage in the drift current regime according to the Mott-Gurney law (see Eq. 3.3 in Chapter 3.1.4). However, most organic emitters are hole transport dominated. Therefore, the recombination zone is shifted towards the top electrode (cathode). This is displayed in Figure 3.4b). In this case, the excitons are generated closer to the emitter/metal interface. This increases the likeliness for the formation of a surface plasmon polariton which then can lead to a non-radiative decay.^[48,49]

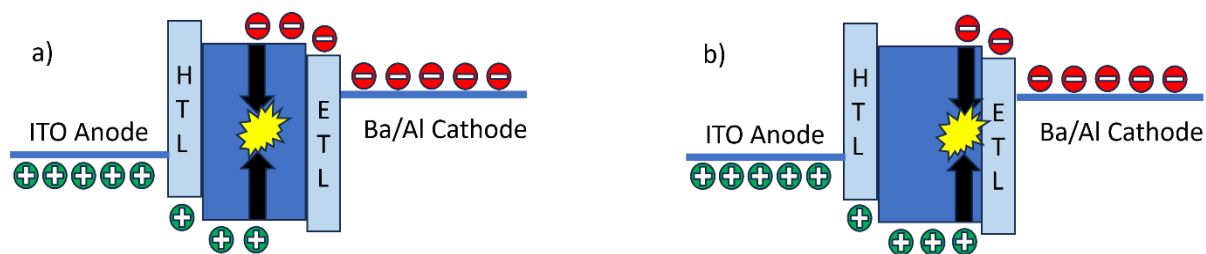


Figure 3.4. a) Centered and b) towards the cathode shifted charge recombination in OLEDs due to balanced and hole-dominated charge transport.

3.1.2. Multi-layer OLEDs

The band diagram of a conventional multi-layer OLED device is presented in Figure 3.5.^[25] The structure of the band diagram resembles a staircase. This is characteristic for a multi-layer OLED device. As Figure 3.5. shows apart from the two electrodes, there are different layers of organic material. A charge-injection layer (compare Chapter 3.1.1.1) supports the injection of the respective charge (electrons at the Ba/Al or electron holes at the indium tin oxide (ITO) anode). After charge injection from the electrodes, the charges are be transported to the EML which is assisted by a charge transport layer (see Chapter 3.1.1.2) for the respective charge. In a conventional multi-layer OLED, additional charge-blocking layers are installed to prevent counter charges from reaching the counter electrodes. The working principles of such charge-blocking layers are described by their work functions: They have very high (for holes) or very low (for electrons) work functions, which can prevent a transfer of counter charges. This also is depicted in Figure 3.5. Inside the EML, the charges recombine and form an exciton. The different processes (charge-injection, charge-transport and charge-recombination) all share the potential to decrease device efficiency and stability. In multi-layer OLEDs optimization of these processes is achieved by the use and alignment of the different above-mentioned organic layers between the two electrodes.^[25]

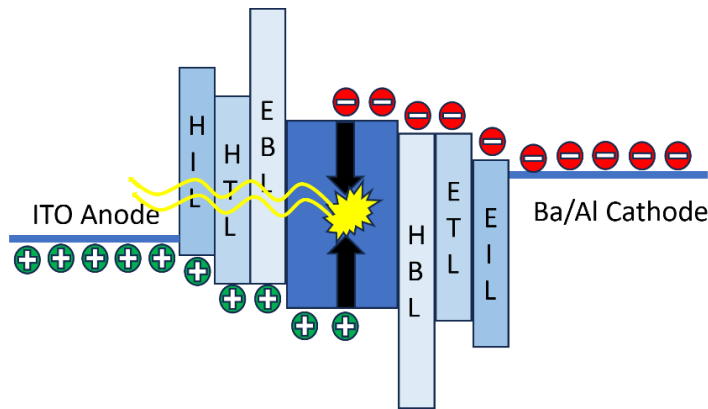


Figure 3.5. Band diagram of a conventional multi-layer OLED device.

Figure 3.6 displays the general architecture of a multi-layer organic light-emitting diode (OLED) with the different modes of the layers as well as the respective refractive indices $n_{D,i}$.

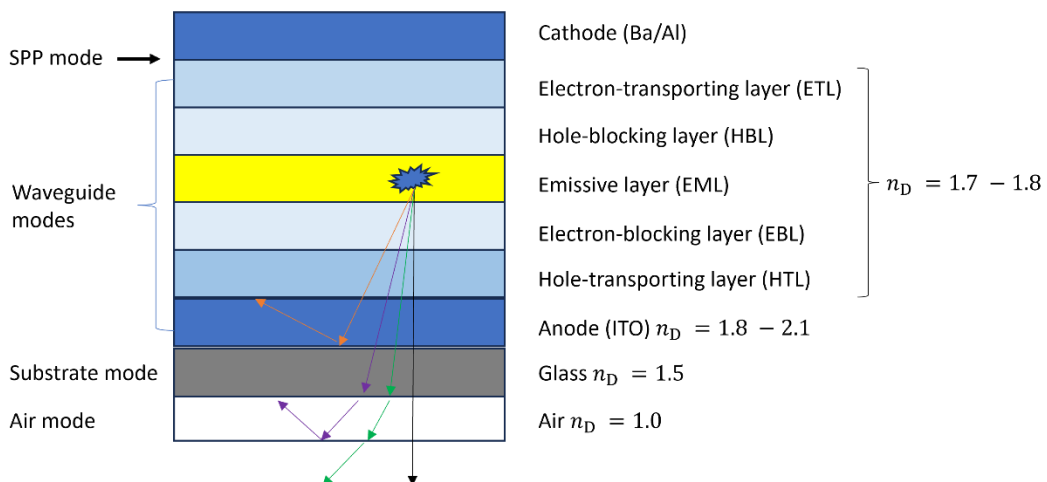


Figure 3.6. Overview of the structure and different modes with refractive indices of the layers in a multi-layer OLED device. The Figure is following Ref. [48].

The generated photons in the device interact with the different layers through reflection, absorption, refraction and thin-film interference.^[50] Eventually, the generated photons leave the device and contribute to light output.^[50] The fraction of generated photons inside the device that can be outcoupled from the device is called the outcoupling efficiency. It can be understood as the efficiency of extracted photons from the device. The outcoupling efficiency for a common OLED device is about 20 – 30%. This means that about 70 to 80% is trapped inside the device and cannot be outcoupled. As a result, the maximum EQE is 20 to 30%. The EQE is a standard benchmark for OLED devices and is defined as the fraction of emitted photons that leave the device by the number of injected charges into the device. Therefore, it can be regarded as a *charge-to-photon conversion efficiency*.^[48,50] In order to increase the outcoupling efficiency and thus the EQE, there are different factors that can be optimized. The greatest influence on the outcoupling efficiency has been proven to be the thickness and refractive indices of the layers within the OLED and the direction of the photon generated from the exciton relaxation.^[51,52] The latter depends on the orientation of the emitter: Photons are per definition emitted perpendicularly to the transition dipole moment (TDM) of the emitter.^[50] Therefore, the outcoupling efficiency of an emitter can be enhanced significantly, if the emitter is oriented in a way that the TDMs are aligned horizontally with respect to the plane of the device.^[50] A horizontal dipole orientation of the emitter TDM enhances the outcoupling efficiency and thus increases the efficiency of an OLED device.^[50] Moreover, the position of the charge recombination profile has a major impact influence on different modes (surface plasmon polariton (SPP) mode, waveguide mode, substrate mode and the air mode) within the device.^[48] The different layers inside the device also have different refractive indices $n_{D,i}$. As a result, the light outcoupling is angle-dependent at the interfaces between the layers. When a photon reaches an interlayer between two layers with a different refractive index, it is refracted. If the next layer has a lower refractive index (Anode => Glass, Glass => Air), the photon is refracted away from the perpendicular. However, beyond a certain critical angle of incidence, the angle of reflection becomes 90°. As a result, the photon is reflected and cannot exit the device, reducing the light outcoupling. This is also displayed in Figure 3.6. Therefore, the alignment of the refractive indices of the different layers inside an OLED device is essential in order to achieve a better OLED performance.^[48]

3.1.3. Single-layer OLEDs

In comparison to the multi-layer OLEDs introduced in Chapter 3.1.2, a single-layer device only consists of an EML between two Ohmic contacts.^[29,30] As Figure 3.7b) points out, there is no staircase-like band structure in contrast to the multi-layer OLEDs mentioned above: The term *single-layer* here does not mean that there is just one layer in the device but that there is no staircase in the band structure. The absence of charge injection-, charge transport- and charge-blocking layers in contrast to a multi-layer device simplifies the device architecture. However, it increases the demands on the emitter and its properties because it has to compensate for all the functions of the above-mentioned layers. A possible OLED architecture with a schematic band diagram for an effective single-layer device is displayed in Figure 3.7a).^[48]

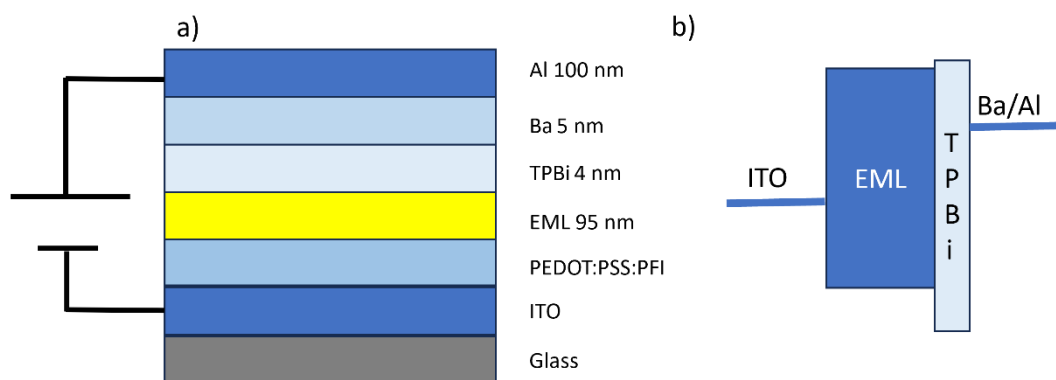


Figure 3.7. a) Device architecture and b) schematic band diagram of the single-layer OLEDs in this work.

In contrast to a multi-layer OLED, in a single-layer device a broad recombination profile is obtained that ideally is located within the center of EML. This way, it is possible to achieve single-layer devices with almost as high outcoupling efficiencies and EQEs as multi-layer devices with an optimized confined emission zone.^[48] This can only be achieved for emitters with balanced charge transport.

3.1.4. Single-Carrier Devices (Electron-Only EO and Hole-Only HO)

For charge transport studies of organic semiconductors, so-called single-carrier devices are fabricated. These enable the exclusive study of electron (electron only, EO) or hole (hole only, HO) charges. The schematic layout of these two devices is presented in Figure 3.8. To achieve a single-carrier device, the working electrodes are only allowed to inject one type of charge, either electrons or holes.

For efficient charge injection, thin interlayers of Buckminsterfullerene (C_{60}) (4 nm) for HOs and TPBi (4 nm) for EOs are introduced. These materials form an Ohmic contact between the electrode and the semiconductor, resulting in a charge injection without any injection barrier.^[29]

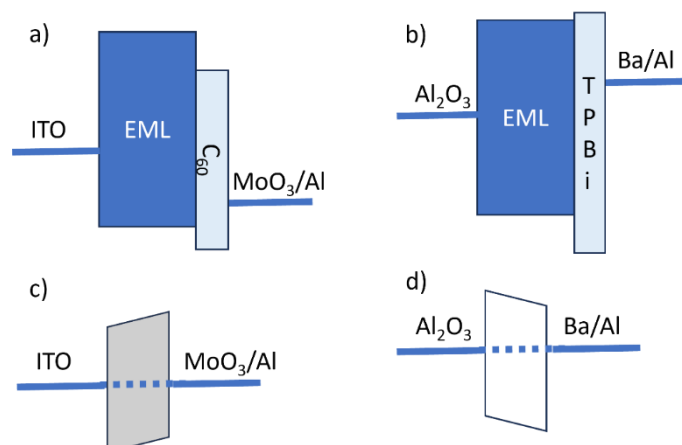


Figure 3.8. Schematic band diagrams (work functions) of the a) HO and b) EO devices and the corresponding band diagrams at the thermal equilibrium (c) and d)).

Figure 3.9 presents the device architecture of an EO as well as a HO device used inside this work. The latter consists of a glass substrate with a patterned ITO layer. On top of the substrate, a layer of PEDOT:PSS:PFI is spin-coated, followed by the evaporated semiconducting layer (95 nm). On top of that, a C_{60} (4 nm) and a molybdenum trioxide (MoO_3) (7 nm) layer is evaporated. The top electrode consists of a 100 nm thick layer of aluminum (Al). The EO device consists of a glass substrate, onto which a 30 nm thick layer of Al as bottom electrode is evaporated. To prevent the injection of holes, the work function is decreased by the oxidation of the aluminum to aluminum trioxide (Al_2O_3). This is

achieved by exposing the aluminum layer to air for five minutes. The next layer is an evaporated EML (95 nm) followed by an evaporated 4 nm thick interlayer of TPBi and the top electrode of a 5 nm thick layer of barium (Ba) and a 100 nm thick layer of aluminum.

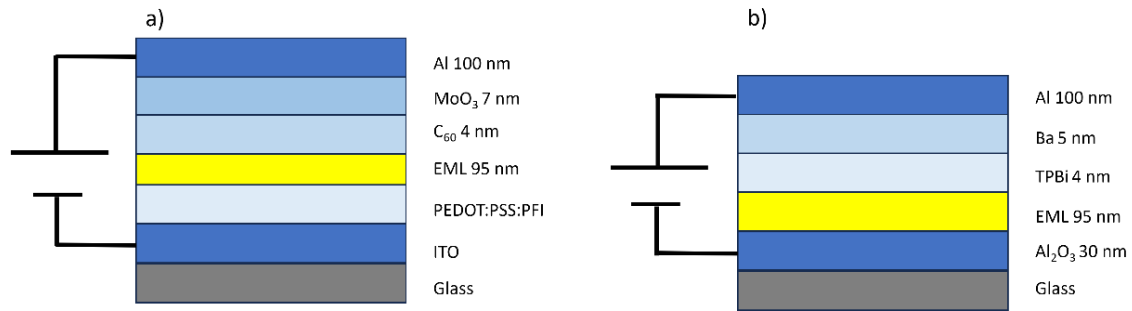


Figure 3.9. General architectures of single-carrier devices: a) HO device architecture; b) EO device architecture.

In contrast to the EO device, for the HO device charges can be injected either from the top or from the bottom depending on the applied bias voltage. Therefore, also for negative bias voltage, a current density is measured. Typically for an organic semiconductor, applied bias voltage (V) is plotted versus the measured current density (J) on a semi-logarithmical scale. Such a JV plot of a HO device is presented in Figure 3.10 for CzDBA. Hole injection is possible from both sides, but an asymmetrical JV curve is obtained in this example. This occurs when the work function of one of the contacts does not match the semiconductor. A JV plot on a log-log scale reveals two different scaling laws between current density and applied voltage: In the diffusion regime at low voltages, a linear dependence ($J \sim V$) is observed. This is the case because in the diffusion regime, the current density is described by a combination of Ohm's law and Fick's first law of diffusion.^[46]

$$J_{\text{diff}} = nq\mu \frac{V}{d} \quad (3.2)$$

In Equation 3.2, J_{diff} is the resulting current density, n the diffused charge carrier density, q the elementary charge, μ the charge mobility, V the applied bias voltage and d the thickness of the active layer.

At higher voltages, the current is space charge limited with a quadratic dependence on the applied bias voltage ($J \sim V^2$). This regime is described by the Mott-Gurney law.^[53]

$$J_{\text{SCLC}} = \frac{9}{8} \varepsilon \mu \frac{(V - V_{\text{bi}})^2}{d^3} \quad (3.3)$$

In Equation 3.3, J_{SCLC} stands for the space charge limited current, ε for the dielectric constant of the emitter and V_{bi} for the built-in voltage which is a result of the difference in the work functions of the two electrodes. To get to this regime, there are two requirements:

- 1.) An Ohmic charge injection from the electrode into the semiconductor.
- 2.) A trap-free charge transport inside the semiconductor.

If the latter is not given, the current density will be trap-limited which leads to a stronger voltage dependence ($J \sim V^k, k > 2$).^[30]

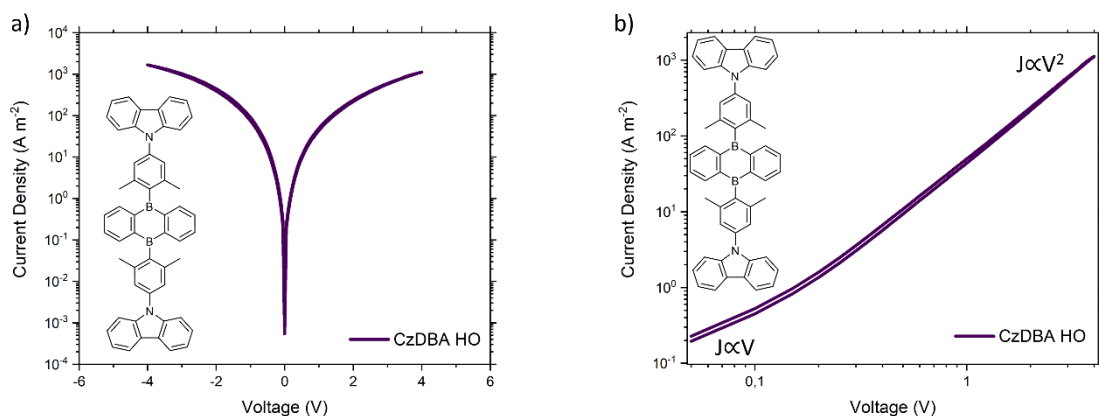


Figure 3.10. Current density versus voltage plot for a HO device of 5,10-Bis(4-(9*H*-carbazol-9-yl)-2,6-dimethylphenyl)-5,10-dihydroboranthrene (CzDBA) on a) semi-log scale b) log-log scale. Data provided by Oskar Sachnik.

For the EO devices in this work, the two electrodes are an aluminum and an aluminum trioxide electrode (compare Figure 3.9b)). The difference in the work functions of these electrodes causes the built-in voltage. In the EO devices, electrons can only be injected from the top electrode because injection from the bottom electrode is hindered by an injection barrier.^[40] Figure 3.11 shows a typical JV plot of an asymmetric EO device for 10-(4-(4,6-diphenyl-1,3,5-triazin-2-yl)phenyl)-10*H*-spiro[acridine-9,9'-fluorene] SpiroAc-Trz on a semi-log as well as on a log-log scale.

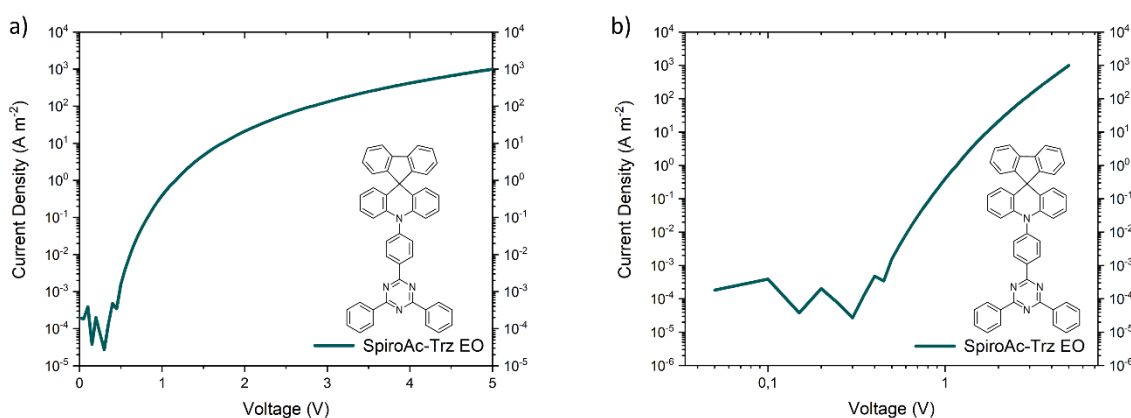


Figure 3.11. Current density versus voltage plot for an electron-only device of 10-(4-(4,6-diphenyl-1,3,5-triazin-2-yl)phenyl)-10*H*-spiro[acridine-9,9'-fluorene] SpiroAc-Trz on a) semi-log scale b) log-log scale. Data provided by Oskar Sachnik.

The log-log scale JV plot in Figure 3.11b) can again be separated into two different regimes. However, in the diffusion regime, the current density no longer is depending linearly on the applied voltage. This is because an accumulation of diffused charge carriers at the top electrode which leads to band bending.^[54] At higher voltages than the built-in voltage, the current density again shows a quadratic dependence on the applied voltage according to the Mott-Gurney law (see Eq. 3.3 in Chapter 3.1.4).

3.2. Development of Materials in OLEDs

3.2.1. Fluorescent Materials

For the first generation of OLEDs, only fluorescent organic emitters were used. Fluorescence is only generated by radiative relaxation from the singlet level (S_1) to the ground state level (S_0). This results in the major drawback of first-generation OLEDs: As Figure 3.12 points out, in a first-generation OLED 75% of recombined charges cannot be used as the triplet state (T_1) cannot be harvested for light output. A major benchmark for the obtained light output is the internal quantum efficiency (IQE) which describes the conversion percentage of injected charges into the device that can create a photon.^[50] The maximum IQE of first-generation OLED devices is only 25%. As Figure 3.12 shows, the other 75% of the generated excitons are trapped inside the triplet state T_1 and decay non-radiatively to the ground state. Therefore, for first-generation OLEDs, not more than 8% EQE could theoretically (30% outcoupling efficiency \times 25% IQE) be achieved.^[55,56]

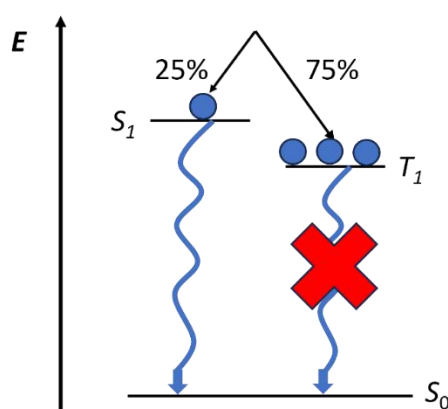


Figure 3.12. Jablonski diagram for first-generation OLEDs using only fluorescent organic emitters.

3.2.2. Phosphorescent Materials

To overcome this intrinsic loss of the triplet excitons, second-generation OLEDs in which phosphorescent emitters are used were introduced. This enables the triplet excitons to be harvested, resulting in a maximum IQE of up to 100%. For phosphorescent emitters, materials are needed that enable the emission of photons from the triplet state T_1 . To be able to reach this triplet state, a spin-forbidden transition is needed: By incorporation of heavy metal atoms (Ir, Pt, Os, Au) to the molecules, the spin-orbit coupling (SOC) is enhanced and a spin-forbidden emissive relaxation from T_1 to the ground state S_0 (Phosphorescence PH) becomes possible. Moreover, the increased SOC also increases the transition from S_1 to T_1 via intersystem crossing (ISC). From there on, PH also is possible. When the ISC rate is significantly higher than the fluorescence rate, up to 100% of the generated excitons populate the triplet state and can be used for phosphorescent emission, yielding an IQE of up to 100%.^[57] Figure 3.13 presents all possible transitions in a Jablonski scheme of a second-generation OLED device using phosphorescent emitters.

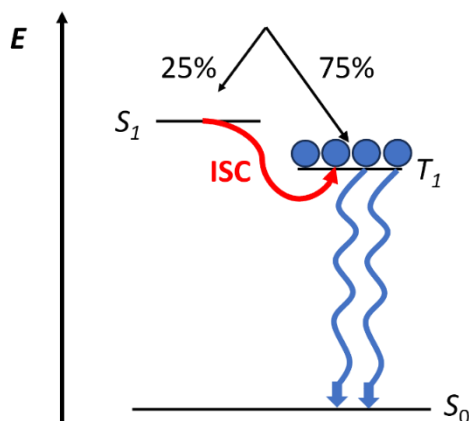


Figure 3.13. Jablonski diagram for second-generation OLEDs using phosphorescent emitters.

3.2.3. TADF Materials

However, the incorporation of heavy metals in order to be able to harvest triplet excitons comes with a major drawback: Heavy metals are expensive and often toxic as well. This was the reason for development of a third generation of OLED devices that use TADF emitters. With TADF materials, triplet excitons can also be harvested and an IQE of up to 100% is possible but with the major advantage of no need for expensive and toxic heavy metal materials.^[16] TADF materials with comparable or even higher efficiencies than phosphorescent emitters have already been reported, proving their promising potential.^[7]

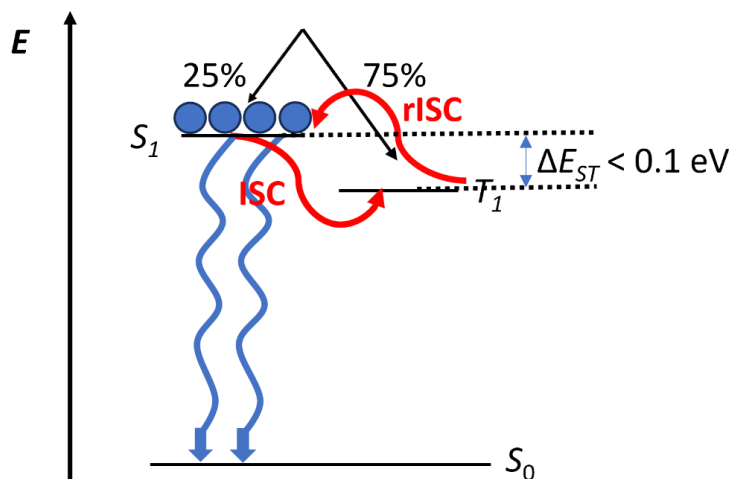


Figure 3.14. Jablonski diagram for a TADF emitter.

TADF emitters are purely organic molecules that enable the harvesting of triplet excitons without any phosphorescent emission. This is achieved by a small energy gap 0.10 eV or less between the lowest excited singlet and triplet state (ΔE_{ST}). Since the electronic transition from the excited triplet state T_1 back to the ground state S_0 is spin-forbidden, it is a comparably slow process with a low rate constant. As a result, the ISC can be followed by an effective rISC from the excited triplet state T_1 back to the excited singlet state S_1 and then decay via fluorescence to the ground state S_0 (compare Figure 3.14).^[16,58]

3.2.3.1. Bi-exponential Intensity Decay

The description of the photophysical properties of a TADF compound can be simplified using the Jablonski scheme in Figure 3.14: From the first excited singlet state S_1 , there are different possible relaxation modes for the electron: On the one hand, it can return to the ground state S_0 in either a radiative (prompt fluorescence PF) or a non-radiative (internal conversion IC) way. On the other hand, it can be converted to the triplet state T_1 via ISC. From T_1 , the electron can also relax back to the ground-state, again either radiative (phosphorescence PH) or a non-radiative (IC). However, as these relaxations are spin-forbidden, the T_1 state has a higher lifetime that gives rise to the thermally activated rISC back to the S_1 . This process is enhanced by a small energy gap ΔE_{ST} between these states (compare Eq. 3.5 in Chapter 3.2.3.2). The radiative relaxation of the electron back to the ground-state S_0 after a rISC is called delayed fluorescence (DF). Therefore, the intriguing characteristic of a TADF emitter is a PF emission in the ns range followed by a DF emission in the μs range. This yields a decay with two components (prompt and delayed) that can be fitted with a bi-exponential decay curve.

$$I = A_1 e^{-\frac{t}{\tau_{\text{PF}}}} + A_2 e^{-\frac{t}{\tau_{\text{DF}}}} \quad (3.4)$$

In Equation 3.4, A_1 and A_2 are the pre-exponential factors for the prompt and delayed fluorescence, t is the time and τ_{PF} and τ_{DF} are the lifetimes of the prompt and the delayed fluorescence.

This characteristic bi-exponential decay for TADF compounds is displayed in Figure 3.15 for the material CzDBA.^[58]

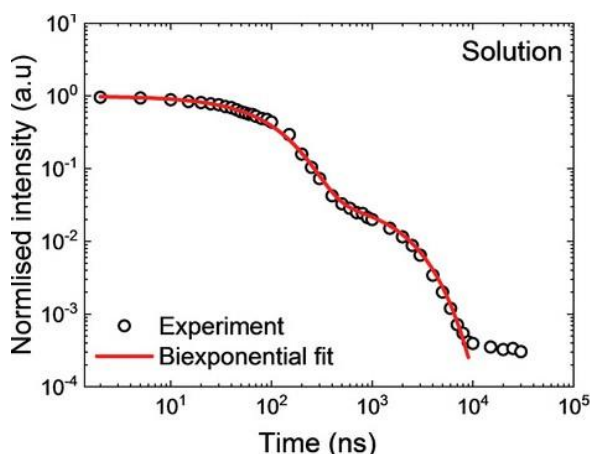


Figure 3.15. Bi-exponential decay curve of the TADF material 5,10-Bis(4-(9H-carbazol-9-yl)-2,6-dimethylphenyl)-5,10-dihydroboranthrene (CzDBA) taken from Ref. [58].

3.2.3.2. Mathematical Description of ΔE_{ST}

Because the rISC is very slow compared to ISC and fluorescence, it is the rate-determining step in the process. In an ideal TADF emitter, the rISC rate is comparable to the ISC rate and much higher than the non-radiative relaxation from the T_1 state to the ground state. In order to increase the rISC rate (k_{rISC}), the energy difference ΔE_{ST} between T_1 and S_1 has to be minimized. This is pointed out by Equation 3.5 which is an Arrhenius equation that enables the determination of k_{rISC} . As it points out, the rISC rate can be increased by a smaller energy gap ΔE_{ST} or a higher temperature T .^[17]

$$k_{\text{rISC}} = A e^{-\frac{\Delta E_{ST}}{k_B T}} \quad (3.5)$$

The energy of the T_1 and S_1 states is defined as the sum of the orbital energy E_{orb} , the repulsion energy between electrons K and the exchange energy J that contains the Pauli repulsion between electrons (see Equations 3.6 and 3.7). Subtraction of E_{T_1} (Eq. 3.6) from E_{S_1} (Eq. 3.7) then yields the energy difference ΔE_{ST} between the orbitals that is $2J$ (Eq. 3.8).^[17]

$$E_{T_1} = E_{\text{orb}} + K - J \quad (3.6)$$

$$E_{S_1} = E_{\text{orb}} + K + J \quad (3.7)$$

$$\Delta E_{ST} = E_{S_1} - E_{T_1} = 2J \quad (3.8)$$

As a result, the energy gap between T_1 and S_1 state only depends on the exchange energy J and therefore can be minimized by minimizing J . On a molecular scale, this can be achieved by spatially separating the HOMO and the LUMO orbital so that the overlap between the two frontier orbitals is minimized. In order to achieve this, a TADF material consists of an electron acceptor A and an electron donor D moiety which favor D-A electron transfer in the excited state. Therefore, TADF molecules are linked via an aromatic bridge and form excited states with strong charge-transfer (CT) character. In order to minimize the overlap of HOMO and LUMO orbital even more, it is possible to either have a twisted orientation between donor and acceptor moiety or to have a fixed separation (e.g. in a spiro compound). This yields a better spatial separation of the frontier orbitals and a minimized exchange energy J .^[59]

3.2.3.3. Synthesis of D-A type TADF Molecules

As described in Chapter 2, there are two different kinds of TADF emitters: molecules with donor and acceptor moieties and MR-TADF. Although, the acceptor moiety of the molecules in this work alone has a structure similar to a MR-TADF (compare Figure 2.2) material, it is connected to a donor moiety in a D-A fashion. The attaching of the acceptor moiety to the donor moiety typically is achieved using a Palladium-Catalyzed C–N Cross-Coupling Reaction of amines with aryl halides called Buchwald-Hartwig amination.^[60] The catalyst cycle schematically is presented in Figure 3.16 and can be explained the following way: The oxidative addition of a Pd(0) L_n species (I) into an aryl halide Ar–X bond yields a Pd(2) species of type II. Then, the coordination of an amine increases the acidity of intermediate III. This enables its deprotonation by a hindered base like potassium *tert*-butyl oxide *t*BuOK. As a result, the palladium amide complex IV is formed. Its reductive elimination then yields the arylated amine product and the regenerated Pd(0) L_n catalyst I.^[61]

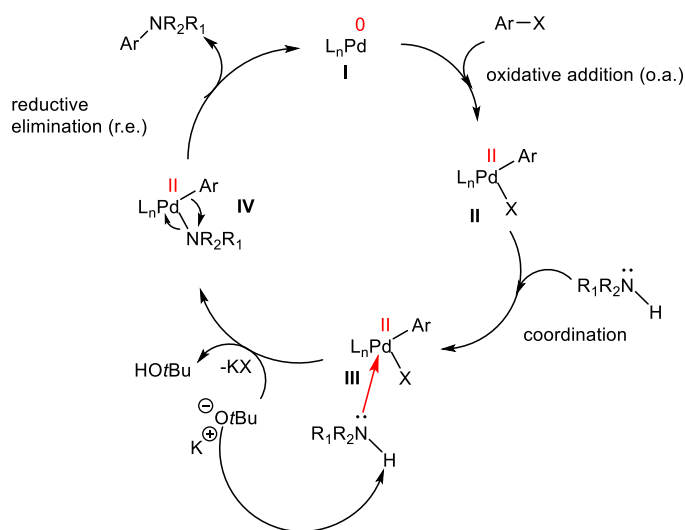


Figure 3.16. Catalyst cycle of the Buchwald-Hartwig amination.

4. Results and Discussion

4.1. Theoretical TD-DFT (time-dependent density-functional theory) simulations

4.1.1. Singlet and Triplet Energy Levels and (ΔE_{ST})

First, DFT (density-functional theory) simulations have been performed on all three structures (TMCz-DBA, SpiroAc-DBA and DI-DBA) to determine the HOMO and LUMO levels, the lowest excited singlet state (S_1), the lowest triplet state (T_1) and the singlet-triplet energy gap (ΔE_{ST}). The obtained values are summarized in Table 4.1. A geometric optimization was performed with Ground-State DFT approach. The calculations were obtained by utilizing the Lee-Yang-Parr correlation function (B3LYP) with a 6–31G basis set to receive HOMO and LUMO energies. An additional energy-based calculation was carried out with a TD-SCF approach and a 6–31G basis set to determine the energies of the lowest excited singlet S_1 and triplet state T_1 . These states enable the calculation of the energy gap ΔE_{ST} as well as the expected emission wavelength. For a TADF emitter, ΔE_{ST} is ideally smaller than < 0.1 eV. This way, rISC can be realized by thermal activation to enhance triplet exciton harvesting.^[47]

Table 4.1. Energy levels for DI-DBA, TMCz-DBA and SpiroAc-DBA. (Optimization: Ground-State DFT, B3LYP, 6–31G basis set with d and p orbitals, Energy: TD-SCF with singlet and triplet states)

Compound	DI-DBA	TMCz-DBA	SpiroAc-DBA
S_1 (eV)	2.69	2.58	2.57
λ_{fl} (nm)	460	480	482
T_1 (eV)	2.62	2.54	2.56
ΔE_{ST} (eV)	0.07	0.04	0.01
$\Delta E_{ST,Lit.}$ (eV)	0.02 ^a	0.02 ^b	0.01 ^c

a: DFT calculation for the optimization of the ground state, TD-DFT calculation for the excited state (B3LYP, with 6–31G basis set).^[39,62]

b: singlet and triplet energies estimated from onsets of the emission spectra at 298 K and 77 K in 30 wt% doped films in PPF, respectively.^[63]

c: DFT calculation for the optimization of the ground state, TD-DFT calculation for the excited state (B3LYP/def2svp), molecule with two additional *tert*-butyl groups on the acceptor and two additional methyl groups on the donor moiety.^[64]

DI-DBA, SpiroAc-DBA and TMCz-DBA exhibit low singlet-triplet energy gaps ΔE_{ST} which are well below < 0.1 eV. Theoretically, this opens up the pathway to high rISC, which should effectively enable the singlet harvesting via prompt fluorescence (PF) and triplet harvesting via delayed fluorescence (DF). These compounds show therefore promising properties to be utilized as efficient emitters with thermally active delayed fluorescence capabilities. At ambient temperatures, the thermal energy RT is 0.03 eV ($R \times T = 8.314 \frac{\text{J}}{\text{mol K}} \times 298 \text{ K} = 2.48 \frac{\text{kJ}}{\text{mol}} = 0.03 \text{ eV}$) demonstrating that rISC for SpiroAc-DBA is supposed to happen. Even though being already reported with an excellent OLED performance, enabled by efficient triplet harvesting, DI-DBA exhibits the largest singlet-triplet energy gap of 0.07 eV.^[9] This can be explained by the obtained DFT results: By a triplet-triplet upconversion (TTU), the T_1 state (2.62 eV) can be transformed into a T_2 state (2.66 eV) which is energetically between T_1 and S_1 state (2.69 eV) and has a low energy gap of only 0.03 eV.^[65] The four relevant energy states of DI-DBA are shown in Table 4.2.

Table 4.2. Lowest energy levels T_1 , T_2 , S_1 and S_2 for DI-DBA (determined by DFT).

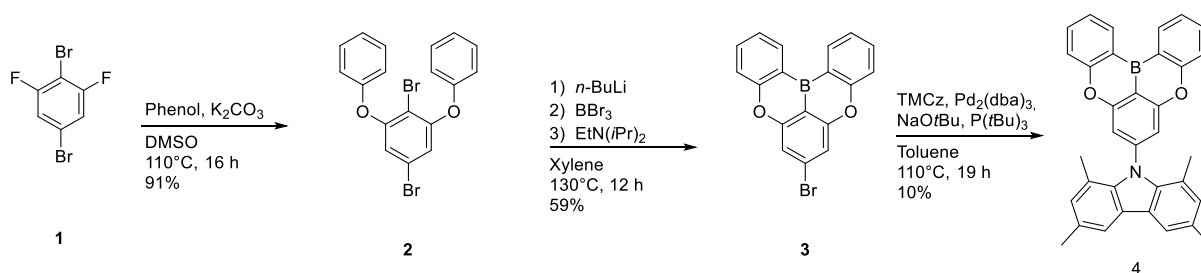
	T_1	T_2	S_1	S_2
Energy (eV)	2.62	2.66	2.69	2.72

As a consequence of four energetically low excited states, describing electronic transitions using the simple three-state system (S_0 , S_1 , T_1 , compare Figure 3.14) is no longer applicable for DI-DBA. This leads to more complex mathematical description of emissive and non-emissive behavior.

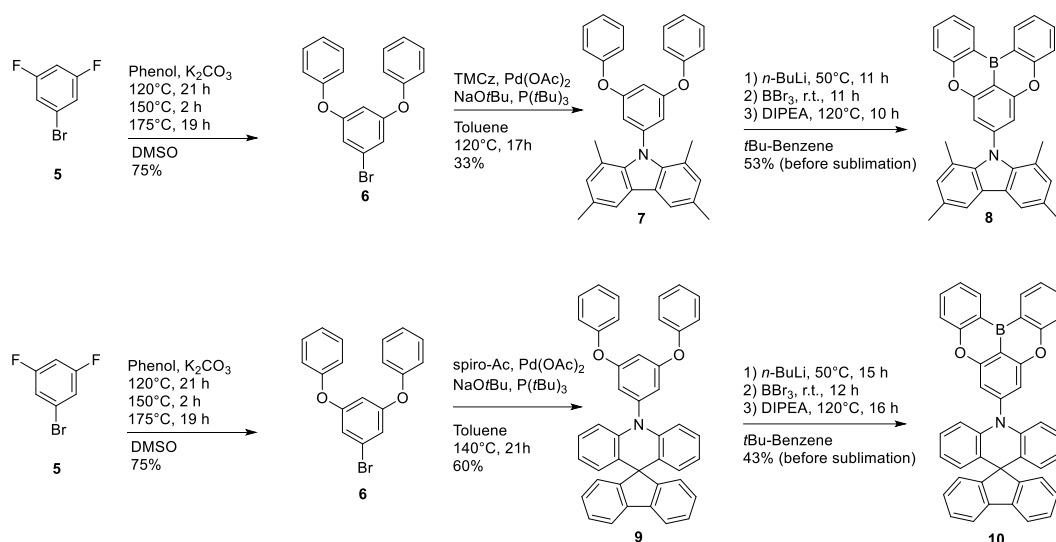
The transition from the first singlet state S_1 to the singlet ground state S_0 can be used to calculate the fluorescence wavelength λ_{fl} . The obtained values are shown in Table 4.1. All three materials emit blue light (DI-DBA: 460 nm, TMCz-DBA: 480 nm, SpiroAc-DBA: 482 nm) with DI-DBA exhibiting the deepest blue emission. In comparison, the λ_{fl} of TMCz-DBA and SpiroAc-DBA is 20 nm red-shifted resulting in an expected sky-blue light emission.

As Table 4.2 points out, all materials exhibit a small ΔE_{ST} of less than < 0.1 eV. The DI-DBA is commercially available. Therefore, we synthesized the TMCz-DBA and the SpiroAc-DBA in order to compare their properties to the DI-DBA.

4.1.2. Synthetic route



For the experimental part, the first approach was the synthesis of a reactive 5-(5,9-dioxa-13b-boranaphtho[3,2,1-*de*]anthracen-7-yl) (DBA) acceptor component (DBA-Br). This would have been ideal because the DBA-Br could have been used as precursor and any suitable donor moiety could have been attached to it, opening the way to a huge pool of TADF molecules. For this purpose, molecule 1 was used as starting material to obtain molecule 2 via nucleophilic substitution of the two fluor atoms by the phenol which worked out quite well (91% yield). In the next step, molecule 2 reacted with n -butyllithium and boron tribromide to form species 3 in a ring-closure reaction. This reaction again was performed with a decent yield (59%). In an exemplary attempt for the attaching of the active DBA-acceptor moiety to a donor moiety, the TMCz-donor moiety was selected. However, this reaction only gave a yield of 10% product 4 (TMCz-DBA). As a result, for the following experimental part, the reaction procedures were performed the other way around: first, the donor moiety was attached to the molecule and in a subsequent step, the ring closure was performed using boron tribromide. The coupling of donor and acceptor moiety was achieved using a Buchwald-Hartwig amination that is described in Chapter 3.2.3.3.^[60,61] This way, TMCz-DBA as well as SpiroAc-DBA were synthesized in sufficient amounts: The attaching of the donor moiety to the acceptor moiety was achieved in yields of 33% for the TMCz-donor molecule and 60% for SpiroAc-donor molecule. The final ring closure reaction then yielded 53% respectively 43% (before vacuum sublimation) of the desired TADF compounds.



4.1.3. HOMO and LUMO Energies

Table 4.3 shows the from the DFT calculations obtained HOMO and LUMO energies. The HOMO levels (DI-DBA: 4.85 eV, TMCz-DBA: 4.90 eV, SpiroAc-DBA: 4.95 eV) are located within the trap-free window, indicating trap-free hole transport for all three compounds. However, the LUMO levels (DI-DBA: 1.77 eV, TMCz-DBA: 1.84 eV, SpiroAc-DBA: 1.88 eV) are far outside the trap-free window, indicating that electron transport will be trap-limited (compare Chapter 3.1.1.3).^[30]

The spatial distributions of HOMO and LUMO of the optimized molecules are illustrated in Figure 4.3. The LUMO of all three emitters is located on the DBA acceptor unit, while the HOMO is distributed over the donor units, with minor LUMO overlap. A small overlap of HOMO and LUMO can be related to a low singlet-triplet energy splitting ΔE_{ST} (see Chapter 3.2.3.2). This is consistent with the low values obtained for ΔE_{ST} (see Table 4.1).

The HOMO and LUMO energies have been determined experimentally in order to compare them to the ones from theoretical calculations. The HOMO levels have been determined by Photoemission Yield Spectroscopy in ambient atmosphere (PYS) using drop-casted films. The resulting data is demonstrated in Figure 4.1a). Extrapolation by linear fitting of the terminal regime yields an intercept indicating the highest occupied molecular orbital. This graphical HOMO determination is referred to as a *Tauc* plot with the photon energy as *x*-coordinate and the to the absorption coefficient normalized quantity^{0.5} on the *y*-coordinate.^[66,67] The obtained values for the HOMO levels are shown in Table 4.3.

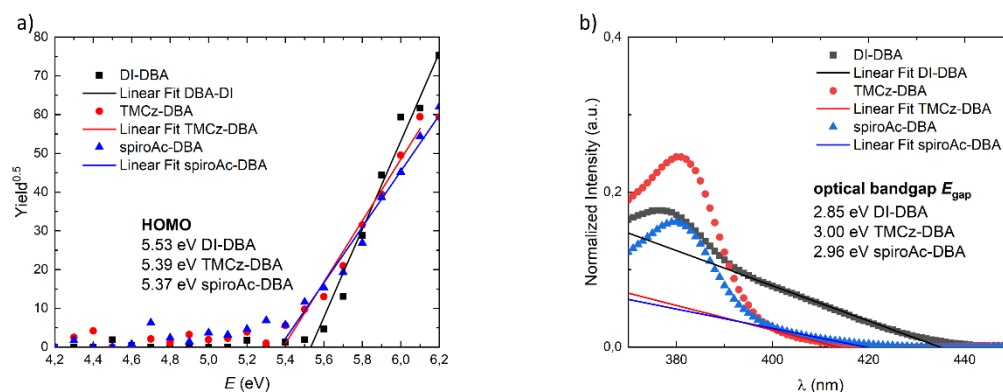


Figure 4.1. Graphical determination of the a) HOMO levels and b) LUMO levels of DI-DBA, SpiroAc-DBA and TMCz-DBA.

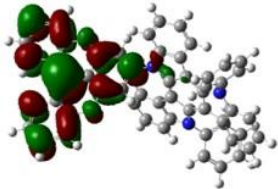
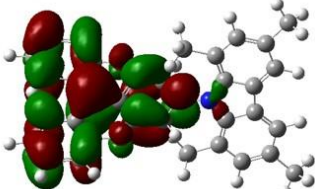
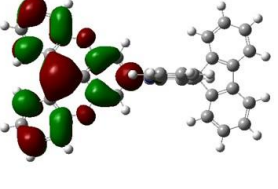
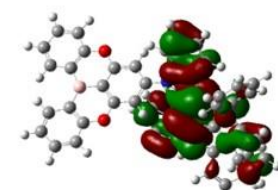
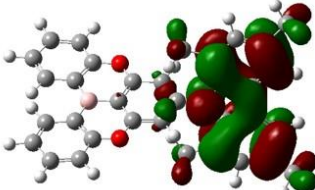
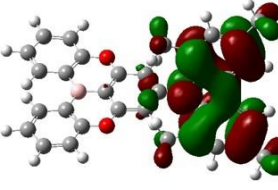
As all three chemical structures share the same acceptor part, the measured differences in HOMO energies have to arise from the donor system of the molecule. The π -system of the DI donor is more elongated than the one of TMCz and SpiroAc donor moiety. This yields a higher electron density distributed over the molecule that might lead to a higher electron density of the HOMO resulting in a slightly higher energy.

The LUMO energy was determined from the absorption spectra (Figure 4.1b)) of pristine neat film samples. The optical bandgap energy E_{gap} can be determined using a tangent at the turning point in the terminal region within the absorption spectra. The LUMO marks the lowest area with no electron density in the system and can be calculated as difference between HOMO and optical bandgap.

$$E_{\text{LUMO}} = E_{\text{HOMO}} - E_{\text{gap}}$$

The obtained values for the HOMO and LUMO levels are summarized in Table 4.3.

Table 4.3. HOMO, LUMO distributions and calculated and experimental energies.

	DI-DBA	TMCz-DBA	SpiroAc-DBA
LUMO			
Calc./Exp./Lit. (eV)	1.77/2.85/2.76 ^a	1.84/2.39/1.83 ^b	1.88/2.41/2.00 ^c
HOMO			
Calc./Exp./Lit. (eV)	4.85/5.53/ 5.51 ^a	4.90/5.39/5.29 ^b	4.95/5.37/4.98 ^c

a: Determined by DFT calculations at B3LYP/ 6–31G level. ^[39,62]

b: Determined by DFT calculations at PBE0/6-31G(d) level. ^[63]

c: Determined by DFT calculations at B3LYP/def2svp level, molecule with two additional *tert*-butyl groups on the acceptor and two additional methyl groups on the donor moiety. ^[64]

For DI-DBA, the literature values are in good agreement with the experimentally determined values but show strong deviations from the DFT calculations. In the case of SpiroAc-DBA, the literature values exhibit the best agreement with the DFT calculations. This seems reasonable since both values were obtained from theoretical calculations. TMCz-DBA in the literature shows quite intriguing behavior: The LUMO level is in good agreement with the theoretically calculated value whereas the HOMO value exhibits much better agreement with the experimentally determined energy level.

The deviation from the experimentally determined LUMO values can be explained by the different conditions between the theoretical calculation and the experimental determination. Remarkably, DI-DBA has a higher LUMO energy than TMCz-DBA and SpiroAc-DBA. All three compounds share the same DBA acceptor, which implies that the donor part has an impact on the LUMO level of the acceptor moiety of the molecule. In contrast to the experimentally obtained HOMO values, which indicate trap-free hole transport, the experimentally obtained LUMO values are outside the trap-free window for

charge-transport, being clearly lower than 3.6 eV. As a result, trap-free hole transport and trap-limited electron transport is expected for the three compounds.^[30]

4.2. Photophysical Properties

4.2.1. UV/Vis Absorption and Emission

For photophysical measurements (UV/Vis absorption, PL emission and photoluminescence quantum yield PLQY) all three compounds were either evaporated on quartz substrates or dissolved in toluene.

Figure 4.2 displays the UV/Vis absorption spectra of films and solution. Film and solution samples exhibit similar absorption characteristics, with maxima around 380 nm. These values are summarized in Table 4.4 and are in good agreement with literature reports.^[62,63] The film samples experience a slight bathochromic shift (1–3 nm), which might be caused by the formation of J-type aggregates in the film sample.^[68]

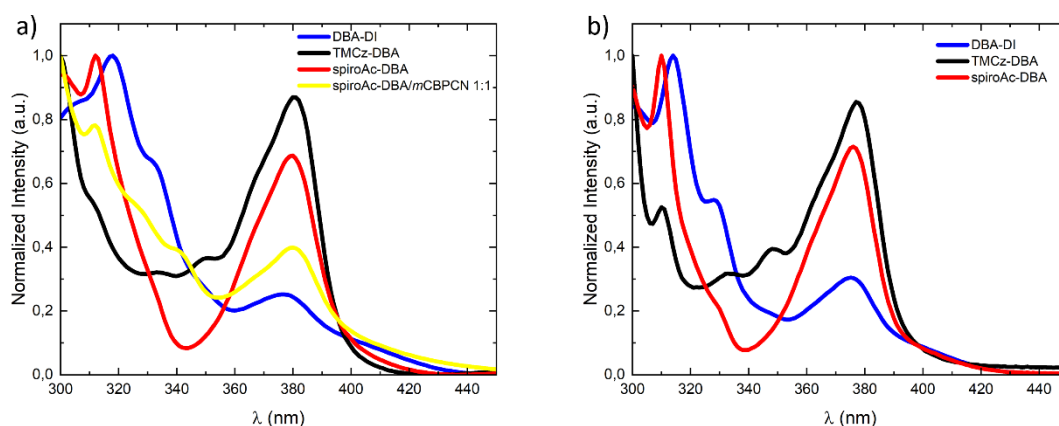


Figure 4.2. UV/Vis absorption spectra of a) evaporated films and b) in 10^{-5} M toluene solutions of the compounds DI-DBA, TMCz-DBA and SpiroAc-DBA.

In Figure 4.2a), the graph of the film samples also contains a SpiroAc-DBA sample doped in a *m*CBP-CN host material. In general, the EML of an OLED device can be doped inside a suitable host matrix. This can have an effect on the charge transport and charge trapping and this way also influence the device performance. For this concept to properly work, the bandgap of the emitter should fit inside that of the host material so that energy transfer from the host to the emitting material is effective. For this sample, the doping was performed because the DFT calculations showed the smallest energy gap ΔE_{ST} of the three compounds and the pristine neat film sample exhibited the highest PLQY (compare Table 4.4). The doped neat film sample of SpiroAc-DBA with 50% *m*CBP-CN shows a quite similar absorption spectrum as the pristine SpiroAc-DBA film sample. The mixing with the *m*CBP-CN host material does exhibit a major influence on the absorption spectrum.

The obtained values of the absorption maxima in 10^{-5} M Toluene solution for SpiroAc-DBA are comparable to a similar molecule incorporating *tert*-Butyl groups on the DBA acceptor and two additional methyl groups on the donor unit: The absorption maxima show good agreement with a slight bathochromic shift for the molecule in Literature that can be the result of the slightly modified structure of the molecule.^[62]

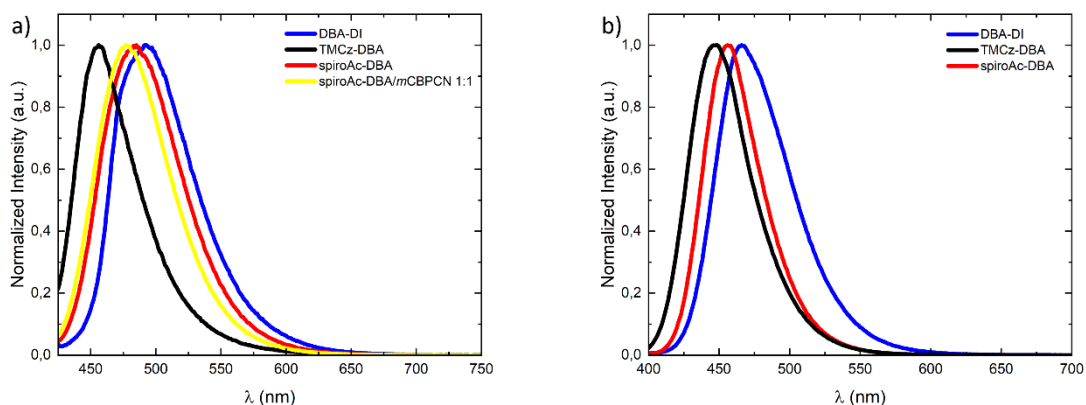


Figure 4.3. PL Emission spectra of a) evaporated films and b) of 10^{-5} M Toluene solutions of the compounds DI-DBA, TMCz-DBA and SpiroAc-DBA.

In Figure 4.3, the PL spectra of both film and solution samples are illustrated. The neat film of TMCz-DBA reaches a maximum PL at 458 nm. SpiroAc-DBA ($\lambda_{\text{max}} = 485$ nm) and DI-DBA ($\lambda_{\text{max}} = 497$ nm) exhibit red-shifted PL with shifts of 27 nm and 39 nm, respectively. TMCz-DBA shows a deep blue PL compared to the sky-blue PL of SpiroAc-DBA and DI-DBA. Both DI-DBA (FWHM = 81 nm) and SpiroAc-DBA (FWHM = 74 nm) show a broad emission (70–100 nm FWHM) which is typical for a D-A type TADF emitter because of the strong vibronic coupling and structural relaxation in the charge-transfer excited states.^[69] Interestingly, the FWHM of TMCz-DBA (54 nm) is relatively narrow, which could be attributed to fewer vibrational levels, indicating less degree of freedom of the molecular structure.

The largest Stokes shift in neat film is observed for DI-DBA (121 nm) with the smallest Stokes shift for TMCz-DBA (78 nm). Doping of SpiroAc-DBA in a matrix, such as *m*CBP-CN, leads to a decrease in the Stokes shift from 105 to 97 nm. A pristine neat film of *m*CBP-CN exhibits an emission maximum at 412 nm,^[70] whereas the pristine SpiroAc-DBA film emits at 485 nm (compare Table 4.5). This might lead to a slightly blue-shifted emission in the in *m*CBP-CN host doped sample (477 nm).

In solution, the PL experiences significant blue shifts for TMCz-DBA (448 nm), SpiroAc-DBA (456 nm) and DI-DBA (466 nm). In comparison, TMCz-DBA still shows the bluest PL, followed by SpiroAc-DBA and DI-DBA. DI-DBA (61 nm) and SpiroAc-DBA (47 nm) experience a reduction of the FWHM in solution. On the other side, TMCz-DBA shows an almost unaltered FWHM of 52 nm. The similar PL and FWHM for TMCz-DBA in both film and solution might indicate that TMCz-DBA is less prone to aggregation compared to SpiroAc-DBA and DI-DBA. Again, the largest Stokes shift is observed for DI-DBA (89 nm) and the smallest for TMCz-DBA (70 nm).

In all cases, the PL is red-shifted for the film samples which can be explained by J-type aggregation in solid state.^[71] For both DI-DBA (31 nm) and SpiroAc-DBA (29 nm) the largest difference between solution and film PL is observed. For TMCz-DBA only a minor difference (10 nm) is measured, which indicates that J-type aggregation is less pronounced.

To estimate the fluorescent capabilities, PLQY measurements of the compounds were performed in film. The results are given in Table 4.4. All materials exhibit a higher PLQY in nitrogen atmosphere than in air. Oxygen is capable of quenching triplet states, leading to a loss of excitons that are required for delayed fluorescence of a TADF emitter.^[72] DI-DBA shows the lowest PLQY in air (19%) and nitrogen (22%), followed by TMCz-DBA (32% in air, 35% in nitrogen) and SpiroAc-DBA (45% in air, 51% in

nitrogen). A common strategy to enhance the film PLQY is doping of the emitter in a host matrix.^[73,74] For TMCz-DBA and SpiroAc-DBA values exceeding 98% are reported.^[39,62–64] These high values are accomplished by low doping ratios of 30 respectively 10%.

SpiroAc-DBA showed the highest neat film PLQY (51%), which makes it promising to be doped in a host matrix. An improvement of up to 73% was accomplished for a 1:1 dilution in mCBP-CN. Further improvement of the film PLQY might be possible by opting for a higher dilution. Nevertheless, the high film PLQY in a simple 1:1 dilution is an indicator for an efficient system with low concentration quenching. Doping SpiroAc-DBA in mCBP-CN shows therefore promising properties to be utilized in an OLED. Table 4.4 summarizes the photophysical properties of the three emitters, including the wavelength of the absorption maxima, the emission maxima, and the PLQY of the neat film samples.

Table 4.4. Summary of the photophysical properties of DI-DBA, TMCz-DBA and SpiroAc-DBA.

	DI-DBA		TMCz-DBA		SpiroAc-DBA		SpiroAc-DBA: mCBP-CN (1:1)
	Film ^a	Sol. ^b	Film ^a	Sol. ^b	Film ^a	Sol. ^b	Film ^a
$\lambda_{\text{abs, max}}$ (nm)	318, 376	314, 375	380	311, 378	312, 380	310, 377	312, 380
$\lambda_{\text{abs, max, lit}}$ (nm)	–	374 ^c	–	282, 377	–	282, 309, 380	–
$\lambda_{\text{em, max}}$ (nm)	497	466	458	448	485	456	477
$\lambda_{\text{em, max, lit}}$ (nm)	–	467 ^c	467 ^d	446 ^e	477 ^f		–
Stokes shift (nm)	121	89	78	70	105	79	97
FWHM (nm)	81	61	54	52	74	47	66
PLQY-O ₂ (%)	19	–	32	–	45	–	70
PLQY-N ₂ (%)	22	–	35	–	51	–	73
PLQY _{lit.} -N ₂ (%)	95 ^g	–	98 ^d	81 ^e	99 ^{f,h}	–	–

a: Neat Film of a thickness of 95 nm.

b: Solution of a concentration of 10⁻⁵ M in Toluene at Room Temperature.

c: in Toluene.^[39]

d: 30 wt% doped thin film in a (diphenylphosphoryl)-dibenzo[*b,d*]-furan (PPF) host matrix.^[63]

e: Solution of a concentration of 10⁻⁵ M in oxygen-free Toluene at Room Temperature.^[63]

f: molecule with two additional tert-butyl groups on the acceptor and two additional methyl groups on the donor moiety, 10 wt% doped film in a PPF host matrix.^[64]

g: 30 wt% doped thin film in a mCBP-CN host matrix.^[39]

h: under argon atmosphere.^[64]

4.2.2. Solvatochromism

Figure 4.4 shows the solvatochromism for TMCz-DBA and SpiroAc-DBA which is typically observed for TADF emitters. Both materials exhibit a red shift with increasing solvent polarity due to the polarizable properties of the excited CT states that exhibit different energies with respect to the polarity of the solvent (see Chapter 1). The solvatochromism of the compounds shows the presence of excited CT states. Moreover, the spectra are well resolved for low-polarity solvents and become increasingly structureless approaching with increasing solvent polarity (see Chapter 1). This also is typical for the emission from excited states with a CT character.^[18] In hexane, which is a prime example of a non-polar solvent, the spectrum is well resolved and the emission maxima are quite similar: at 423 nm for SpiroAc-DBA and at 420 nm for TMCz-DBA. Then, for the much more polar solvent 1,4-dioxane, both spectra are red-shifted exhibiting the maximum emission at 479 nm for SpiroAc-DBA respectively

460 nm for TMCz-DBA. With further increasing the polarity (chloroform < ethyl acetate < dichloromethane), the emission is further red-shifted and exhibits the highest intensity for the most polar solvent dichloromethane at 511 nm for SpiroAc-DBA respectively at 508 nm for TMCz-DBA.

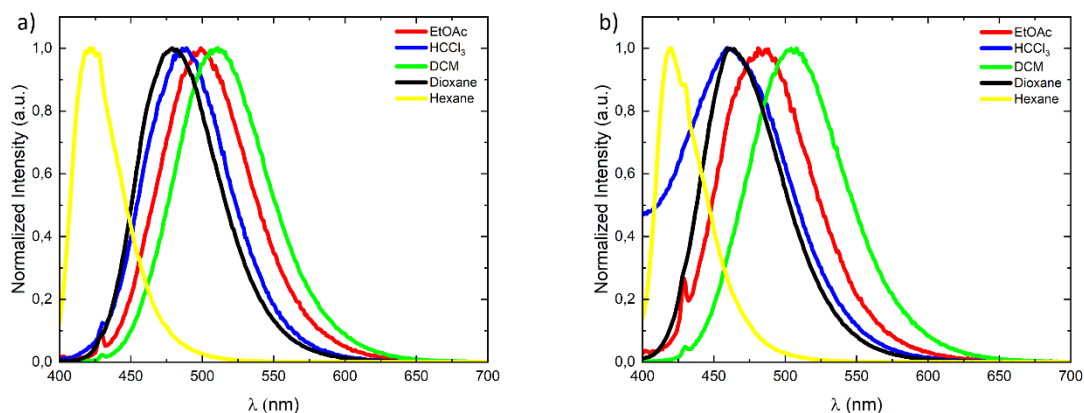


Figure 4.4. Solvatochromism for a) SpiroAc-DBA and b) TMCz-DBA.

4.2.3. Time-resolved photoluminescence (TRPL)

In order to investigate the characteristic photoluminescent properties, time-resolved photoluminescence (TRPL) spectra were recorded on neat evaporated films (Figure 4.5).

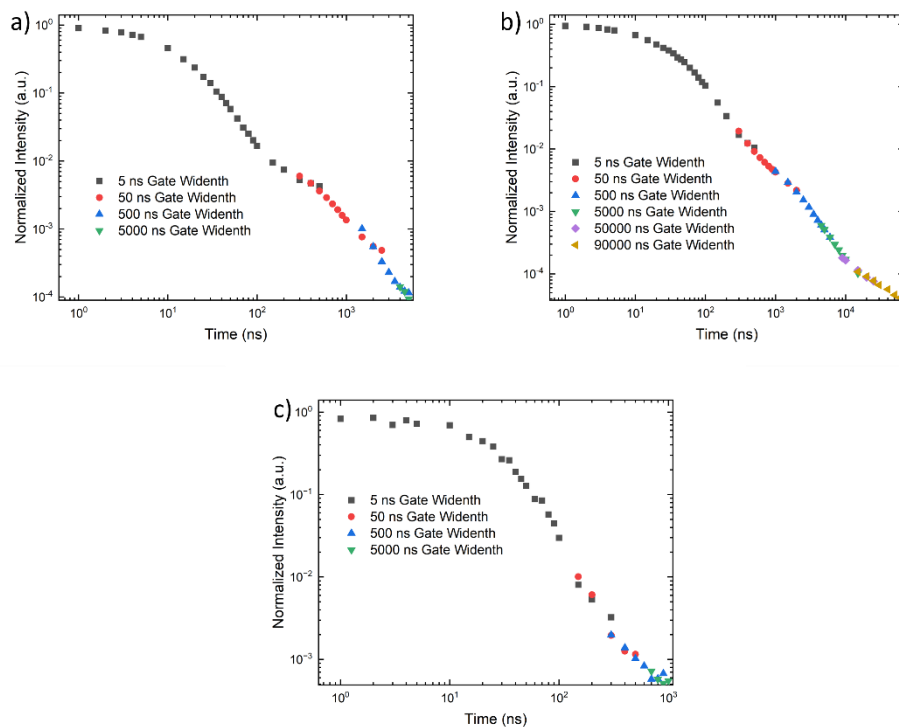


Figure 4.5. TRPL Measurements on a) DI-DBA, (b) SpiroAc-DBA and c) TMCz-DBA pristine evaporated films (95 nm).

The TRPL measurements reveal a bi-exponential decay curve in DI-DBA and in SpiroAc-DBA. For TMCz-DBA, the expected bi-exponential decay could not be observed. The longest lifetime is observed in SpiroAc-DBA, reaching a detectable signal even after 5×10^4 ns (50 μ s). This shows the DF of the material quite well as a DF takes place on timescales in the μ s ($> 10^3$ ns) region whereas the PF takes place on timescales in the ns regime (compare Chapter 3.2.3.1). Fitting the prompt and delayed curves into two separate exponential decay curves (see Appendix), the lifetimes of the prompt τ_{PF} and delayed fluorescence τ_{DF} can be derived (see Table 4.5). For both, PF and DF part, SpiroAc-DBA exhibits the highest lifetime that is also comparable to literature data. However, the data obtained for DI-DBA and TMCz-DBA show a quite strong deviation from literature. A possible reason for this can be the doping of the molecules in literature. Both molecules were measured at 30 wt% in a host matrix.

Table 4.5. Lifetimes of prompt τ_{PF} and delayed τ_{DF} fluorescence for DI-DBA, SpiroAc-DBA and TMCz-DBA.

Compound	DI-DBA	SpiroAc-DBA	TMCz-DBA
τ_{PF} (ns)	15	34	27
$\tau_{PF,Lit.}$ (ns)	23 ^a	37 ^b	38 ^c
τ_{DF} (μ s)	0.39	1.86	—
$\tau_{DF,Lit.}$ (μ s)	1.25 ^a	1.69 ^b	0.75 ^c

a: 30 wt% doped thin film in a *m*CBP-CN host matrix.^[39]

b: 10 wt% doped film in a PPF host matrix and under argon atmosphere, molecule with two additional *tert*-butyl groups on the acceptor and two additional methyl groups on the donor moiety.^[64]

c: 30 wt% doped thin film in a PPF host matrix.^[63]

4.2.4. Ellipsometry

Ellipsometry measurements were performed on neat film samples (30 nm thickness) on SiO₂ wafers (1.4 \times 2.0 cm) without oxidation layer. The refractive indices n_D of the three samples were determined by plotting the measurements for three different angles (65°, 70°, 75°). The obtained graphs are displayed in Figure 4.6.

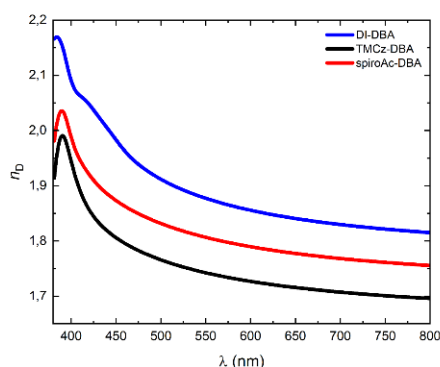


Figure 4.6. Refractive indices $n_{D,i}$ of DI-DBA, SpiroAc-DBA and TMCz-DBA in dependence on the wavelength.

As demonstrated in Figure 4.6, the highest refractive index n_D is observed for DI-DBA reaching a value of 2.17. The n_D for TMCz-DBA and SpiroAc-DBA is slightly lower with 1.99 and 2.04, respectively. For all materials, the maximum n_D is reached around 400 nm. An appropriate alignment of the refractive indices of the different layers within an OLED device is crucial in order to achieve an effective light outcoupling (see Chapter 3.1.2).

4.2.5. Angular Dependency

In order to determine the horizontal dipole orientation, angular dependency measurements were performed on encapsulated samples of the three emitters on eagle glass substrates. Table 4.6 displays the obtained values for the horizontal dipole orientation of DI-DBA, TMCz-DBA and SpiroAc-DBA. The plotted data can be seen in the Appendix (Chapter 10).

Table 4.6. Horizontal dipole orientations of DI-DBA, TMCz-DBA and SpiroAc-DBA.

Compound	Horizontal Dipole Orientation (%)
DI-DBA	83
TMCz-DBA	69
SpiroAc-DBA	78

DI-DBA as well as SpiroAc-DBA exhibit high horizontal dipole orientations with 83% and 78%. Therefore, especially these two materials can be considered promising emitters for the application in OLEDs. A high horizontal orientation of emissive transition dipole moments can increase the light outcoupling efficiency and therefore improve the overall EQE of the devices (see Chapter 3.1.2).

4.3. Device Characteristics

4.3.1. Electron- and Hole-only Devices

Single-carrier devices (HOs and EOs), as well as double-carrier devices (OLEDs) of the three emitters were fabricated to examine the charge transport properties. The detailed fabrication procedures can be found in the methods part (Chapter 6.2). Figure 3.9 in Chapter 3.1.4 displays the structures of the HO and EO single-carrier devices. For application in a single-layer OLED, transport of holes and electrons needs to be balanced. Fabricating hole- and electron-only devices and measuring the current density-voltage characteristics allows a first estimation for the balance of charges. Ideally, both single-carrier devices should exhibit a similar current density at the same voltage. If this can be achieved within a single EML, no additional electron- and/or hole-transport layers are needed, resulting in less elaborate device fabrication.

In Figure 4.7 hole and electron-onlys of the three different compounds as well as the SpiroAc-DBA :mCBP-CN sample (1:1) are shown. This allows a qualitative analysis of the charge balance.

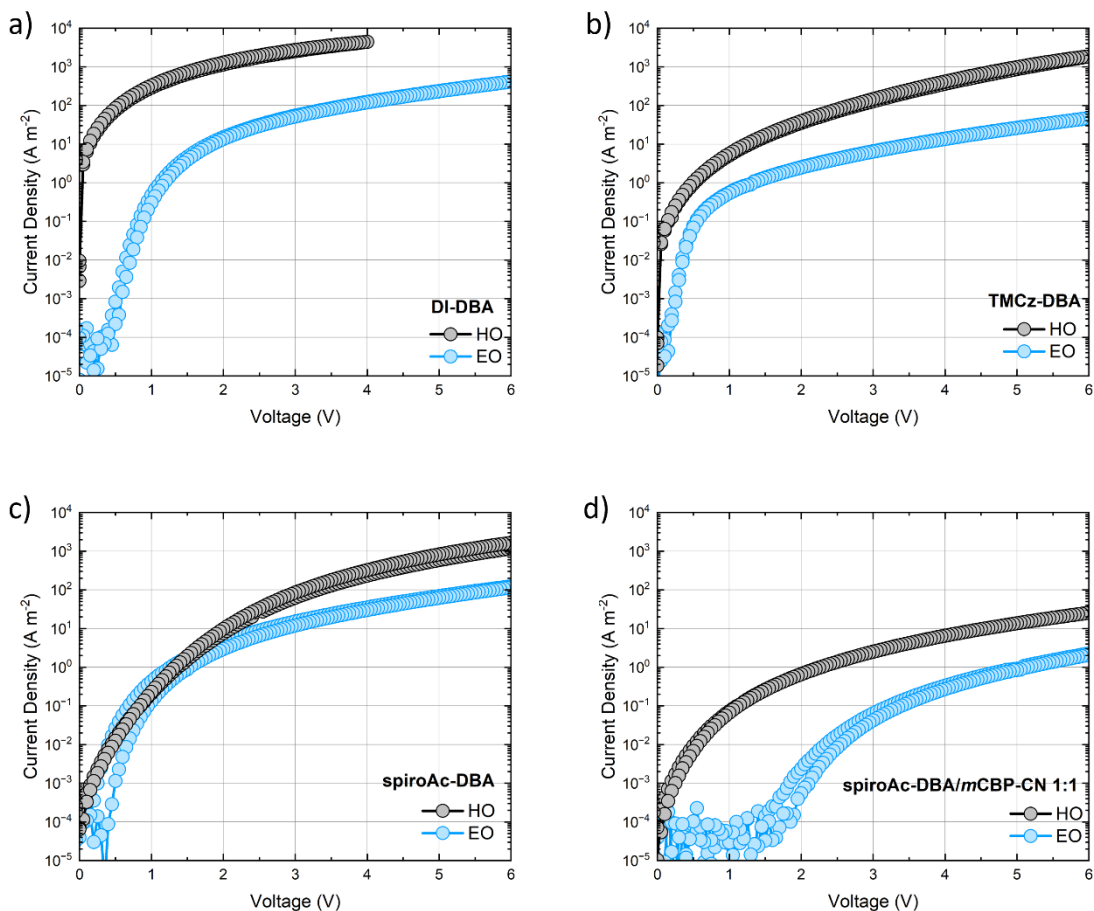


Figure 4.7. Comparison of HO (grey) and EO (blue) devices of a) DI-DBA, b) TMCz-DBA, c) SpiroAc-DBA and d) SpiroAc-DBA:*mCBP-CN* 1:1 in order to compare its charge transport properties. The EMLs have a thickness of 95 nm except TMCz-DBA with 110 nm.

Charge transport is relatively unbalanced for DI-DBA and TMCz-DBA, with the hole transport being almost 2 orders of magnitude higher than the electron transport. The best balance in terms of charge transport is achieved in SpiroAc-DBA. Compared to neat SpiroAc-DBA, the electron and hole current experience a decrease for the SpiroAc-DBA:*mCBP-CN* 1:1 sample, which is expected upon dilution. The decrease of both currents indicates that hole and electron transport is carried by SpiroAc-DBA, which is in good agreement with the HOMO (6.1 eV) and LUMO (2.5 eV) levels of *mCBP-CN*.^[70]

4.3.2. OLED Devices

As a next step, single-layer OLEDs based on all three emitters were fabricated. The emissive layer was sandwiched between an ohmic electron and hole contact. The architecture of the devices is presented in Figure 3.7 in Chapter 3.1.3.

The electroluminescence (EL) spectrum (see Appendix) of the four film samples in Table 4.7 was captured to determine the wavelength of the emitted photons, which is required for calculation of the external quantum efficiency (EQE). The EQE represents a common guideline for the efficiency of OLED devices (see Chapter 3.1.3).^[75]

The main EL characteristics are summarized in Table 4.7.

Table 4.7. Characteristics of the EL inside the devices for DI-DBA, TMCz-DBA, SpiroAc-DBA and SpiroAc-DBA:*mCBP-CN* (1:1).

Compound	DI-DBA	TMCz-DBA	SpiroAc-DBA	SpiroAc-DBA: <i>mCBP-CN</i> (1:1)
$\lambda_{em, max}$ (nm)	504	487	503	493
FWHM (nm)	78	88	74	64

TMCz-DBA shows a blue EL at 487 nm. DI-DBA (504 nm) and SpiroAc-DBA (503 nm) exhibit red-shifted EL spectra, which agrees with the PL trend in neat film. The doping of SpiroAc-DBA in *mCBP-CN* leads to a blue shift of the electroluminescence, which has already been observed in the neat film PL. (compare Table 4.4).

The FWHM of all emitters is relatively broad, with SpiroAc-DBA showing the narrowest FWHM (74 nm). Surprisingly, TMCz-DBA displays a quite broad emission with a FWHM of 88 nm. The doping of SpiroAc-DBA leads to a narrower EL spectrum showing a FWHM of only 64 nm. Therefore, the doping of the SpiroAc-DBA in *mCBP-CN* leads to an improvement in color purity. However, the doping decreases the electron as well as the hole current (see Figures 4.8 c) and d)). Identifying a suitable host for SpiroAc-DBA that enhances the color purity and supports the charge transport, requires more future investigations.

The resulting current density was measured by a scan of a set voltage regime and the light output was detected by a silicon photodiode on top of the measured OLED area. Figure 4.8 shows the JVL (current-voltage-luminance) curves for the four measured samples. For the current density, different regimes can be distinguished: In the low voltage regime (leakage regime) the current is leakage dominated with a linear dependence on voltage. At intermediate voltages the current density starts to increase in the diffusion regime with an exponential dependence on voltage. At higher voltages the current exhibits a flattening in the drift regime in which the current becomes space charge limited. The LV (luminance vs. voltage) plot enables the determination of the switch-on voltage of the OLED. The switch-on marks the voltage needed for the device to reach a luminance of 1 cd m^{-2} and to show visible light output. The driving voltage is a typical guideline for an OLED device and marks the voltage that is needed for a luminance of $1,000 \text{ cd m}^{-2}$.^[76]

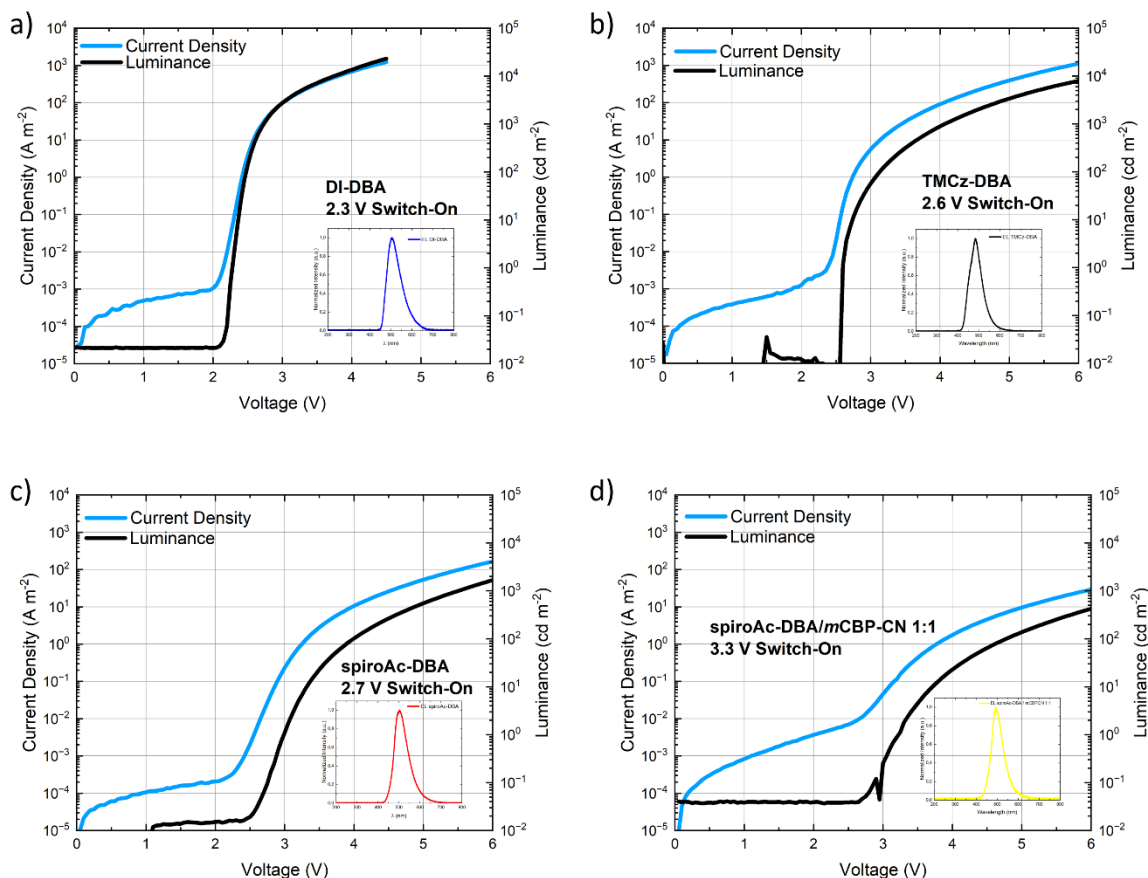


Figure 4.8. JVL curves of a) DI-DBA, b) TMCz-DBA, c) SpiroAc-DBA and d) SpiroAc-DBA/*mCBP-CN* 1:1. The EMLs have a thickness of 95 nm.

The OLED employing DI-DBA shows the lowest switch-on voltage (2.3 V) by far and also the lowest driving voltage of only 2.8 V. In comparison, TMCz-DBA as well as SpiroAc-DBA device require driving voltages of more than 4 V (4.5 respectively 4.8 V). The device employing SpiroAc-DBA:*mCBP-CN* 1:1 requires a driving voltage of 7.1 V, which is matching the fact that dilution of the emitter reduces the hole and electron current (see Figure 4.7d)). All JVL curves in Figure 4.8 also display the above-mentioned typical three areas of the current density (see Chapter 3.1).

The EQE and the power efficiency are guidelines for the performance of an OLED device. Among the investigated devices, DI-DBA achieves the best EQE of 13%. TMCz-DBA only reaches an EQE of 4%. The device with SpiroAc-DBA exhibits a slightly higher EQE of 5%. The doping of SpiroAc-DBA in *mCBP-CN* host increases the EQE a bit to 7%. Typically, doping of an emitter inside a suitable host molecule enhances the device efficiency. However, this is not the case for the in *mCBP-CN* doped sample of SpiroAc-DBA. A possible explanation is the imbalance of charge carriers (compare Figure 4.7) that leads to a shift of the recombination zone towards the top electrode (cathode) and causes increased cathode quenching (see Chapter 3.1.1.3).^[49]

The position of the recombination profile has a major impact on different modes (waveguide mode, substrate mode and the air mode) within the device.^[37] The different layers inside the device also have different refractive indices $n_{D,i}$. As a result, the light outcoupling is angular dependent at the interfaces between the layers and therefore the outcoupling efficiency changes with the distance from the recombination zone to the interface. This is the main reason for the decrease in the light output and the fact that an EQE of close to 100% can never be realized (see Chapter 3.1.2).^[37] Therefore, the

alignment of the refractive indices of the different layers inside an OLED device is essential in order to achieve a better OLED performance.

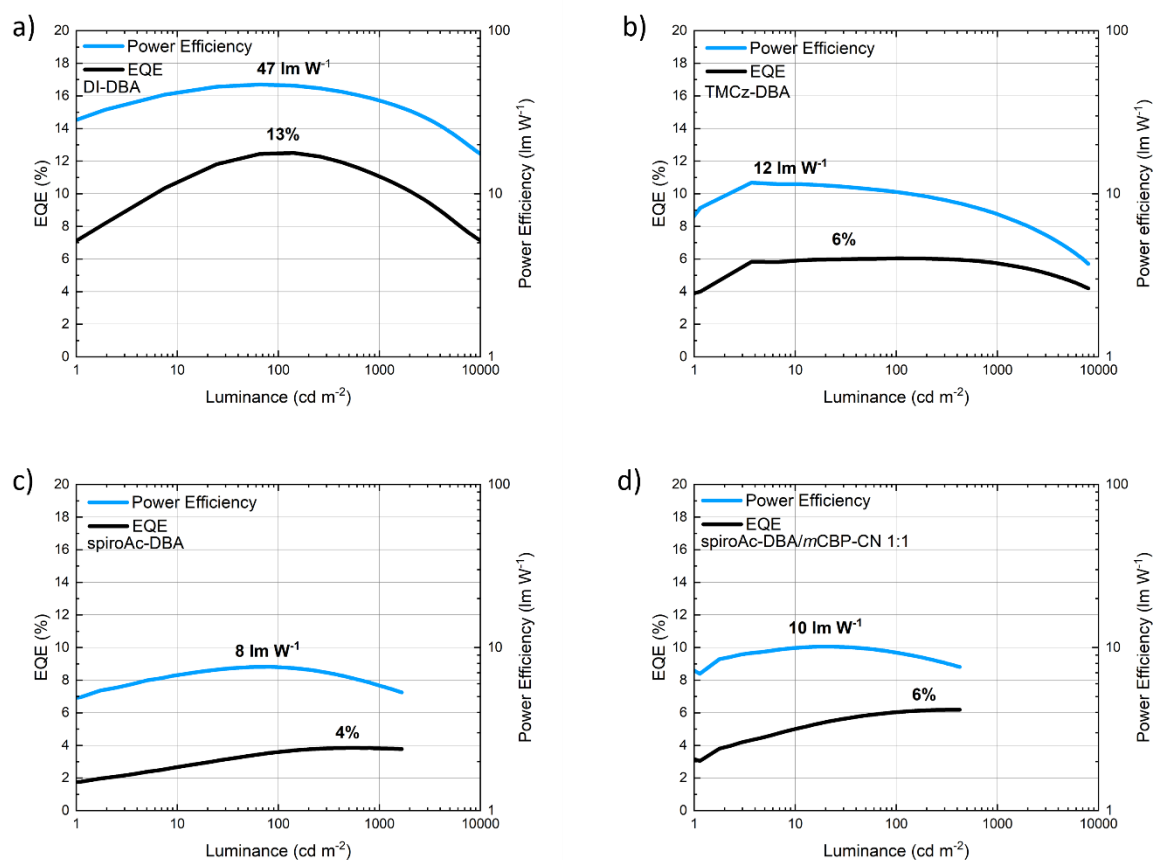


Figure 4.9. External quantum efficiency (EQE) and power efficiency curves of a) DI-DBA, b) TMCz-DBA, c) SpiroAc-DBA and d) SpiroAc-DBA/*mCBP-CN* 1:1. The EMLs have a thickness of 95 nm.

As shown in Figure 4.9a), the by far best power efficiency and EQE can be achieved with DI-DBA. The doping of SpiroAc-DBA in *mCBP-CN* host only yields a small increase in the EQE of the device.

Table 4.8 shows a summary of the EL device characteristics of the fabricated blue TADF-OLEDs containing the EL emission maximum, the FWHM, the switch-on voltage V_{on} , the driving voltage $V_{driv.}$, the maximum and the maximum power efficiency of the devices.

Table 4.8. Summary of the device parameters of the single-layer devices of DI-DBA, TMCz-DBA, SpiroAc-DBA and SpiroAc-DBA in *mCBP-CN* (1:1).

Compound	DI-DBA	TMCz-DBA	SpiroAc-DBA	SpiroAc-DBA / <i>mCBP-CN</i> (1:1)
$\lambda_{em,max}$ (nm)	504	487	503	493
FWHM (nm)	78	88	74	64
V_{on} (V)	2.3	2.6	2.7	3.3
$V_{driv.}$ (V)	2.8	4.5	4.8	7.1
EQE _{max} (%)	13	6	4	6
$\eta_{p,max.}$ (lm W ⁻¹)	47	12	8	10

5. Summary and Conclusion

In this work, different MR-TADF molecules with the same 5-(5,9-dioxa-13b-boranaphtho[3,2,1-*de*]anthracen-7-yl) (DBA) acceptor moiety were synthesized and compared regarding their photophysical properties and performance in OLED devices. The donor moiety of these molecules was varied in order to analyze its impact on the devices and photophysics to achieve a deeper understanding of structure-property relationships.

TD-DFT (time-dependent density function theory) calculations were performed on these three molecules as a way to get insights on HOMO and LUMO levels as well as the energy gap between lowest excited singlet and triplet state ΔE_{ST} .

The determined HOMO energies are all located within the trap-free window, indicating that electron-hole transport can be expected to be trap-free. However, the LUMO energies of the three emitters are far outside the trap-free window, indicating that electron transport will be trap-limited.

The DFT calculations also pointed out that for all three emitters, the LUMO is located on the DBA acceptor unit, while the HOMO is distributed over the donor units, with minor LUMO overlap. This is consistent with the low ΔE_{ST} values for all three emitters because a small overlap of HOMO and LUMO can be related to a small exchange energy and thus a low singlet-triplet energy splitting ΔE_{ST} . For all three emitters, the energy gap ΔE_{ST} was smaller than 0.1 eV. Therefore, an efficient rISC can be realized by thermal activation, making the molecules promising candidates for TADF properties. With an energy splitting of only 0.01 eV, SpiroAc-DBA exhibits the smallest value and therefore, in a second step, was investigated in a doped OLED with *m*CBP-CN as host matrix. Moreover, the DFT calculations showed that for the emission process of the DI-DBA, not only T_1 and S_1 but also T_2 and S_2 have to be considered due to their similar energies.

The photophysical investigations of the neat film samples pointed out that all materials are blue emitters with TMCz-DBA emitting light in the deep blue region whereas SpiroAc-DBA and the DI-DBA can be considered sky-blue emitters. TMCz-DBA shows the most pronounced emission with a FWHM of 54 nm and therefore displays the highest color purity of the three materials. This could result from fewer vibrational levels, and therefore less degrees of freedom of the molecular structure. In the analysis of the photoluminescence quantum yield (PLQY), SpiroAc-DBA showed the highest neat film value of 51% which was increased to 73% in a 1:1 dilution in the host material *m*CBP-CN. Further improvement of the film PLQY might be possible by opting for a higher dilution.

For SpiroAc-DBA as well as TMCz-DBA, the solvatochromism was investigated and successfully confirmed, pointing out the emission from excited states with CT character that is typical for TADF compounds.

To analyze the photoluminescent decay of the emitters, time-resolved photoluminescence (TRPL) spectra were recorded on neat evaporated films. These revealed a bi-exponential decay curve in DI-DBA and in SpiroAc-DBA. However, for TMCz-DBA, the expected bi-exponential decay could not be observed. The longest lifetime could be observed in SpiroAc-DBA, reaching a detectable signal even after 50 μ s. This displays the delayed fluorescence (DF) of the material quite well as a DF takes place on timescales in the μ s region whereas the prompt fluorescence (PF) takes place on timescales in the ns regime. Fitting the prompt and delayed fluorescence parts into two separate exponential decay curves, the lifetimes of the prompt and delayed fluorescence were derived: These showed for both, PF and DF, the highest lifetime for the SpiroAc-DBA among the three different emitters with 34 ns respectively 1.86 μ s.

Furthermore, ellipsometry measurements were performed on neat film samples of the materials. The obtained data is of interest for an appropriate alignment of the refractive indices of the different layers within an OLED device to be able to achieve a better light outcoupling.

Angular Dependency measurements on encapsulated samples were performed to determine the horizontal dipole orientation. These revealed particularly high horizontal dipole orientations with 83% for the DI-DBA and 78% for the SpiroAc-DBA. Therefore, these two materials can be considered promising emitters for the application in OLEDs because a high horizontal orientation of emissive transition dipole moments can increase the light outcoupling efficiency.

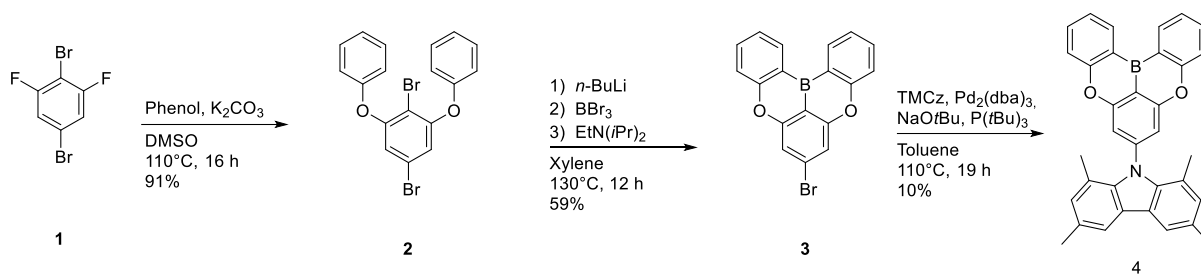
An important factor in determining the efficiency of an OLED device is the investigation of the balance of charge transport. For this purpose, single-carrier devices (electron-only EO and hole-only HO) were fabricated and analyzed. Ideally, both single-carrier devices should exhibit a similar current density at the same voltage; charge transport for holes and electrons should be balanced. However, for all samples, hole transport was at least one order of magnitude higher than electron transport. The best alignment of the two currents was obtained for the pure SpiroAc-DBA single-carrier devices. The 1:1 mixing of SpiroAc-DBA with the host material *mCBP-CN* resulted in strong decreases in the electron as well as hole current. While the mixing enhances the PLQY, it also reduces the charge transport as a result of the dilution of the emitting molecule.

Last, the single-layer OLED devices were fabricated and analyzed in order to understand the structure-property relationships. The EL spectra display quite broad emission for all three samples (74–88 nm). Interestingly, the doping of SpiroAc-DBA leads to a narrower EL spectrum showing a FWHM of only 64 nm, 10 nm less than the pure sample. Therefore, the doping of the SpiroAc-DBA in *mCBP-CN* leads to an improvement in color purity. However, as described above, the doping decreases the electron and hole current. As a result, the identification of a suitable host material for SpiroAc-DBA that not only enhances the color purity but also supports the charge transport, requires further investigations. This might result in a single-layer OLED device with good color purity as well as device efficiency.

For all fabricated devices, the OLED employing DI-DBA exhibits the lowest switch-on voltage of 2.3 V and also by far the lowest driving voltage of only 2.8 V. The device with SpiroAc-DBA:*mCBP-CN* 1:1 requires a high driving voltage of 7.1 V, which matches the strong reduction of hole and electron current caused by the mixing with the host material. Among the investigated devices, DI-DBA also achieves the highest EQE of 13%. The device with TMCz-DBA reaches an EQE of 4%; the one with SpiroAc-DBA of 5%. The doping of SpiroAc-DBA in *mCBP-CN* host material leads to a slight increase of 7%, even though the hole and electron current are reduced by the mixing. This again is a strong indication for the demand to identify a suitable host material for SpiroAc-DBA so that the charge transport is maintained at a high level, leading to an efficient single-layer device.

6. Experimental Part

6.1. Synthesis



MM01 (2,5-dibromo-1,3-di(phenyloxy)benzene)

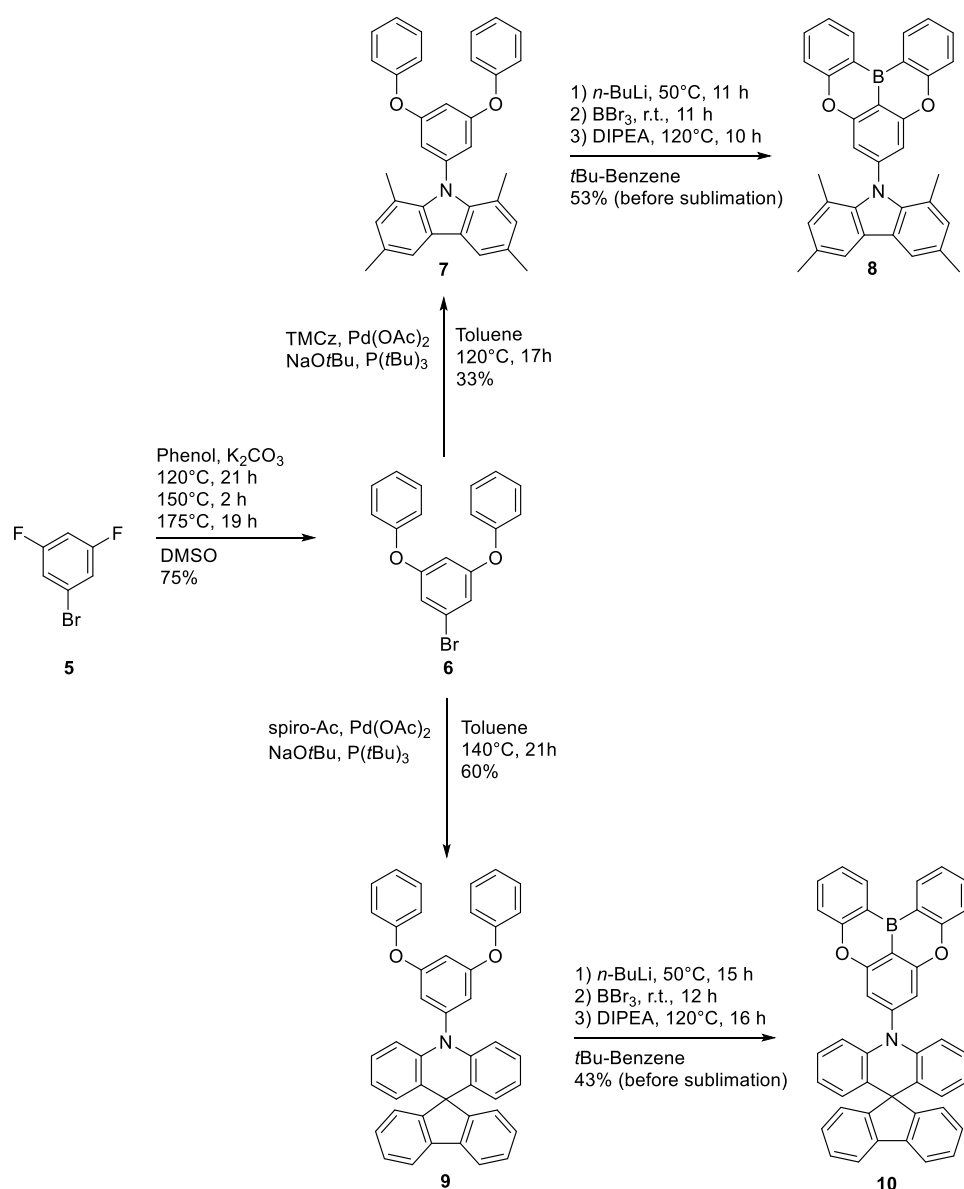
Under a nitrogen atmosphere phenol (2.57 g, 27.0 mmol, 2.9 eq.) was added to a solution of dibromo-1,3-difluorobenzene (**1**, 2.50 g, 9.2 mmol, 1 eq.) and potassium carbonate (3.80 g, 27.0 mmol, 2.9 eq.) in anhydrous DMSO (13 mL). The reaction mixture was stirred at 110 °C for 16 hours. After addition of water (20 mL), the aqueous layer was extracted with ethyl acetate (3 × 50 mL). The combined organic phases were washed with brine (50 mL) and water (50 mL), dried over anhydrous Na₂SO₄, and concentrated under reduced pressure. The crude product was purified by column chromatography (stationary phase: silica, eluent: hexane/dichloromethane = 5:1) to afford 2,5-dibromo-1,3-di(phenyloxy)benzene (**2**, 3.49 g, 8.3 mmol, 90% yield) as a colorless solid: ¹H NMR (400 MHz, CDCl₃) δ (ppm) 7.41 (t, *J* = 8.0 Hz, 4H), 7.20 (t, *J* = 8.0 Hz, 2H), 7.06 (d, *J* = 8.0 Hz, 4H), 6.76 (s, 2H); ¹³C NMR (400 MHz, CDCl₃) δ (ppm) 156.4, 155.9, 130.1, 124.5, 121.1, 119.2, 116.9, 105.9, 1.04; MS (ASAP) *m/z*: [M+1]⁺ 421.1.

MM02 (7-bromo-5,9-dioxa-13b-boranaphtho[3,2,1-de]anthracene)

To a solution of 2,5-dibromo-1,3-di(phenyloxy)benzene (**2**, 1.00 g, 2.38 mmol, 1 eq.) in anhydrous xylene (13 mL), a 1.6 M solution of *n*-butyllithium in hexane (1.5 mL, 2.62 mmol, 1.1 eq.) was added dropwise at 0 °C under a nitrogen atmosphere. After stirring at room temperature for 1 hour, boron tribromide (0.4 mL, 4.15 mmol, 1.7 eq.) was added dropwise to the mixture at -78 °C. The reaction mixture was allowed to warm to room temperature and stirred for 1 hour. *N,N*-diisopropylethylamine (DIPEA, 0.75 mL, 4.29 mmol, 1.8 eq.) was added at 0 °C. The resulting mixture was stirred at 130 °C for 15 hours and cooled in an ice bath to form precipitates. The precipitates were collected by filtration, suspended in dichloromethane (50 mL), and successively washed with a saturated aqueous solution of sodium acetate (50 mL) and water (50 mL). The organic layer was concentrated under reduced pressure. After hexane (20 mL) was added to the crude product, the resulting precipitates were collected by filtration and washed with hexane, methanol, and ethanol to afford 7-bromo-5,9-dioxa-13b-boranaphtho[3,2,1-de]anthracene (**3**, 491 mg, 1.40 mmol, 59% yield) as a colorless solid: ¹H NMR (400 MHz, CDCl₃) δ (ppm) 8.68 (dd, *J* = 7.7, 1.8 Hz, 2H), 7.73 (ddd, *J* = 8.5, 7.0, 1.7 Hz, 2H), 7.54 (dd, *J* = 8.4, 1.2 Hz, 2H), 7.45–7.36 (overlapped m, 4H); ¹³C NMR (400 MHz, CDCl₃) δ (ppm) 134.6, 133.9, 123.2, 118.6, 112.2, 77.2; MS (ASAP) *m/z*: [M+1]⁺ 351.2.

MM03 (9-[1,4]Benzoxaborino[2,3,4-kl]phenoxaborin-7-yl-1,3,6,8- tetramethyl-9H-carbazole)

To a solution of 7-bromo-5,9-dioxa-13b-boranaphtho[3,2,1-*de*]anthracene (**3**, 0.25 g, 0.71 mmol, 1 eq.), 1,3,6,8-tetramethyl-9H-carbazole (TMCz, 0.18 g, 0.80 mmol, 1.1 eq.), Pd₂(dba)₃ (0.03 g, 0.13 mmol, 0.2 eq.) and NaOtBu (0.15 g, 0.16 mmol, 0.2 eq.) in anhydrous toluene (5 mL) P(*t*Bu)₃ (0.02 g, 0.08 mmol, 0.1 eq.) was added under a nitrogen atmosphere. After stirring at 110 °C for 19 hours, water (10 mL) was added to the reaction mixture at room temperature. The combined organic phases were extracted with toluene (3 × 30 mL) and then dried over anhydrous MgSO₄. After filtration and evaporation, the crude product was purified by column chromatography (stationary phase: silica, eluent: hexane/dichloromethane = 2:1) to afford 9-[1,4]Benzoxaborino[2,3,4-kl]phenoxaborin-7-yl-1,3,6,8- tetramethyl-9H-carbazole (TMCz-DBA, **4**, 35 mg, 0.07 mmol, 10% yield) as a yellow solid: ¹H NMR (400 MHz, CDCl₃) δ (ppm) 8.75 (dd, *J* = 7.7, 1.6 Hz, 2H), 7.75 (td, *J* = 8.0, 1.2 Hz, 4H), 7.56 (dd, *J* = 8.5, 1.1 Hz, 2H), 7.44 (td, *J* = 8.0 Hz, 1.2 Hz, 2H), 7.38 (s, 2H), 6.92 (s, 2H), 2.49 (s, 6H), 1.94 (s, 6H); ¹³C NMR (400 MHz, CDCl₃) δ (ppm) 151.0, 144.4, 118.6, 117.8, 77.2, 19.4, 1.0; MS (ASAP) *m/z*: [M+1]⁺ 493.1.



MM04 (5-bromo-1,3-diphenoxybenzene)

Phenol (4.90 g, 0.07 mol, 3.3 eq.) was added to a mixture of 1-bromo-3,5-difluorobenzene (**5**, 4.00 g, 0.02 mol, 1 eq.), and K₂CO₃ (7.18 g, 0.07 mol, 3.3 eq.) in anhydrous DMSO (30 mL) at room temperature under a nitrogen atmosphere. The reaction mixture was stirred at 120 °C for 21 hours. Then, the temperature was increased to 150 °C for 2 hours and then to 175 °C for another 19 hours. The reaction mixture was allowed to cool to room temperature. After the addition of water (50 mL), the reaction solution was extracted with toluene (4 × 50 mL) and the combined organic phases were washed with brine (2 × 50 mL) and water (50 mL), dried over anhydrous MgSO₄, and then concentrated under reduced pressure. The crude product was purified by column chromatography (stationary phase: silica, eluent: hexane/dichloromethane = 4:1) to afford 5-bromo-1,3-diphenoxybenzene (**6**, 5.23 g, 0.02 mol, 75% yield) as a colorless liquid: ¹H NMR (400 MHz, CDCl₃) δ (ppm) 7.41 (td, *J* = 7.1, 1.7 Hz, 4H), 7.20 (tt, *J* = 7.4, 2.1 Hz, 2H), 7.10 (dd, *J* = 8.7, 2.1 Hz, 4H), 6.89 (d, *J* = 2.2 Hz, 2H), 6.67 (t, *J* = 2.2 Hz, 1H); ¹³C NMR (400 MHz, CDCl₃) δ (ppm) 159.5, 155.9, 130.1, 124.4, 123.2, 119.7, 115.9, 107.6; MS (ASAP) *m/z*: [M+1]⁺ 343.2.

MM05 (9-(3,5-diphenoxyphenyl)-1,3,6,8-tetramethyl-9H-carbazole)

A mixture of 5-bromo-1,3-diphenoxybenzene (**6**, 1.23 g, 3.61 mmol, 1 eq.), 1,3,6,8-tetramethyl-9H-carbazole (TMCz, 0.87 g, 3.90 mmol, 1.1 eq.), Pd(OAc)₂ (0.032 g, 0.14 mmol, 0.04 eq.), P(*t*Bu)₃ (0.04 g, 0.21 mmol, 0.06 eq.) and NaOtBu (0.413 g, 4.30 mmol, 1.2 eq.) was prepared in anhydrous and degassed toluene (140 mL) and refluxed for 17 hours under an inert atmosphere. Water (150 mL) was added to the reaction mixture, which then was extracted with dichloromethane (3 × 50 mL). The combined organic phases were dried over MgSO₄ and concentrated under reduced pressure. The crude product thus obtained was purified by column chromatography (stationary phase: silica, eluent: hexane/dichloromethane = 4:1) to afford 9-(3,5-diphenoxyphenyl)-1,3,6,8-tetramethyl-9H-carbazole (**7**, 0.58 g, 33% yield) as a colorless oily liquid: ¹H NMR (CDCl₃, 400 MHz) δ (ppm) 7.70 (dt, *J* = 1.7, 0.8 Hz, 2H), 7.35 (t, *J* = 8.0 Hz, 4H), 7.12 (ddt, *J* = 8.6, 7.3, 1.1 Hz, 2H), 7.06 (m, 4H), 6.93 (m, 2H), 6.89 (t, *J* = 2.4 Hz, 1H), 6.81 (d, *J* = 2.2 Hz, 2H), 2.46 (m, 6H), 2.08 (s, 6H); ¹³C NMR (CDCl₃, 400 MHz) δ (ppm) 158.5, 156.2, 144.2, 138.8, 130.3, 130.1, 129.0, 124.3, 124.0, 120.9, 119.6, 117.8, 115.9, 109.6, 21.1, 19.4; MS (ASAP) *m/z*: [M+1]⁺ 485.3.

MM06 (10-(3,5-diphenoxyphenyl)-10H-spiro[acridine-9,9'-fluorene])

A mixture of 5-bromo-1,3-diphenoxybenzene (**6**, 1.09 g, 3.19 mmol, 1 eq.), 10H-spiro[acridine-9,9'-fluorene] (spiro-Ac, 1.21 g, 3.64 mmol, 1.1 eq.), Pd(OAc)₂ (0.05 g, 0.20 mmol, 0.06 eq.), P(*t*Bu)₃ (0.33 g, 1.65 mmol, 0.5 eq.) and NaOtBu (0.386 g, 4.02 mmol, 1.3 eq.) was prepared in anhydrous and degassed toluene (130 mL) and refluxed for 21 hours under an inert atmosphere. Water (50 mL) was added to the reaction mixture, which then was extracted with dichloromethane (3 × 50 mL). The combined organic layer was dried over MgSO₄ and concentrated under reduced pressure. The crude product thus obtained was purified by column chromatography (stationary phase: silica, eluent: hexane/dichloromethane = 2:1) to afford 10-(3,5-diphenoxyphenyl)-10H-spiro[acridine-9,9'-fluorene] (**9**, 1.18 g, 60% yield) as a colorless oily liquid: ¹H NMR (CDCl₃, 400 MHz) δ (ppm) 7.78 (dt, *J* = 7.5, 1.0 Hz, 2H), 7.46–7.27 (m, 8H), 7.25–7.11 (m, 8H), 6.99 (ddd, *J* = 8.5, 7.1, 1.6 Hz, 2H), 6.90–6.78 (m, 3H), 6.58 (t, *J* = 8.0 Hz, 2H), 6.52 (d, *J* = 8.0 Hz, 2H), 6.38 (dd, *J* = 7.8, 1.5 Hz, 2H). ¹³C NMR (CDCl₃, 400 MHz) δ (ppm) 160.9, 156.4, 156.0, 143.2, 140.8, 139.2, 130.1, 128.4, 127.8, 127.6, 127.3, 125.8, 124.9, 124.3, 120.8, 119.9, 119.6, 115.1, 114.5, 108.7; MS (ASAP) *m/z*: [M+1]⁺ 593.6.

MM07 (10-(5,9-dioxa-13b-boranaphtho[3,2,1-de]anthracen-7-yl)-10H-spiro[acridine-9,9'-fluorene])

A 1.6 M solution of *n*-butyllithium in hexane (0.73 mL, 1.2 mmol, 1.2 eq.) was added slowly to 10-(3,5-diphenoxyphenyl)-10H-spiro[acridine-9,9'-fluorene (**9**, 0.59 g, 1.0 mmol, 1 eq.) in *t*-butylbenzene (6 mL) at 0 °C under a nitrogen atmosphere. After stirring at 50 °C for 15 hours, boron tribromide (0.14 mL, 1.5 mmol, 1.5 eq.) was added at 0 °C. After stirring at room temperature for 12 hours, *N,N*-diisopropylethylamine (DIPEA, 0.35 mL, 2.0 mmol) was added at 0 °C. After stirring at 120 °C for 16 hours, the solvent was removed in vacuo. The resulting solid was filtered with a pad of silica using toluene as an eluent. The solvent was removed in vacuo to obtain 10-(5,9-dioxa-13b-boranaphtho[3,2,1-de]anthracen-7-yl)-10H-spiro[acridine-9,9'-fluorene] (SpiroAc-DBA, **10**, 0.32 g, 53% yield) as a yellow solid that was further purified by vacuum sublimation: ¹H NMR (CDCl₃, 400 MHz) δ 8.78 (dd, *J* = 7.7, 1.7 Hz, 2H), 7.86–7.74 (m, 4H), 7.61 (dd, *J* = 8.5, 1.1 Hz, 2H), 7.53–7.36 (m, 8H), 7.31 (td, *J* = 7.4, 1.2 Hz, 2H), 6.93 (t, *J* = 8.0 Hz, 2H), 6.60 (td, *J* = 7.6, 1.2 Hz, 2H), 6.52 (d, *J* = 8.3 Hz, 2H), 6.45 (dd, *J* = 7.8, 1.6 Hz, 2H); ¹³C NMR (CDCl₃, 400 MHz) δ 134.7, 134.1, 128.5, 127.8, 127.7, 127.3, 125.9, 123.3, 121.0, 120.0, 77.2; MS (ASAP) *m/z*: [M+1]⁺ 600.8.

MM08 (9-[1,4]Benzoxaborino[2,3,4-*k*]phenoxaborin-7-yl-1,3,6,8-tetramethyl-9H-carbazole)

A 1.6 M solution of *n*-butyllithium in hexane (0.61 mL, 1.0 mmol, 1.2 eq.) was added slowly to 9-(3,5-diphenoxyphenyl)-1,3,6,8-tetramethyl-9H-carbazole (**7**, 0.40 g, 0.8 mmol, 1 eq.) in *t*-butylbenzene (6 mL) at 0 °C under a nitrogen atmosphere. After stirring at 50 °C for 11 hours, boron tribromide (0.12 mL, 1.3 mmol, 1.6 eq.) was added at 0 °C. After stirring at room temperature for 11 hours, *N,N*-diisopropylethylamine (DIPEA, 0.29 mL, 1.7 mmol, 2.2 eq.) was added at 0 °C. After stirring at 120 °C for 10 hours, the solvent was removed in vacuo. The resulting solid was filtered through a pad of silica using toluene as an eluent. After the solvent was removed in vacuo, the crude product was washed with acetonitrile to obtain 9-[1,4]Benzoxaborino[2,3,4-*k*]phenoxaborin-7-yl-1,3,6,8-tetramethyl-9H-carbazole (TMCz-DBA, **8**, 0.176 g, 43% yield) as a yellow solid that was further purified by vacuum sublimation. ¹H NMR (CDCl₃, 400 MHz) δ 8.75 (dd, *J* = 7.8, 1.7 Hz, 2H), 7.80–7.71 (m, 4H), 7.56 (dd, *J* = 8.4, 1.1 Hz, 2H), 7.44 (ddd, *J* = 8.0, 7.1, 1.1 Hz, 2H), 7.38 (s, 2H), 6.92 (d, *J* = 1.7 Hz, 2H), 2.49 (s, 6H), 1.94 (s, 6H); ¹³C NMR (CDCl₃, 400 MHz) δ 156.9, 134.7, 134.0, 130.3, 129.3, 123.2, 121.5, 118.6, 112.0, 77.2, 21.1, 19.3; MS (ASAP) *m/z*: [M+1]⁺ 493.8.

6.2. Methods

Chemicals: For synthesis, all chemicals and solvents were purchased by Sigma Aldrich, Fisher Scientific and TCI and used without further purification.

For device fabrication, C₆₀, TPBi and the PFI solution were purchased by Sigma Aldrich; MoO₃ was purchased by Fisher Scientific and PEDOT:PSS was purchased by Clevio. Di-DBA was obtained from Luminescence Technology Corporation and used without further purification.

Thin-layer chromatography: For qualitative thin-layer chromatography, ALUGRAM® SIL G/UV254 (MACHEREY-NAGEL) plates were used with 0.20 mm of silica oxide on aluminum sheets as the stationary phase. Fluorescent compounds were detected under irradiation with a UV-lamp at wavelengths of 254 nm or 365 nm.

Column chromatography: For column chromatography, silica gel 60 (size 40 – 63 μm) (MACHEREY-NAGEL) was used as stationary phase. Solids were placed on the silica gel as dry load absorbed in silica gel or as solution in DCM.

Mass spectrometry: APCI-MS spectra were measured with an expression® compact mass spectrometer (CMS) from Advion. The resulted spectra were processed with the computer program Data Express 4.0.13.8 from Advion.

Nuclear magnetic resonance spectroscopy (NMR): NMR spectra were measured with a Bruker 300 MHz NMR Spectrometer Avance. The analytics were obtained with MestReNova 14.1.1 (Mestrelab).

Spectroscopic Characterization: All measurements (Luminescence, UV/Vis Absorption, TRPL) were carried out at room temperature. For solution measurements, 10^{-6} M degassed solution of DI-DBA, TMCz-DBA and SpiroAc-DBA in toluene was used for steady-state UV/Vis absorption and photoluminescence (PL). The measurements were done in a 2 mm path length quartz cuvette. For film measurements, a neat film (95 nm) was deposited on top of a quartz substrate.

Luminescence spectroscopy: To record photoluminescence quantum yields (PLQYs) and photoluminescence (PL) spectra, a HORIBA Jobin Yvon Fluorolog-3 spectrofluorometer was used with the FluorEssence computer software, using 380 nm excitation wavelength for all samples.

UV/Vis spectroscopy: The steady-state UV/Vis absorption measurements were recorded using a PerkinElmer Lambda 900 UV/VIS/NIR Spectrometer.

Time-resolved photoluminescence spectroscopy (TRPL): For TRPL measurements, the solid-state samples were excited at 400 nm with a Ti: sapphire laser (Coherent, Astrella), paired a commercial optical parametric amplifier (Coherent, OperA). Measurements were performed with a 4Picos gated-iCCD camera from Stanford Computer Optics. The spectra were collected using the 4Spec computer software (Stanford Computer Optics). The photoexcitation light was focused onto the sample in order to ensure a uniform excitation density throughout the film. The laser beam was focused onto the sample with a spot size of 0.8 mm; the focus was checked with a Coherent LaserCam-Hr II beam profiler was used.

Optical Characterization: The refractive indices of DI-DBA, SpiroAc-DBA and TMCz-DBA were experimentally determined by a variable angle spectroscopic ellipsometer (Alpha-SE, Quantum Design GmbH), and the dipole orientations of the neat film samples were determined with a Fluxim Phelos gonio-spectrometer, by fitting the angular dependence of photoluminescence with Setfos software from Fluxim.

Theoretical calculations: Theoretical calculations were performed with the software Gaussian 09. For the three emitters (DI-DBA, TMCz-DBA and SpiroAc-DBA), the optimization of the ground-state structure was performed with the DFT method with the B3LYP functional with 6-31G basis set. The S_1 and T_1 energies were calculated based on a TD-DFT approach at a B3LYP/6-31G level. The distribution of the HOMOs and LUMOs was visualized on the GaussView 5.0 software.

OLED Fabrication: Glass substrates and ITO (120 nm)-covered glass substrates were thoroughly cleaned with detergent solution, followed with ultrasonic bath in acetone and isopropyl alcohol for each five minutes. Subsequently, the ITO substrates were treated by UV-ozone for 50 minutes; the glass substrates at least for 20 minutes. A layer of poly(3,4-ethylenedioxythio-phenylene):polystyrene sulfonate:perfluorinated ionomer (PEDOT:PSS:PFI) was spin coated and annealed at 135 °C for 10 min in air. The substrates were then transferred into evaporation chambers. The MoO₃, the Ba and the Al layers were evaporated at a pressure less than $5 \cdot 10^{-7}$ mbar. The organic layers were evaporated at a pressure of less than $3 \cdot 10^{-6}$ mbar. Organic functional materials and inorganic layers were deposited in separate chambers. The evaporation rates and layer thicknesses were tracked by quartz crystal monitors. For the different devices (HOs, EOs and OLEDs) different layers were evaporated. The order of the different layers is shown in Chapter 3: These are 5 nm barium, 7 nm MoO₃, 4 nm C₆₀, 95–110 nm emitter (DI-DBA, TMCz-DBA, SpiroAc-DBA, SpiroAc-DBA/mCBP-CN) and 4 nm TPBi that were thermally deposited for the experimental devices investigated in this work. A 100 nm aluminum layer was deposited as the cathode as well as an oxidated 30 nm aluminum layer as

the anode in the EO devices. The devices were characterized in a nitrogen-filled glove box without further encapsulation.

Device Characterization: The current density-voltage characterization was carried out with a Keithley 2400 source meter, while the light output was recorded simultaneously with a (NIST traceable) calibrated Si photodiode with an area larger than the emissive pixel, placed in close proximity to the emitting surface in order to capture all light emitted in the forward hemisphere. The substrate edges of the OLEDs were sealed by the sample holder to avoid detection of the waveguided light from the substrate mode. EL spectra were obtained with a USB4000-UV-VIS-ES spectrometer at different driving voltages. The luminance, EQE, and power efficiency was calculated according to a previously published method.^[75,77]

7. References

- [1] *Organic Light-Emitting Diodes*; Woodhead Publishing: 2013, p. 447.
- [2] Hong, Gloria; Gan, Xuemin; Leonhardt, Céline; Zhang, Zhen; Seibert, Jasmin; Busch, Jasmin M.; Bräse, Stefan. A Brief History of OLEDs-Emitter Development and Industry Milestones. *Advanced materials (Deerfield Beach, Fla.)* **2021**, 33 (9) e2005630.
- [3] Webster, John G. *Wiley Encyclopedia of Electrical and Electronics Engineering*; Wiley: 2000.
- [4] Craford, M. G. in Fifth International Conference on Solid State Lighting, Vol. 5941.
- [5] *International Society for Optics and Photonics*, 2005, p. 594101.
- [6] Leonova, M. S.; Timofeeva, S. S. Environmental and economic damage from the dust waste formation in the silicon production. *IOP Conference Series: Earth and Environmental Science* **2019**, 22912022.
- [7] Wong, Michael Y.; Zysman-Colman, Eli. Purely Organic Thermally Activated Delayed Fluorescence Materials for Organic Light-Emitting Diodes. *Advanced materials (Deerfield Beach, Fla.)* **2017**, 29 (22).
- [8] Rothberg, Lewis J.; Lovinger, Andrew J. Status of and prospects for organic electroluminescence. *Journal of Materials Research* **1996**, 11 (12) 3174–3187.
- [9] Baldo, M. A.; O'Brien, D. F.; You, Y.; Shoustikov, A.; Sibley, S.; Thompson, M. E.; Forrest, S. R. Highly efficient phosphorescent emission from organic electroluminescent devices. *Nature* **1998**, 395 (6698) 151–154.
- [10] Thompson, Mark. The Evolution of Organometallic Complexes in Organic Light-Emitting Devices. *MRS Bulletin* **2007**, 32 (9) 694–701.
- [11] Adachi, Chihaya; Baldo, Marc A.; Thompson, Mark E.; Forrest, Stephen R. Nearly 100% internal phosphorescence efficiency in an organic light-emitting device. *Journal of Applied Physics* **2001**, 90 (10) 5048–5051.
- [12] Adachi, Chihaya; Baldo, Marc A.; Forrest, Stephen R.; Thompson, Mark E. High-efficiency organic electrophosphorescent devices with tris(2-phenylpyridine)iridium doped into electron-transporting materials. *Applied Physics Letters* **2000**, 77 (6) 904–906.
- [13] Bottin, François; Finocchi, Fabio; Noguera, Claudine. Stability and electronic structure of the (1×1)SrTiO₃(110) polar surfaces by first-principles calculations. *Physical Review B* **2003**, 68 (3).
- [14] Wallikewitz, Bodo H.; Kabra, Dinesh; Gélinas, Simon; Friend, Richard H. Triplet dynamics in fluorescent polymer light-emitting diodes. *Physical Review B* **2012**, 85 (4).
- [15] Baldo, M. A.; Adachi, C.; Forrest, S. R. Transient analysis of organic electrophosphorescence. II. Transient analysis of triplet-triplet annihilation. *Physical Review B* **2000**, 62 (16) 10967–10977.
- [16] Uoyama, Hiroki; Goushi, Kenichi; Shizu, Katsuyuki; Nomura, Hiroko; Adachi, Chihaya. Highly efficient organic light-emitting diodes from delayed fluorescence. *Nature* **2012**, 492 (7428) 234–238.
- [17] Dias, Fernando B.; Penfold, Thomas J.; Monkman, Andrew P. Photophysics of thermally activated delayed fluorescence molecules. *Methods and applications in fluorescence* **2017**, 5 (1) 12001.

- [18] Marini, Alberto; Muñoz-Losa, Aurora; Biancardi, Alessandro; Mennucci, Benedetta. What is solvatochromism? *The journal of physical chemistry. B* **2010**, *114* (51) 17128–17135.
- [19] Grabowski, Zbigniew R.; Rotkiewicz, Krystyna; Rettig, Wolfgang. Structural changes accompanying intramolecular electron transfer: focus on twisted intramolecular charge-transfer states and structures. *Chemical reviews* **2003**, *103* (10) 3899–4032.
- [20] Dias, Fernando B.; Pollock, Sam; Hedley, Gordon; Pålsson, Lars-Olof; Monkman, Andy; Perepichka, Irene I.; Perepichka, Igor F.; Tavasli, Mustafa; Bryce, Martin R. Intramolecular charge transfer assisted by conformational changes in the excited state of fluorene-dibenzothiophene-S,S-dioxide co-oligomers. *The journal of physical chemistry. B* **2006**, *110* (39) 19329–19339.
- [21] Parker, C. A.; Hatchard, C. G. Triplet-singlet emission in fluid solutions. Phosphorescence of eosin. *Transactions of the Faraday Society* **1961**, 571894.
- [22] Blasse, George; McMillin, David R. On the luminescence of bis (triphenylphosphine) phenanthroline copper (I). *Chemical Physics Letters* **1980**, *70* (1) 1–3.
- [23] Tang, C. W.; VanSlyke, S. A. Organic electroluminescent diodes. *Applied Physics Letters* **1987**, *51* (12) 913–915.
- [24] Endo, Ayataka; Ogasawara, Mai; Takahashi, Atsushi; Yokoyama, Daisuke; Kato, Yoshimine; Adachi, Chihaya. Thermally activated delayed fluorescence from Sn(4+)-porphyrin complexes and their application to organic light emitting diodes--a novel mechanism for electroluminescence. *Advanced materials (Deerfield Beach, Fla.)* **2009**, *21* (47) 4802–4806.
- [25] Quirino, W. G.; Teixeira, K. C.; Legnani, C.; Calil, V. L.; Messer, B.; Neto, O. Vilela P.; Pacheco, M.A.C.; Cremona, M. Improved multi-layer OLED architecture using evolutionary genetic algorithm. *Thin Solid Films* **2009**, *518* (5) 1382–1385.
- [26] Kotadiya, Naresh B.; Blom, Paul W. M.; Wetzelaer, Gert-Jan A. H. Efficient and stable single-layer organic light-emitting diodes based on thermally activated delayed fluorescence. *Nature Photonics* **2019**, *13* (11) 765–769.
- [27] Li, Yungui; Tang, Zheng; Hänisch, Christian; Will, Paul-Anton; Kovačič, Milan; Hou, Ji-Ling; Scholz, Reinhard; Leo, Karl; Lenk, Simone; Reineke, Sebastian; et al. Ultrathin MoO₃ Layers in Composite Metal Electrodes: Improved Optics Allow Highly Efficient Organic Light-Emitting Diodes. *Advanced Optical Materials* **2019**, *7* (3) 1801262.
- [28] Li, Yungui; Wei, Qiang; Cao, Liang; Fries, Felix; Cucchi, Matteo; Wu, Zhongbin; Scholz, Reinhard; Lenk, Simone; Voit, Brigitte; Ge, Ziyi; et al. Organic Light-Emitting Diodes Based on Conjugation-Induced Thermally Activated Delayed Fluorescence Polymers: Interplay Between Intra- and Intermolecular Charge Transfer States. *Frontiers in chemistry* **2019**, 7688.
- [29] Kotadiya, Naresh B.; Lu, Hao; Mondal, Anirban; Ie, Yutaka; Andrienko, Denis; Blom, Paul W. M.; Wetzelaer, Gert-Jan A. H. Universal strategy for Ohmic hole injection into organic semiconductors with high ionization energies. *Nature materials* **2018**, *17* (4) 329–334.
- [30] Kotadiya, Naresh B.; Mondal, Anirban; Blom, Paul W. M.; Andrienko, Denis; Wetzelaer, Gert-Jan A. H. A window to trap-free charge transport in organic semiconducting thin films. *Nature materials* **2019**, *18* (11) 1182–1186.
- [31] Brown, Herbert C.; Dodson, Vance H. Studies in Stereochemistry. XXII. The Preparation and Reactions of Trimesitylborane. Evidence for the Non-localized Nature of the Odd Electron in Triarylborane Radical Ions and Related Free Radicals 1. *Journal of the American Chemical Society* **1957**, *79* (9) 2302–2306.
- [32] Yamaguchi, Shigehiro; Wakamiya, Atsushi. Boron as a key component for new π -electron materials. *Pure and Applied Chemistry* **2006**, *78* (7) 1413–1424.
- [33] Elbing, Mark; Bazan, Guillermo C. A new design strategy for organic optoelectronic materials by lateral boryl substitution. *Angewandte Chemie (International ed. in English)* **2008**, *47* (5) 834–838.

- [34] von Grotthuss, Esther; John, Alexandra; Kaese, Thomas; Wagner, Matthias. Doping Polycyclic Aromatics with Boron for Superior Performance in Materials Science and Catalysis. *Asian Journal of Organic Chemistry* **2018**, 7 (1) 37–53.
- [35] D'Aléo, A.; Sazzad, M. H.; Kim, D. H.; Choi, E. Y.; Wu, J. W.; Canard, G.; Fages, F.; Ribierre, J-C; Adachi, C. Boron difluoride hemicurcuminoid as an efficient far red to near-infrared emitter: toward OLEDs and laser dyes. *Chemical communications (Cambridge, England)* **2017**, 53 (52) 7003–7006.
- [36] Yang, Xiaolong; Guo, Haoran; Liu, Boao; Zhao, Jiang; Zhou, Guijiang; Wu, Zhaoxin; Wong, Wai-Yeung. Erratum: Diarylboron-Based Asymmetric Red-Emitting Ir(III) Complex for Solution-Processed Phosphorescent Organic Light-Emitting Diode with External Quantum Efficiency above 28. *Advanced science (Weinheim, Baden-Wuerttemberg, Germany)* **2018**, 5 (7) 1800950.
- [37] Zhang, Yuewei; Zhang, Dongdong; Wei, Jinbei; Liu, Ziyang; Lu, Yang; Duan, Lian. Multi-Resonance Induced Thermally Activated Delayed Fluorophores for Narrowband Green OLEDs. *Angewandte Chemie International Edition* **2019**, 58 (47) 16912–16917.
- [38] Hatakeyama, Takuji; Shiren, Kazushi; Nakajima, Kiichi; Nomura, Shintaro; Nakatsuka, Soichiro; Kinoshita, Keisuke; Ni, Jingping; Ono, Yohei; Ikuta, Toshiaki. Ultrapure Blue Thermally Activated Delayed Fluorescence Molecules: Efficient HOMO-LUMO Separation by the Multiple Resonance Effect. *Advanced materials (Deerfield Beach, Fla.)* **2016**, 28 (14) 2777–2781.
- [39] Ahn, Dae Hyun; Maeng, Jee Hyun; Lee, Hyuna; Yoo, Hanjong; Lampande, Raju; Lee, Ju Young; Kwon, Jang Hyuk. Rigid Oxygen-Bridged Boron-Based Blue Thermally Activated Delayed Fluorescence Emitter for Organic Light-Emitting Diode: Approach towards Satisfying High Efficiency and Long Lifetime Together. *Advanced Optical Materials* **2020**, 8 (11) 2000102.
- [40] Wetzelaer, G. A. H.; Kuik, M.; Nicolai, H. T.; Blom, P. W. M. Trap-assisted and Langevin-type recombination in organic light-emitting diodes. *Physical Review B* **2011**, 83 (16).
- [41] Jolt Oostra, A.; Blom, Paul W.M.; Michels, Jasper J. Prevention of short circuits in solution-processed OLED devices. *Organic Electronics* **2014**, 15 (6) 1166–1172.
- [42] Shockley, W. The Theory of p-n Junctions in Semiconductors and p-n Junction Transistors. *Bell System Technical Journal* **1949**, 28 (3) 435–489.
- [43] Wetzelaer, G. A. H.; Koster, L. J. A.; Blom, P. W. M. Validity of the Einstein relation in disordered organic semiconductors. *Physical review letters* **2011**, 107 (6) 66605.
- [44] Harada, K.; Werner, A. G.; Pfeiffer, M.; Bloom, C. J.; Elliott, C. M.; Leo, K. Organic homojunction diodes with a high built-in potential: interpretation of the current-voltage characteristics by a generalized Einstein relation. *Physical review letters* **2005**, 94 (3) 36601.
- [45] Poriel, Cyril; Rault-Berthelot, Joëlle. Blue Single-Layer Organic Light-Emitting Diodes Using Fluorescent Materials: A Molecular Design View Point. *Advanced Functional Materials* **2020**, 30 (17) 1910040.
- [46] Röhr, Jason A.; Kirchartz, Thomas; Nelson, Jenny. On the correct interpretation of the low voltage regime in intrinsic single-carrier devices. *Journal of physics. Condensed matter : an Institute of Physics journal* **2017**, 29 (20) 205901.
- [47] Köhler, Anna; Bäessler, Heinz. *Electronic Processes in Organic Semiconductors*; Wiley: 2015.
- [48] Li, Yungui; Kotadiya, Naresh B.; Zee, Bas; Blom, Paul W. M.; Wetzelaer, Gert-Jan A. H. Optical Outcoupling Efficiency of Organic Light-Emitting Diodes with a Broad Recombination Profile. *Advanced Optical Materials* **2021**, 9 (11) 2001812.
- [49] Burin, Alexander L.; Ratner, Mark A. Exciton Migration and Cathode Quenching in Organic Light Emitting Diodes. *The Journal of Physical Chemistry A* **2000**, 104 (20) 4704–4710.
- [50] Tenopala-Carmona, Francisco; Lee, Oliver S.; Crovini, Ettore; Neferu, Ana M.; Murawski, Caroline; Olivier, Yoann; Zysman-Colman, Eli; Gather, Malte C. Identification of the Key Parameters for Horizontal Transition Dipole Orientation in Fluorescent and TADF Organic Light-Emitting Diodes. *Advanced materials (Deerfield Beach, Fla.)* **2021**, 33 (37) e2100677.

- [51] Furno, Mauro; Meerheim, Rico; Hofmann, Simone; Lüssem, Björn; Leo, Karl. Efficiency and rate of spontaneous emission in organic electroluminescent devices. *Physical Review B* **2012**, *85* (11).
- [52] Salehi, Amin; Fu, Xiangyu; Shin, Dong-Hun; So, Franky. Recent Advances in OLED Optical Design. *Advanced Functional Materials* **2019**, *29* (15) 1808803.
- [53] Pauling, Linus. Electronic Processes in Ionic Crystals. By N. F. Mott and R. W. Gurney. *The Journal of Physical Chemistry* **1941**, *45* (7) 1142.
- [54] Wetzelaer, G.A.H. Improved Determination of the Mobility and Built-In Voltage in Asymmetric Single-Carrier Devices. *Physical Review Applied* **2020**, *13* (3.), 034069-1.
- [55] Zhen, Chang-Gua; Dai, Yan-Feng; Zeng, Wen-Jin; Ma, Zhun; Chen, Zhi-Kuan; Kieffer, John. Achieving Highly Efficient Fluorescent Blue Organic Light-Emitting Diodes Through Optimizing Molecular Structures and Device Configuration. *Advanced Functional Materials* **2011**, *21* (4) 699–707.
- [56] Tang, Shi; Li, Weijun; Shen, Fangzhong; Liu, Dandan; Yang, Bing; Ma, Yuguang. Highly efficient deep-blue electroluminescence based on the triphenylamine-cored and peripheral blue emitters with segregative HOMO–LUMO characteristics. *J. Mater. Chem.* **2012**, *22* (10) 4401–4408.
- [57] Lim, Bee T.; Okajima, S.; Chandra, A. K.; Lim, E. C. Radiationless transitions in electron donor-acceptor complexes: selection rules for S1 → T intersystem crossing and efficiency of S1 → S0 internal conversion. *Chemical Physics Letters* **1981**, *79* (1) 22–27.
- [58] Thakur, Kalyani; van der Zee, Bas; Wetzelaer, Gert-Jan A. H.; Ramanan, Charusheela; Blom, Paul W. M. Quantifying Exciton Annihilation Effects in Thermally Activated Delayed Fluorescence Materials. *Advanced Optical Materials* **2022**, *10* (3.), 2101784.
- [59] Numata, Masaki; Yasuda, Takuma; Adachi, Chihaya. High efficiency pure blue thermally activated delayed fluorescence molecules having 10H-phenoxaborin and acridan units. *Chemical communications (Cambridge, England)* **2015**, *51* (46) 9443–9446.
- [60] Louie, Janis; Hartwig, John F. Palladium-catalyzed synthesis of arylamines from aryl halides. Mechanistic studies lead to coupling in the absence of tin reagents. *Tetrahedron Letters* **1995**, *36* (21) 3609–3612.
- [61] Forero-Cortés, Paola A.; Haydl, Alexander M. The 25th Anniversary of the Buchwald–Hartwig Amination: Development, Applications, and Outlook. *Organic Process Research & Development* **2019**, *23* (8) 1478–1483.
- [62] Naveen, Kenkera Rayappa; Lee, Hyuna; Braveenth, Ramanaskanda; Karthik, Durai; Yang, Ki Joon; Hwang, Soon Jae; Kwon, Jang Hyuk. Achieving High Efficiency and Pure Blue Color in Hyperfluorescence Organic Light Emitting Diodes using Organo-Boron Based Emitters. *Advanced Functional Materials* **2022**, *32* (12.).
- [63] Kim, Jong Uk; Park, In Seob; Chan, Chin-Yiu; Tanaka, Masaki; Tsuchiya, Youichi; Nakanotani, Hajime; Adachi, Chihaya. Nanosecond-time-scale delayed fluorescence molecule for deep-blue OLEDs with small efficiency rolloff. *Nature communications* **2020**, *11* (1) 1765.
- [64] Pei, Ranran; Liu, He; Zhou, Changjiang; Miao, Jingsheng; Yang, Chuluo. Efficient blue thermally activated delayed fluorescent emitters based on a boranaphtho[3,2,1-de]anthracene acceptor. *Journal of Materials Chemistry C* **2021**, *9* (47) 17136–17142.
- [65] Kim, Changhae Andrew; Hu, Shicheng; van Voorhis, Troy. Mechanism of Enhanced Triplet-Triplet Upconversion in Organic Molecules. *The journal of physical chemistry. A* **2023**.
- [66] Tauc, J.; Grigorovici, R.; Vancu, A. Optical Properties and Electronic Structure of Amorphous Germanium. *physica status solidi (b)* **1966**, *15* (2) 627–637.
- [67] Makuła, Patrycja; Pacia, Michał; Macyk, Wojciech. How To Correctly Determine the Band Gap Energy of Modified Semiconductor Photocatalysts Based on UV-Vis Spectra. *The journal of physical chemistry letters* **2018**, *9* (23) 6814–6817.

- [68] Kim, Jin Hong; Schembri, Tim; Bialas, David; Stolte, Matthias; Würthner, Frank. Slip-Stacked J-Aggregate Materials for Organic Solar Cells and Photodetectors. *Advanced materials (Deerfield Beach, Fla.)* **2022**, 34 (22) e2104678.
- [69] Song, Xiangang; Shen, Shaogang; Zou, Shengnan; Guo, Fengyun; Wang, Ying; Gao, Shiyong; Zhang, Yong. Efficient narrowband organic light-emitting devices based on multi-resonance TADF emitters with secondary donor. *Chemical Engineering Journal* **2023**, 467143557.
- [70] Ihn, Soo-Ghang; Lee, Namheon; Jeon, Soon Ok; Sim, Myungsun; Kang, Hosuk; Jung, Yongsik; Huh, Dal Ho; Son, Young Mok; Lee, Sae Youn; Numata, Masaki; et al. An Alternative Host Material for Long-Lifespan Blue Organic Light-Emitting Diodes Using Thermally Activated Delayed Fluorescence. *Advanced science (Weinheim, Baden-Wuerttemberg, Germany)* **2017**, 4 (8) 1600502.
- [71] Ma, Suqian; Du, Sijia; Pan, Guocui; Dai, Shuting; Xu, Bin; Tian, Wenjing. Organic molecular aggregates: From aggregation structure to emission property. *Aggregate* **2021**, 2 (4).
- [72] Abdel-Shafi, Ayman A.; Worrall, David R. Mechanism of the excited singlet and triplet states quenching by molecular oxygen in acetonitrile. *Journal of Photochemistry and Photobiology A: Chemistry* **2005**, 172 (2) 170–179.
- [73] Méhes, Gábor; Goushi, Kenichi; Potscavage, William J.; Adachi, Chihaya. Influence of host matrix on thermally-activated delayed fluorescence: Effects on emission lifetime, photoluminescence quantum yield, and device performance. *Organic Electronics* **2014**, 15 (9) 2027–2037.
- [74] Fan, Xiao-Chun; Wang, Kai; Shi, Yi-Zhong; Sun, Dian-Ming; Chen, Jia-Xiong; Huang, Feng; Wang, Hui; Yu, Jia; Lee, Chun-Sing; Zhang, Xiao-Hong; et al. Thermally activated delayed fluorescence materials for nondoped organic light-emitting diodes with nearly 100% exciton harvest. *SmartMat* **2023**, 4 (1).
- [75] Forrest, S. R.; Bradley, D.D.C.; Thompson, M. E. Measuring the Efficiency of Organic Light-Emitting Devices. *Advanced Materials* **2003**, 15 (13) 1043–1048.
- [76] Regnat, Markus; Moon, Chang-Ki; Jenatsch, Sandra; Ruhstaller, Beat; Pernstich, Kurt P. Pinpointing the origin of the increased driving voltage during prolonged operation in a phosphorescent OLED based on an exciplex host. *Organic Electronics* **2022**, 108106570.
- [77] Anaya, Miguel; Rand, Barry P.; Holmes, Russell J.; Credgington, Dan; Bolink, Henk J.; Friend, Richard H.; Wang, Jianpu; Greenham, Neil C.; Stranks, Samuel D. Best practices for measuring emerging light-emitting diode technologies. *Nature Photonics* **2019**, 13 (12) 818–821.

8. List of Figures

Figure 1.1. DI-DBA molecule and electron density for HOMO and LUMO orbital.	3
Figure 2.1. Simplified bondage configuration of p_z - π conjugation of B–C bond in organic conjugated π -systems.....	4
Figure 2.2. Principle of MR-TADF compounds.	5
Figure 2.3. Target molecules DI-DBA, SpiroAc-DBA and TMCz-DBA.....	6
Figure 3.1. Current density versus Voltage Luminance (JVL) plot for a single-layer OLED of 5,10-Bis(4-(9H-carbazol-9-yl)-2,6-dimethylphenyl)-5,10-dihydroboranthrene (CzDBA) in semi-log scale. Data provided by Oskar Sachnik.	7
Figure 3.2. Jablonski diagram for electrical excitation of electrons.	8
Figure 3.3. Spin statistics for exciton formation as a result of charge recombination of two species with spin 1/2 (electrons and electron holes). Reproduced according to Ref. [47].	9
Figure 3.4. a) Centered and b) towards the cathode shifted charge recombination in OLEDs due to balanced and hole-dominated charge transport.....	9
Figure 3.5. Band diagram of a conventional multi-layer OLED device.	10
Figure 3.6. Overview of the structure and different modes with refractive indices of the layers in a multi-layer OLED device. The Figure is following Ref. [48].	10
Figure 3.7. a) Device architecture and b) schematic band diagram of the single-layer OLEDs in this work.	12
Figure 3.8. Schematic band diagrams (work functions) of the a) HO and b) EO devices and the corresponding band diagrams at the thermal equilibrium (c) and d)).	12
Figure 3.9. General architectures of single-carrier devices: a) HO device architecture; b) EO device architecture.	13
Figure 3.10. Current density versus voltage plot for a HO device of 5,10-Bis(4-(9H-carbazol-9-yl)-2,6-dimethylphenyl)-5,10-dihydroboranthrene (CzDBA) on a) semi-log scale b) log-log scale. Data provided by Oskar Sachnik.....	14
Figure 3.11. Current density versus voltage plot for an electron-only device of 10-(4-(4,6-diphenyl-1,3,5-triazin-2-yl)phenyl)-10H-spiro[acridine-9,9'-fluorene] SpiroAc-Trz on a) semi-log scale b) log-log scale. Data provided by Oskar Sachnik.	14
Figure 3.12. Jablonski diagram for first-generation OLEDs using only fluorescent organic emitters. ...	15
Figure 3.13. Jablonski diagram for second-generation OLEDs using phosphorescent emitters.	16
Figure 3.14. Jablonski diagram for a TADF emitter.	16
Figure 3.15. Bi-exponential decay curve of the TADF material 5,10-Bis(4-(9H-carbazol-9-yl)-2,6-dimethylphenyl)-5,10-dihydroboranthrene (CzDBA) taken from Ref. [58].	17
Figure 3.16. Catalyst cycle of the Buchwald-Hartwig amination.....	18
Figure 4.1. Graphical determination of the a) HOMO levels and b) LUMO levels of DI-DBA, SpiroAc-DBA and TMCz-DBA.....	21
Figure 4.2. UV/Vis absorption spectra of a) evaporated films and b) in 10^{-5} M toluene solutions of the compounds DI-DBA, TMCz-DBA and SpiroAc-DBA.	23
Figure 4.3. PL Emission spectra of a) evaporated films and b) of 10^{-5} M Toluene solutions of the compounds DI-DBA, TMCz-DBA and SpiroAc-DBA.	24
Figure 4.4. Solvatochromism for a) SpiroAc-DBA and b) TMCz-DBA.....	26
Figure 4.5. TRPL Measurements on a) DI-DBA, (b) SpiroAc-DBA and c) TMCz-DBA pristine evaporated films (95 nm).....	26
Figure 4.6. Refractive indices n_D, i of DI-DBA, SpiroAc-DBA and TMCz-DBA in dependence on the wavelength.....	27

Figure 4.7. Comparison of HO (grey) and EO (blue) devices of a) DI-DBA, b) TMCz-DBA, c) SpiroAc-DBA and d) SpiroAc-DBA:mCBP-CN 1:1 in order to compare its charge transport properties. The EMLs have a thickness of 95 nm except TMCz-DBA with 110 nm.29

Figure 4.8. JVL curves of a) DI-DBA, b) TMCz-DBA, c) SpiroAc-DBA and d) SpiroAc-DBA/mCBP-CN 1:1. The EMLs have a thickness of 95 nm.31

Figure 4.9. External quantum efficiency (EQE) and power efficiency curves of a) DI-DBA, b) TMCz-DBA, c) SpiroAc-DBA and d) SpiroAc-DBA/mCBP-CN 1:1. The EMLs have a thickness of 95 nm.32

9. List of Tables

Table 4.1. Energy levels for DI-DBA, TMCz-DBA and SpiroAc-DBA. (Optimization: Ground-State DFT, B3LYP, 6–31G basis set with d and p orbitals, Energy: TD-SCF with singlet and triplet states)19

Table 4.2. Lowest energy levels $T1$, $T2$, $S1$ and $S2$ for DI-DBA (determined by DFT).20

Table 4.3. HOMO, LUMO distributions and calculated and experimental energies.22

Table 4.4. Summary of the photophysical properties of DI-DBA, TMCz-DBA and SpiroAc-DBA.....25

Table 4.5. Lifetimes of prompt τ_{PF} and delayed τ_{DF} fluorescence for DI-DBA, SpiroAc-DBA and TMCz-DBA.27

Table 4.6. Horizontal dipole orientations of DI-DBA, TMCz-DBA and SpiroAc-DBA.....28

Table 4.7. Characteristics of the EL inside the devices for DI-DBA, TMCz-DBA, SpiroAc-DBA and SpiroAc-DBA:mCBP-CN (1:1).30

Table 4.8. Summary of the device parameters of the single-layer devices of DI-DBA, TMCz-DBA, SpiroAc-DBA and SpiroAc-DBA in mCBP-CN (1:1).....32

10. Appendix

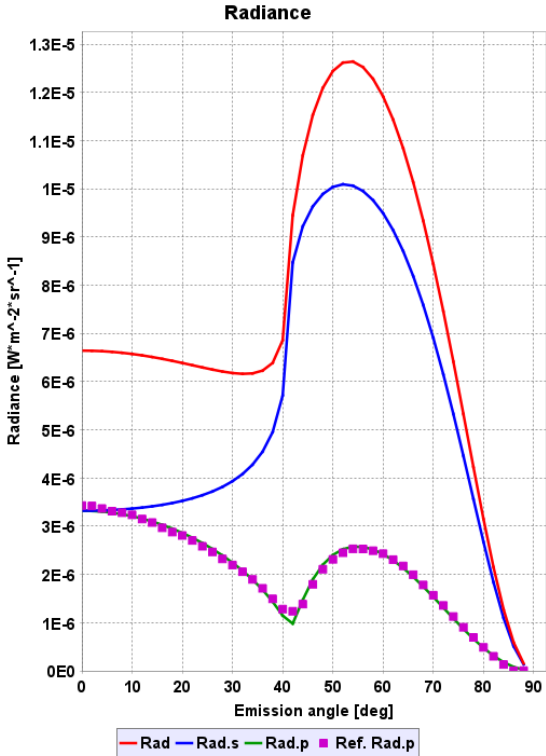


Figure A.1. Fitting of the Angular Dependency Measurement of DI-DBA.

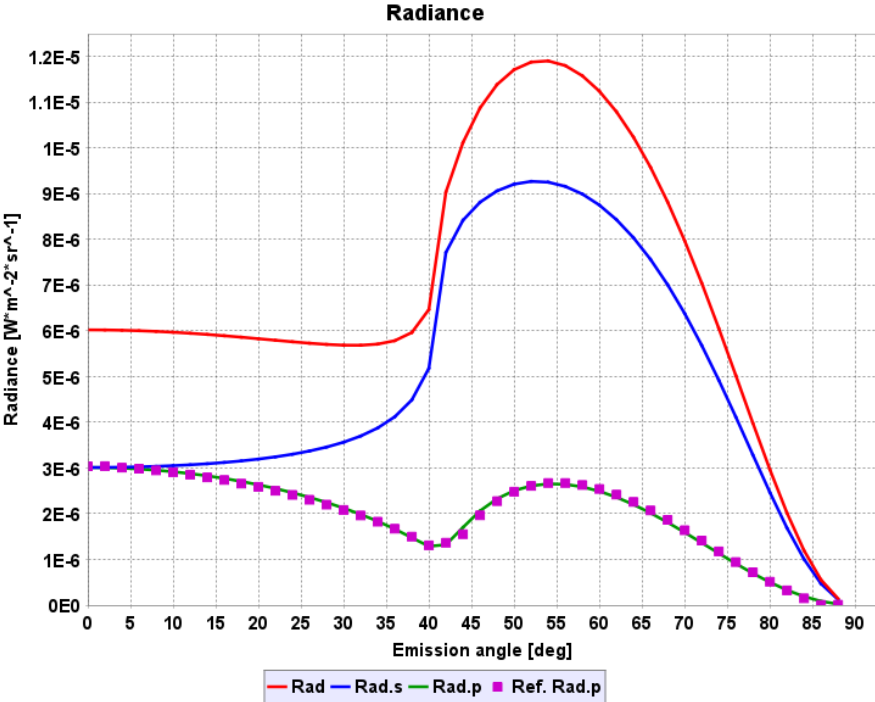


Figure A.2. Fitting of the Angular Dependency Measurement of SpiroAc-DBA.

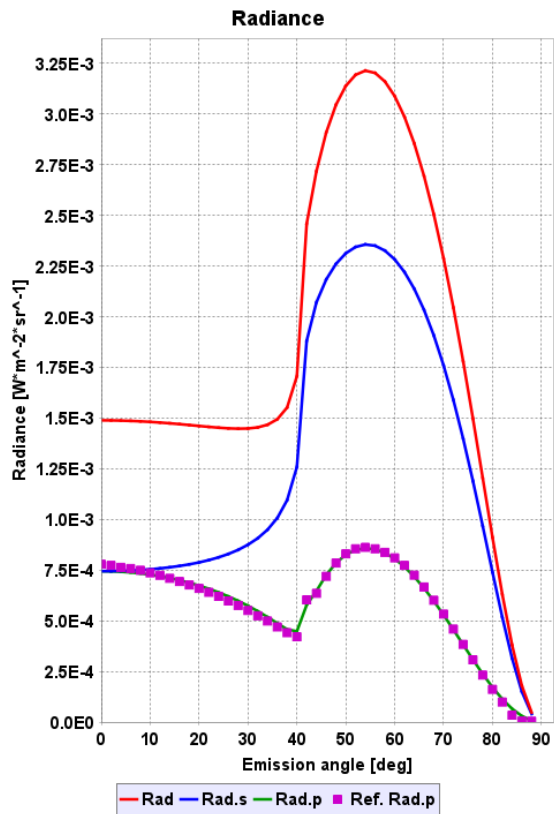


Figure A.3. Fitting of the Angular Dependency Measurement of TMCz-DBA.

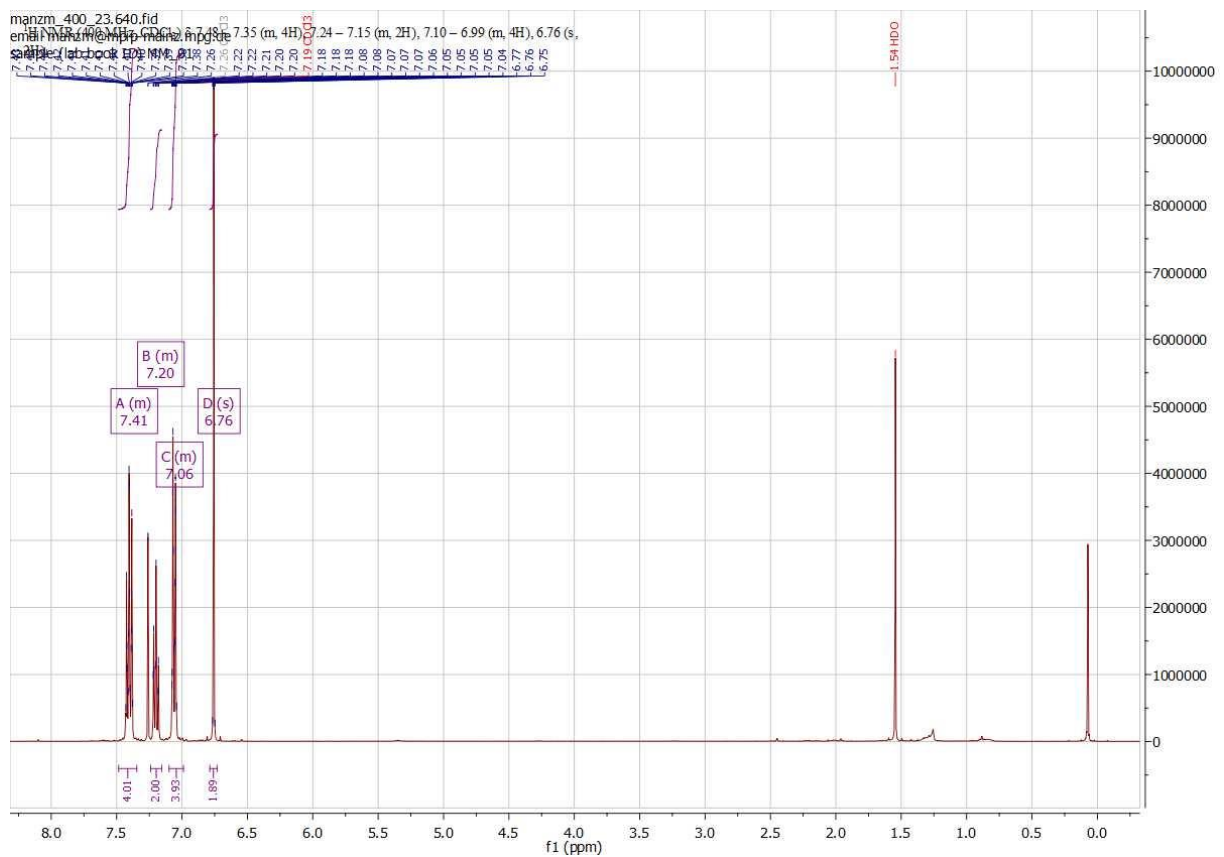


Figure A.4. ¹H-NMR Spectrum of MM01.

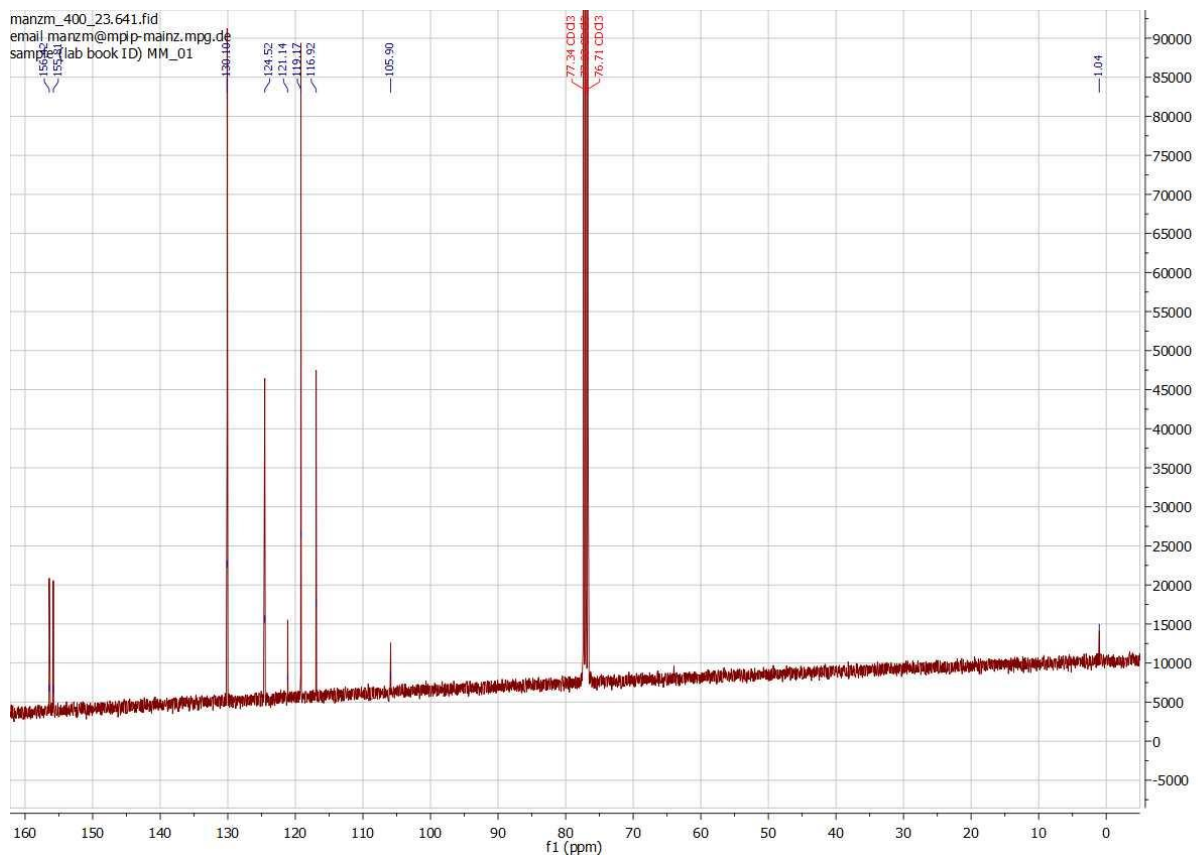


Figure A.5. ¹³C-NMR Spectrum of MM01.

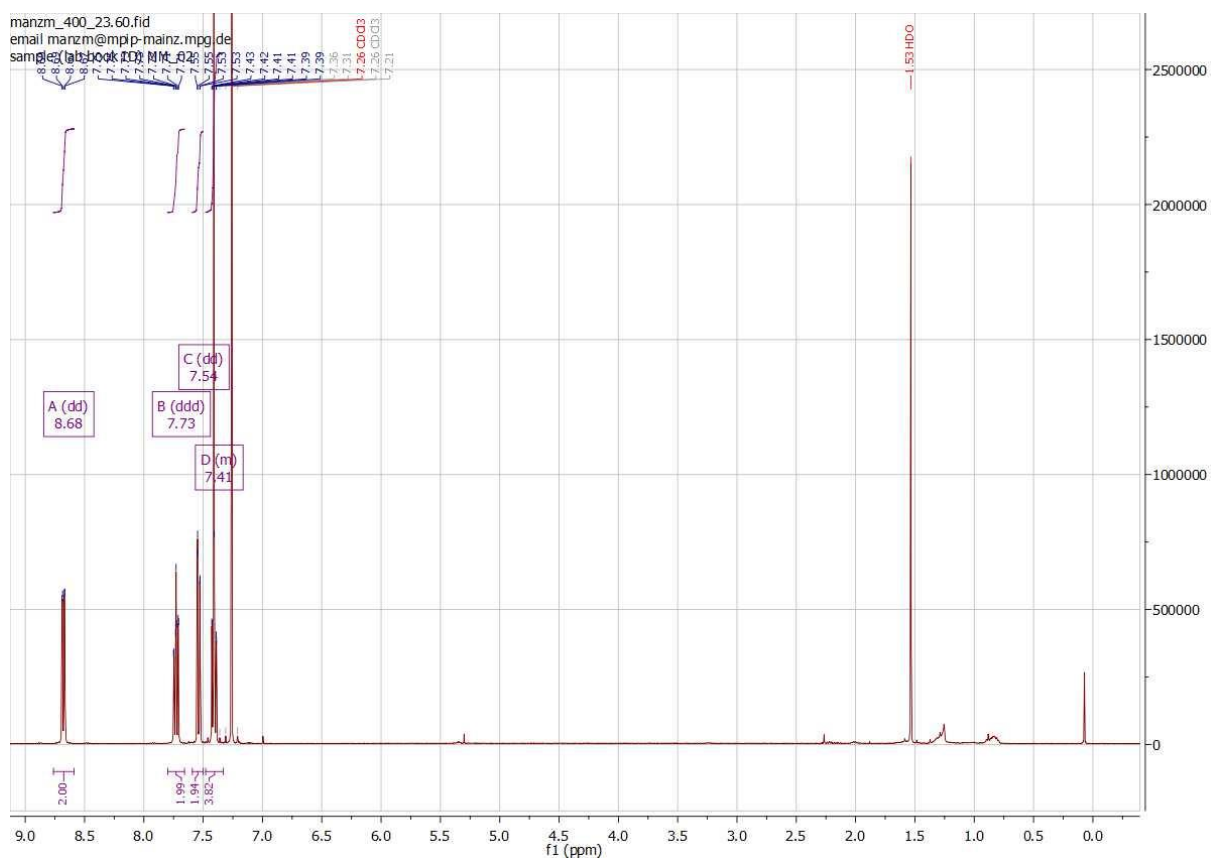


Figure A.6. ¹H-NMR Spectrum of MM02.

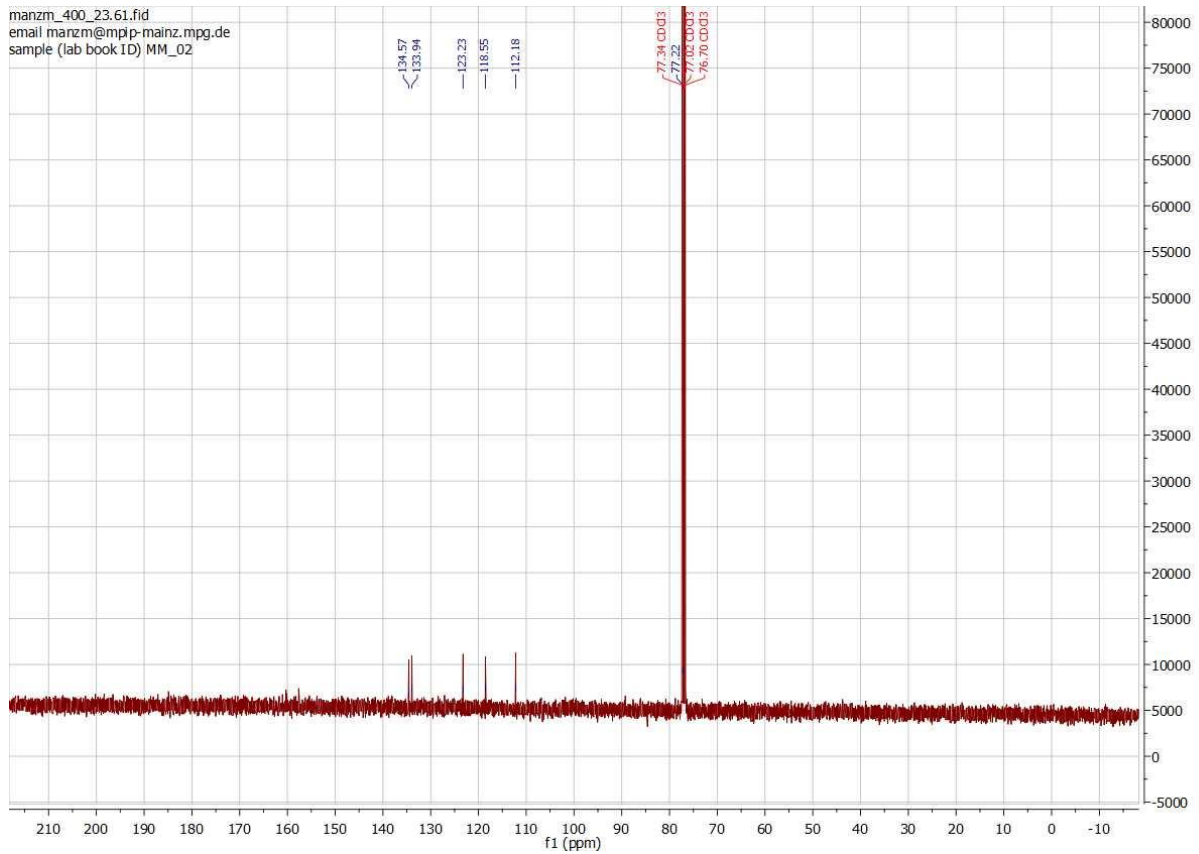


Figure A.7. ¹³C-NMR Spectrum of MM02.

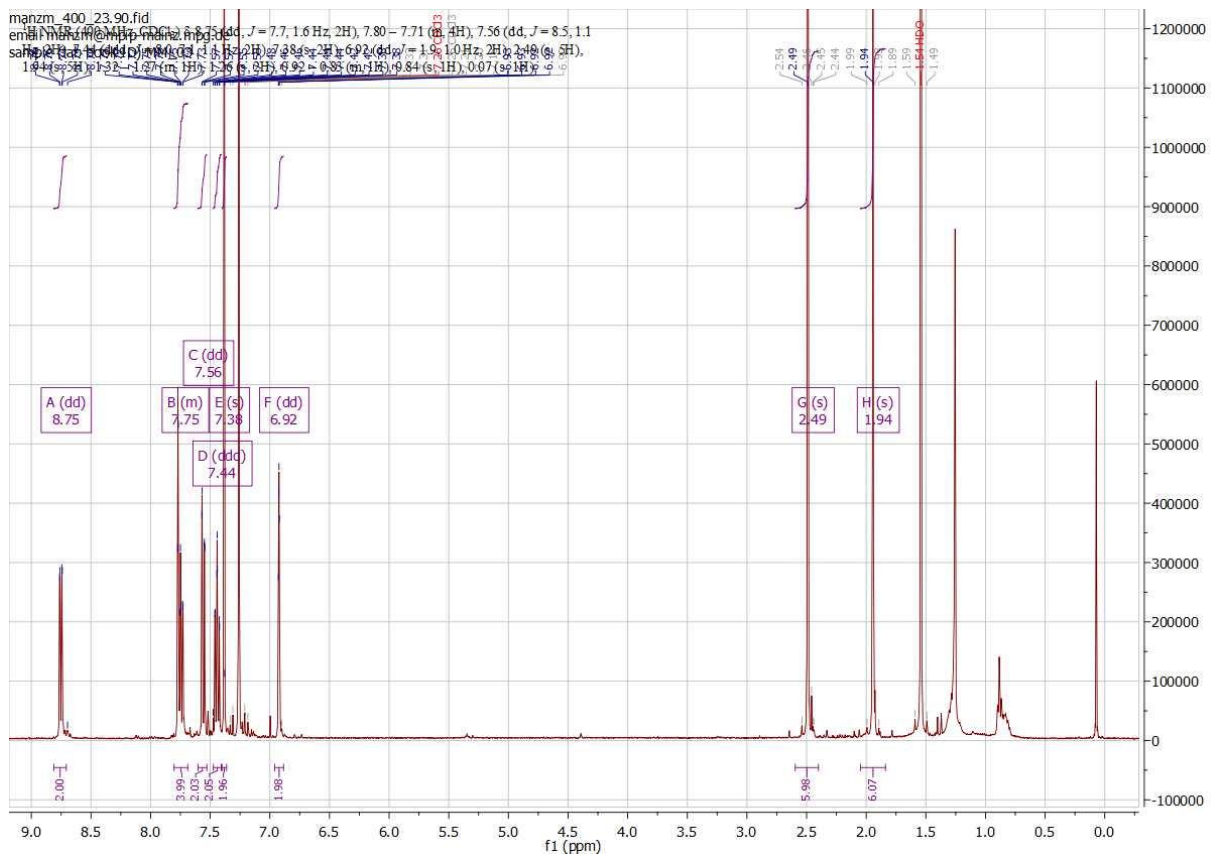


Figure A.8. ¹H-NMR Spectrum of MM03.

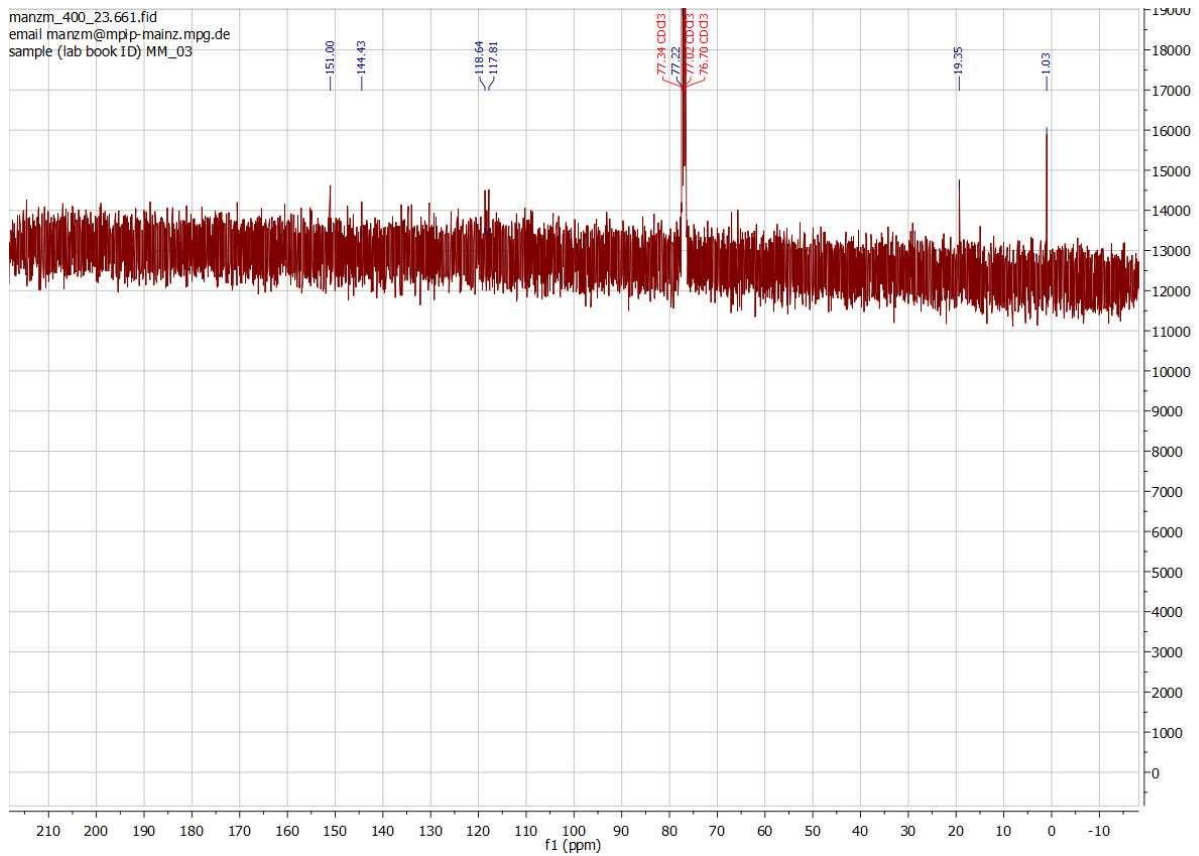


Figure A.9. ^{13}C -NMR Spectrum of MM03.

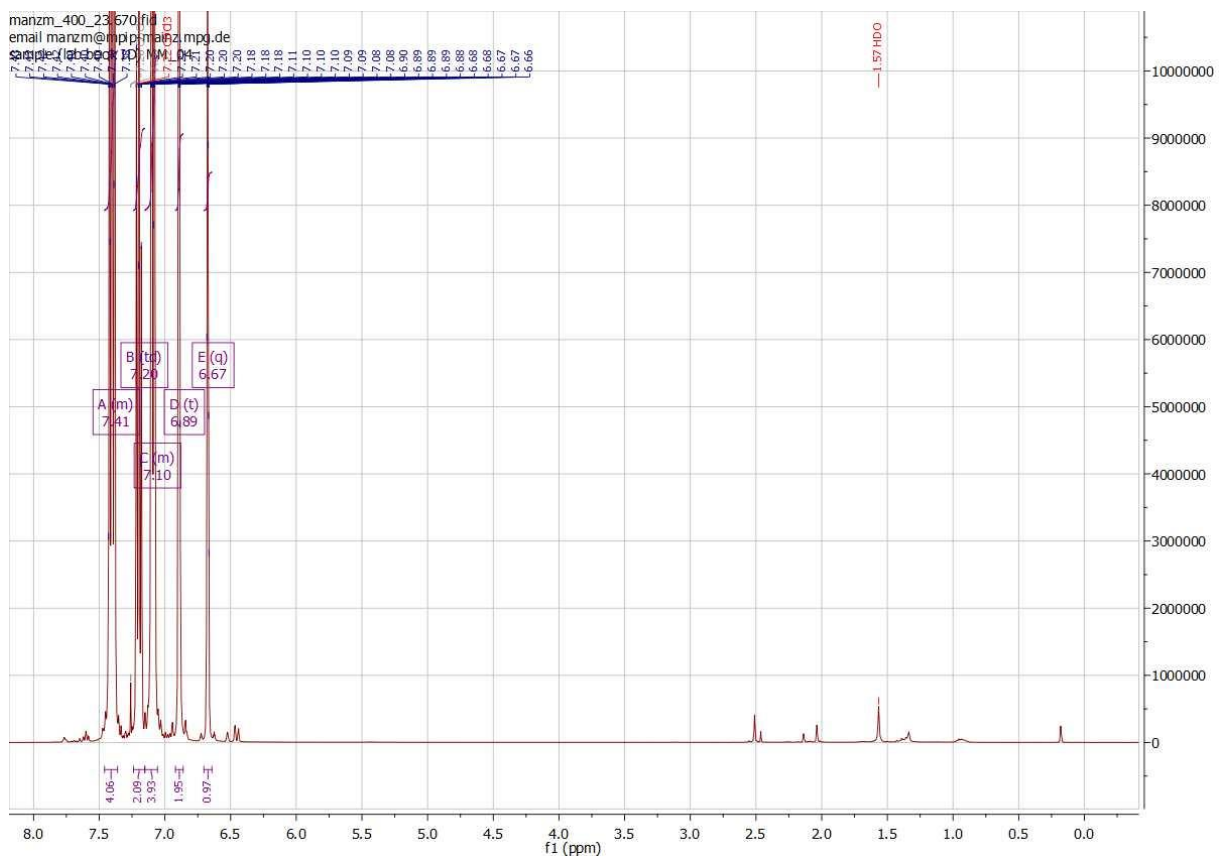


Figure A.10. ^1H -NMR Spectrum of MM04.

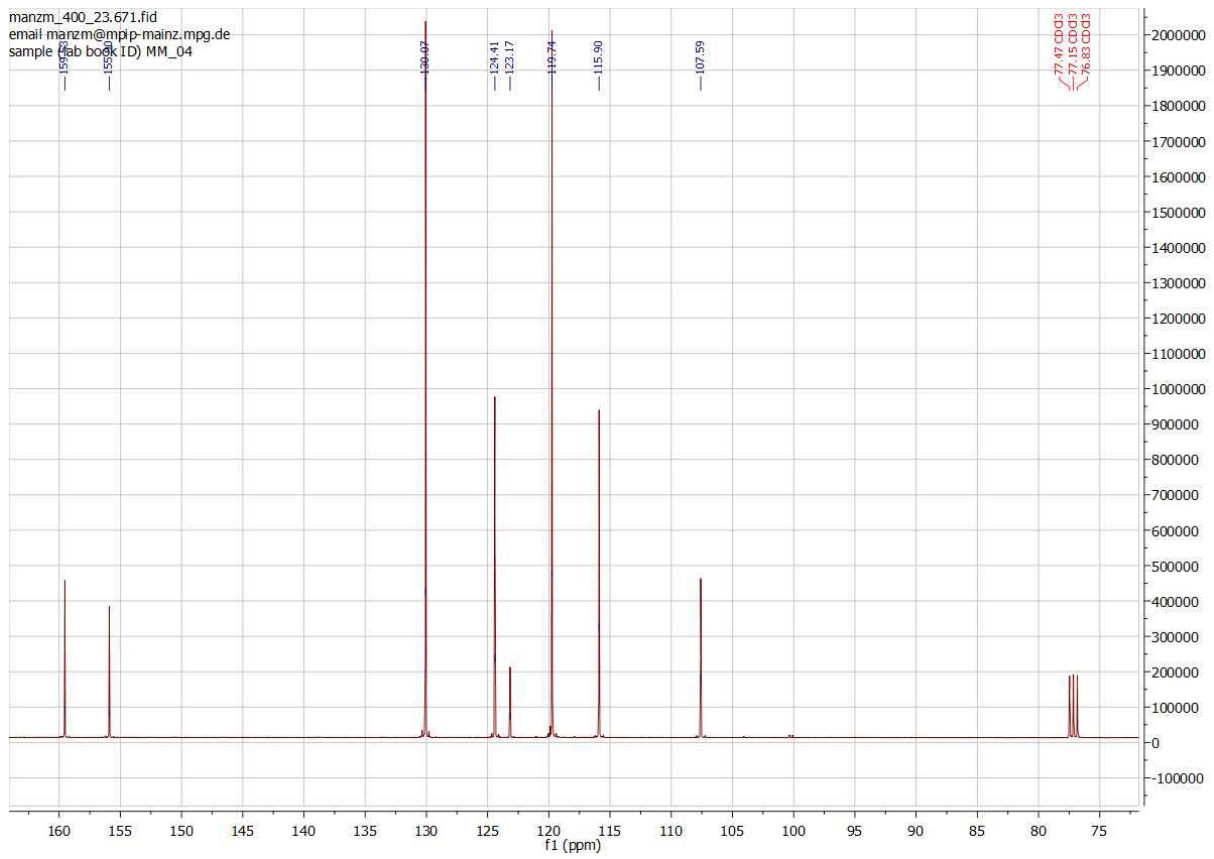


Figure A.11. ¹³C-NMR Spectrum of MM04.

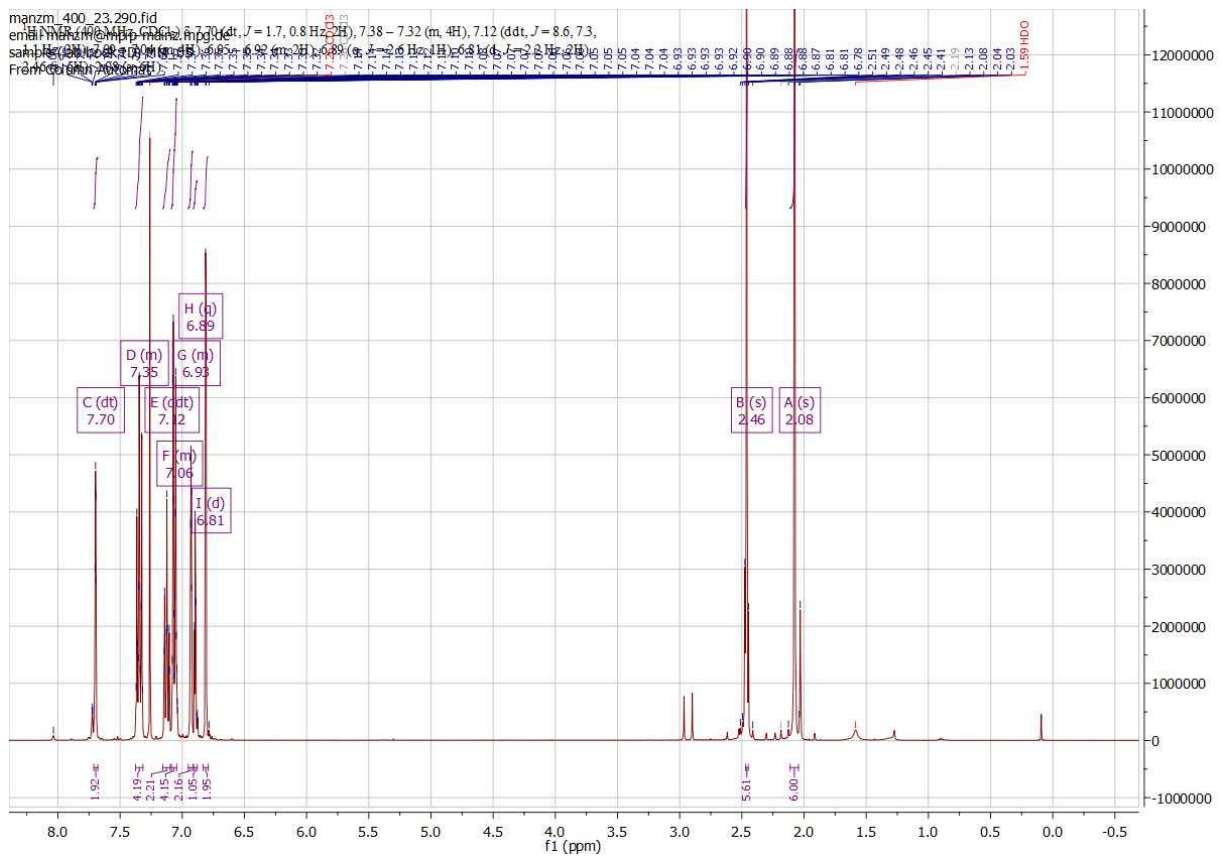


Figure A.12. ¹H-NMR Spectrum of MM05.

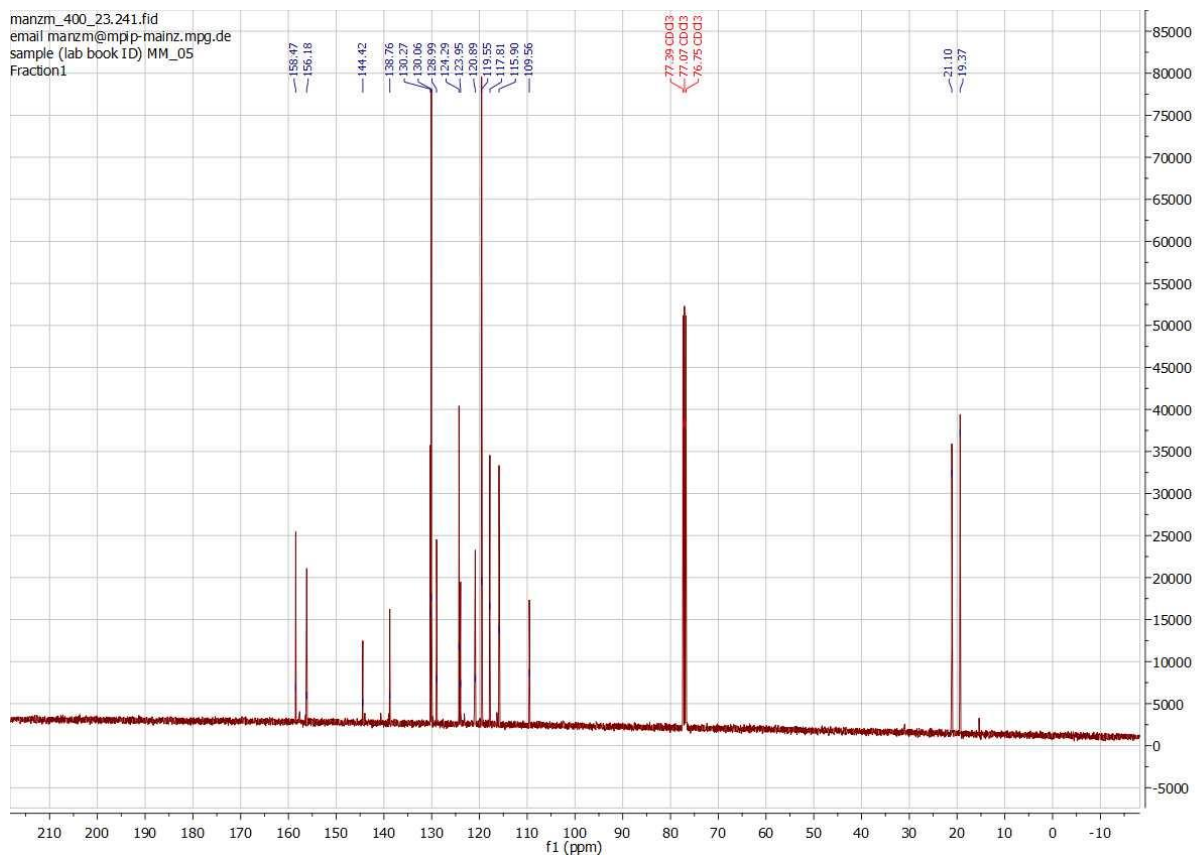


Figure A.13. ¹³C-NMR Spectrum of MM05.

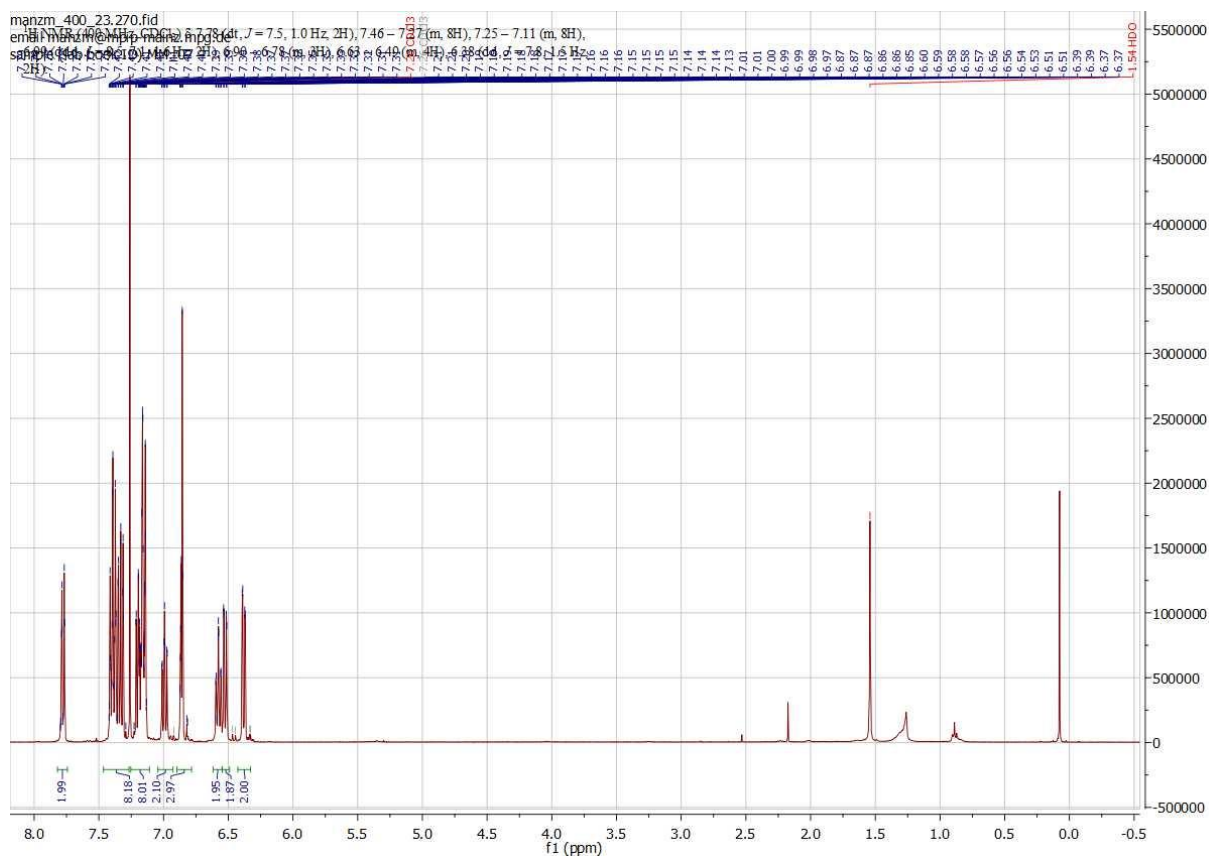


Figure A.14. ¹H-NMR Spectrum of MM06.

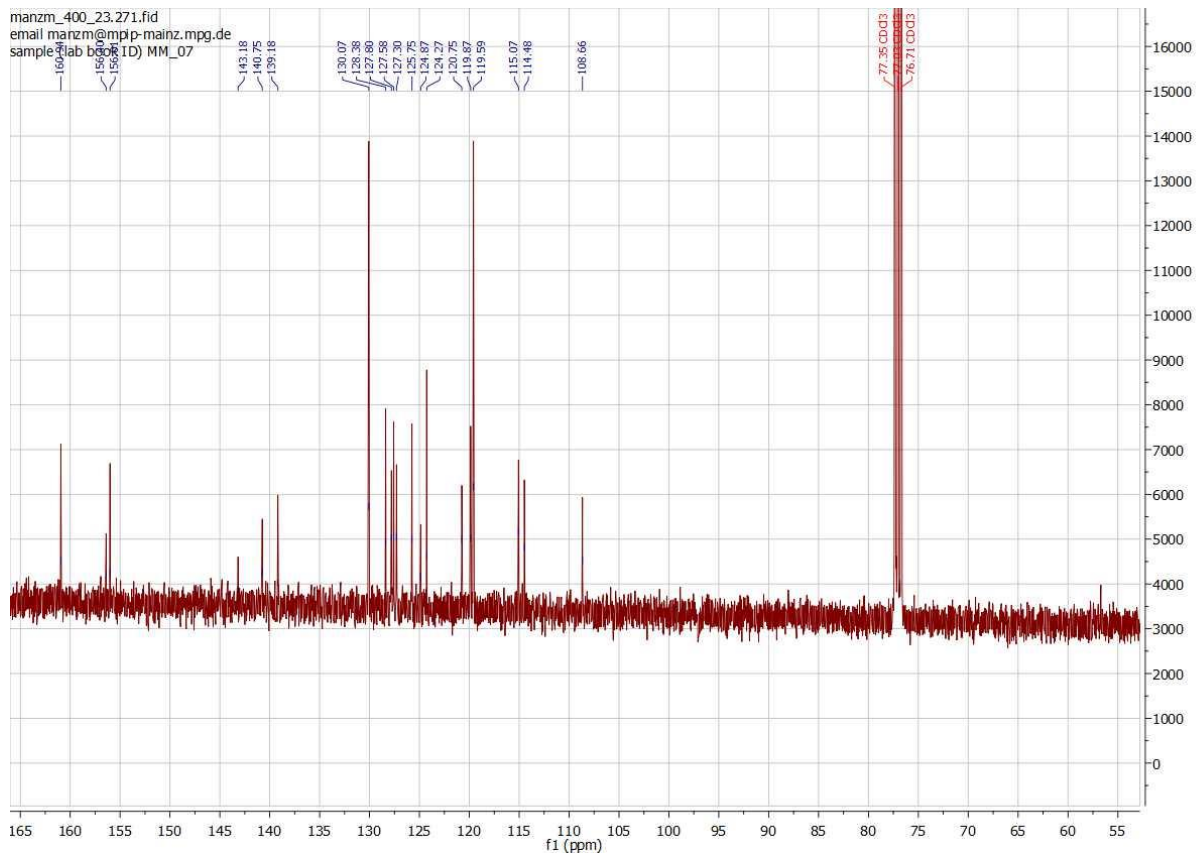


Figure A.15. ^{13}C -NMR Spectrum of MM06.

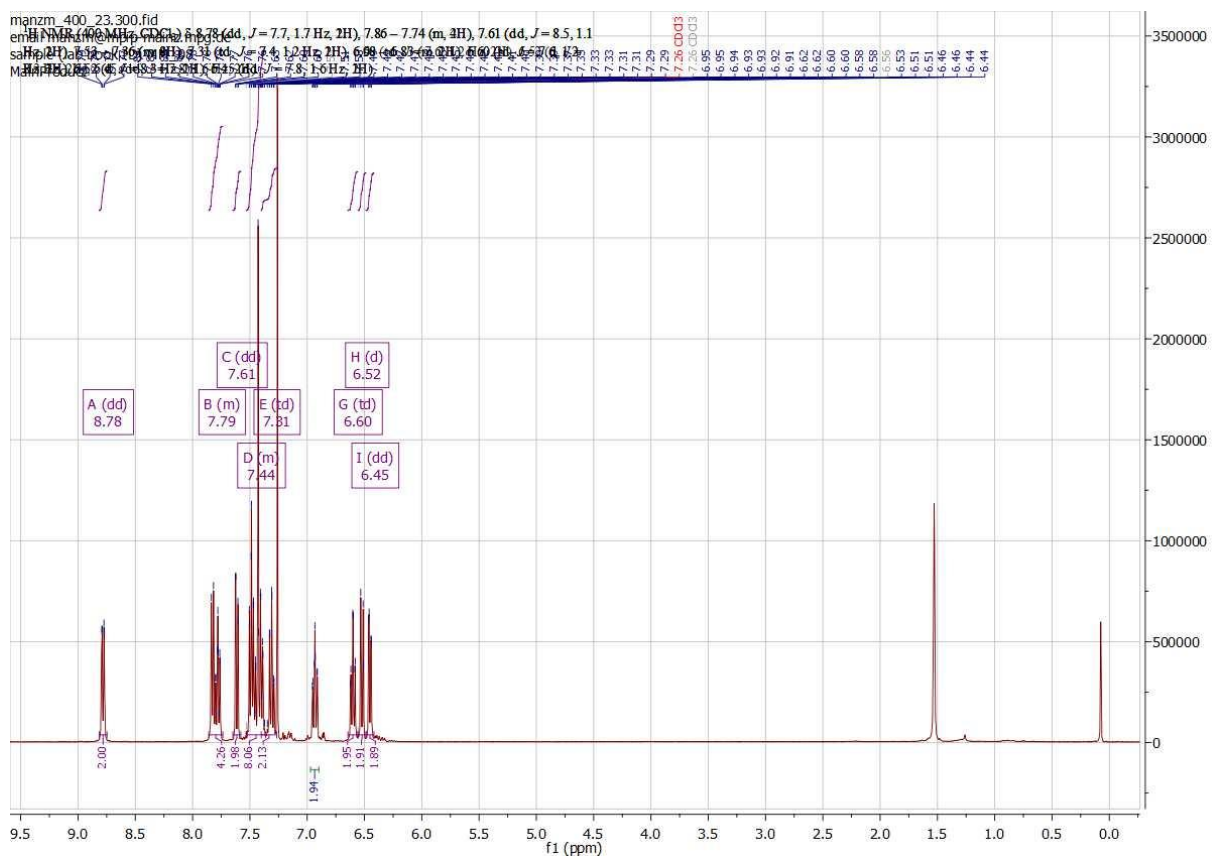


Figure A.16. ^1H -NMR Spectrum of MM07.

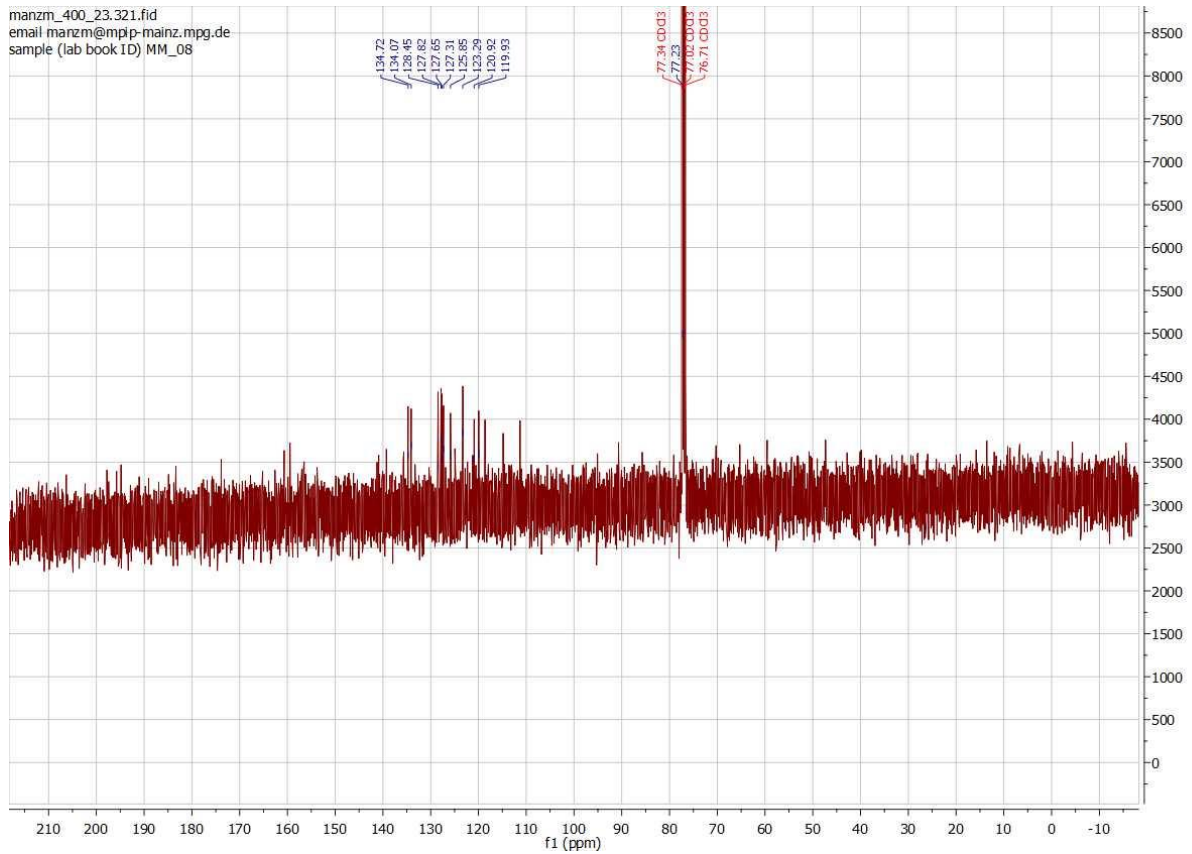


Figure A.17. ^{13}C -NMR Spectrum of MM07.

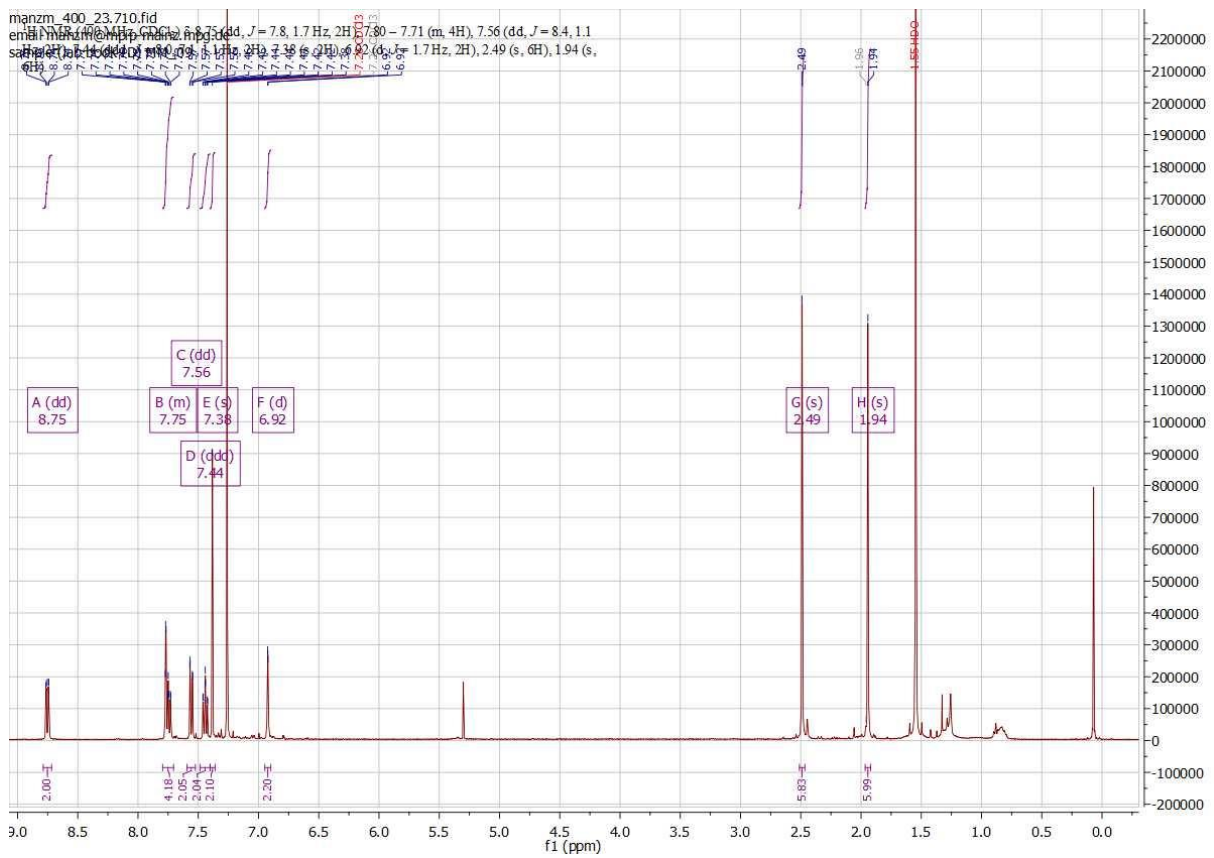


Figure A.18. ^1H -NMR Spectrum of MM08.

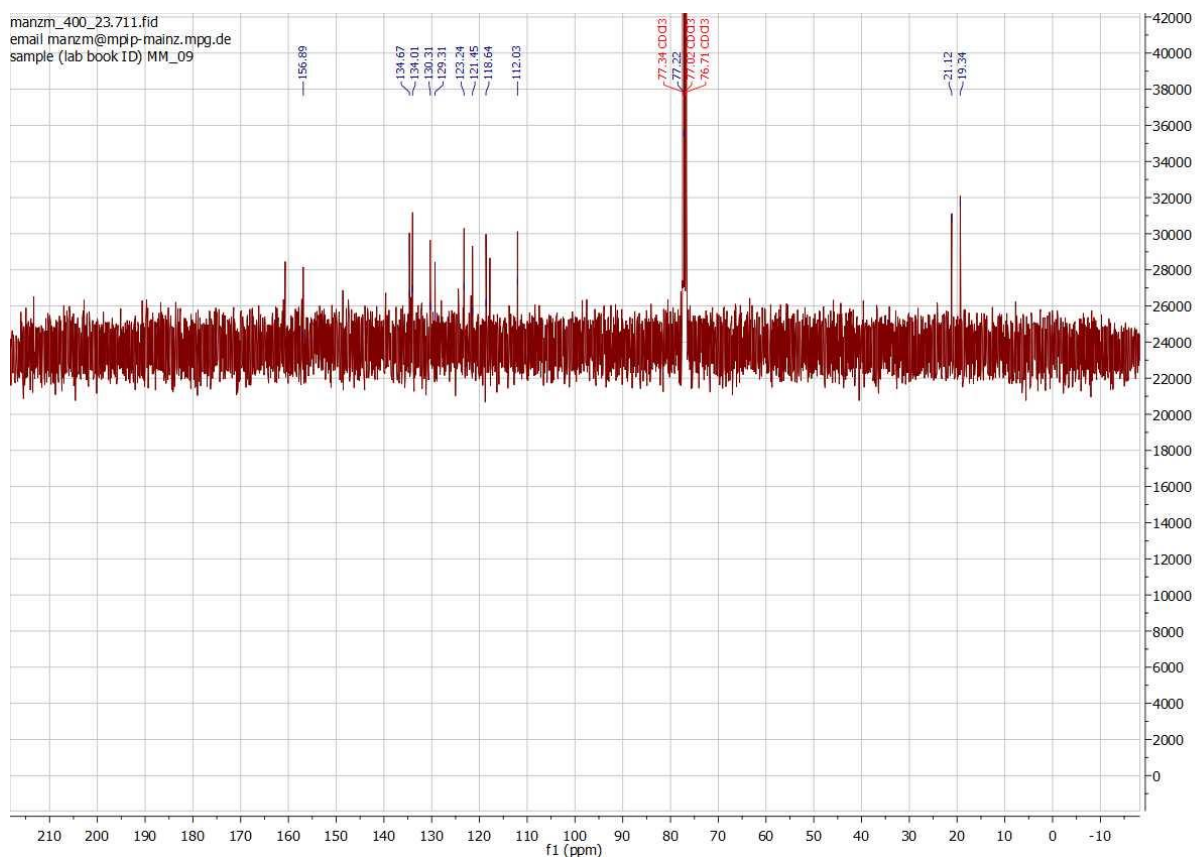


Figure A.19. ^{13}C -NMR Spectrum of MM08.

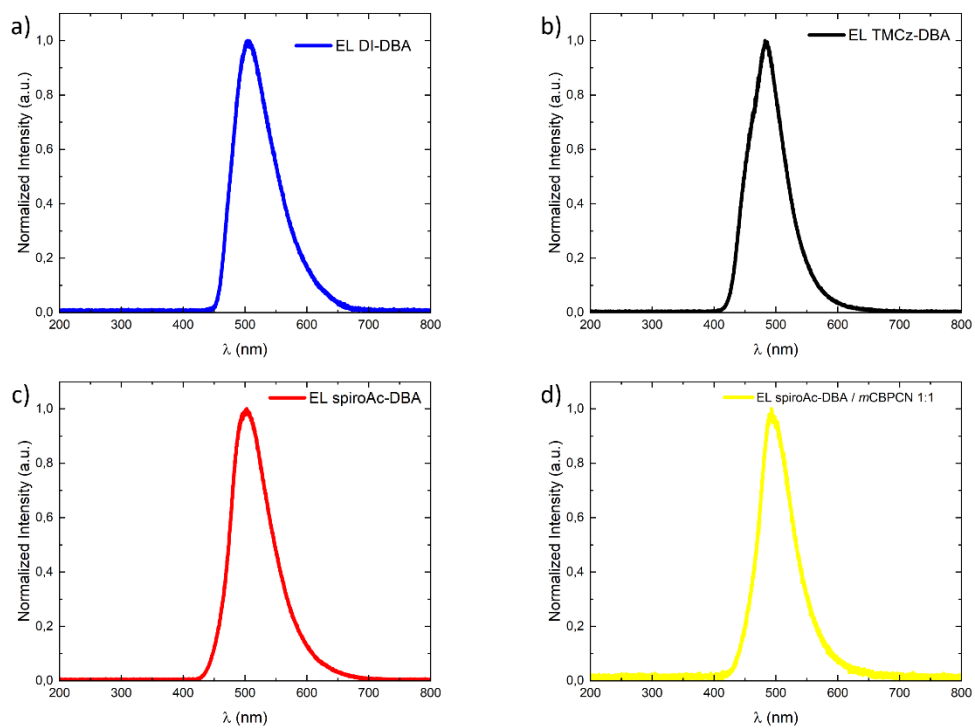


Figure A.20. EL Spectra of a) DI-DBA, b) TMCz-DBA, c) SpiroAc-DBA and d) SpiroAc-DBA/*m*CBP-CN 1:1 in the OLED devices.

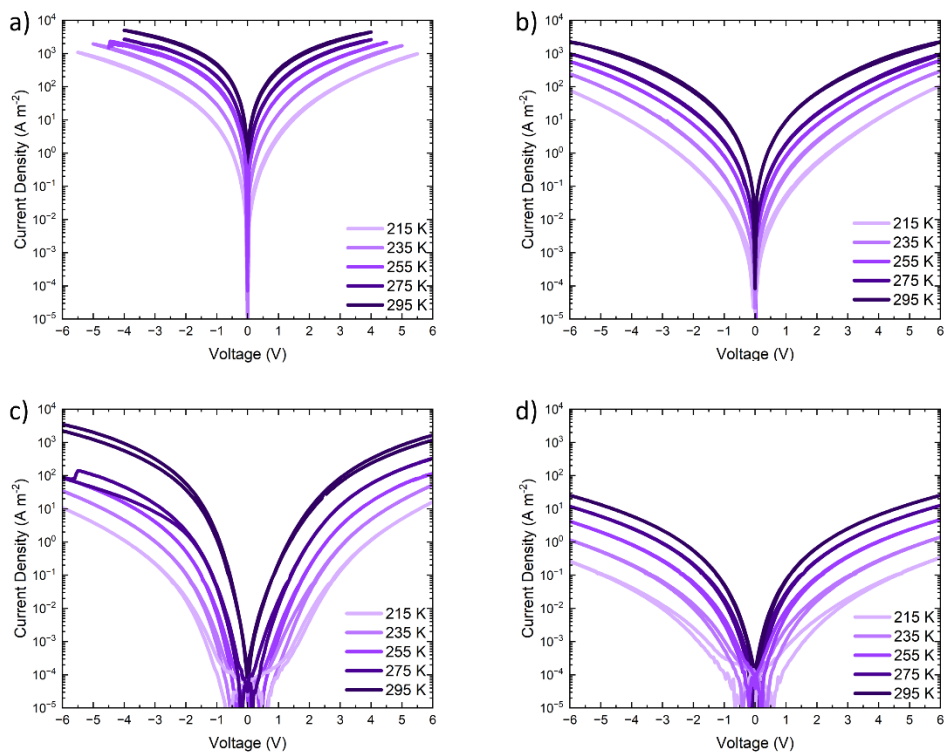


Figure A.21. Temperature-dependent scan of HO devices of a) DI-DBA, b) TMCz-DBA, c) SpiroAc-DBA and d) SpiroAc-DBA/mCBP-CN 1:1.

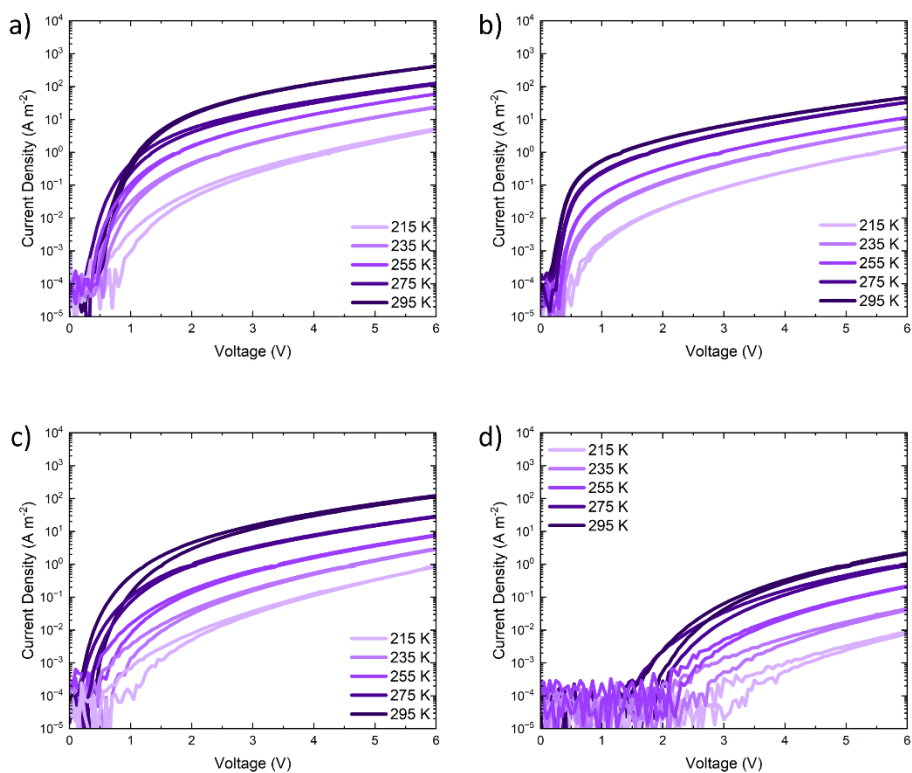


Figure A.22. Temperature-dependent scan of EO devices of a) DI-DBA, b) TMCz-DBA, c) SpiroAc-DBA and d) SpiroAc-DBA/mCBP-CN 1:1.

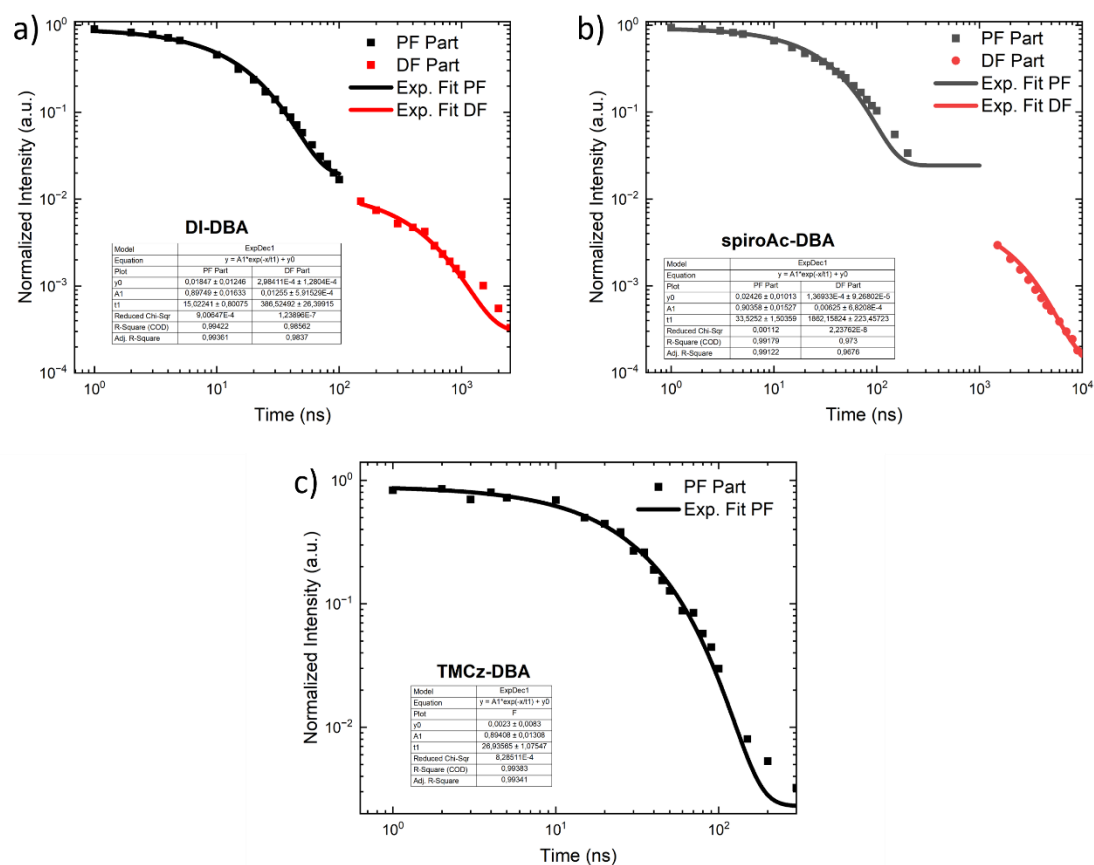


Figure A.23. TRPL Plots of a) DI-DBA, b) SpiroAc-DBA and c) TMCz-DBA.

11. Deutsche Zusammenfassung

Heutzutage finden Organische Leuchtdioden (OLEDs) vielseitigen Einsatz in Bildschirmen von Smartphones, Flachbildschirmen, aber auch in Festkörperbeleuchtungstechniken und sind daher aus unserem Alltag nicht mehr wegzudenken. Im Vergleich zur Flüssigkristallbildschirm-Technologie (LCD) weisen OLEDs mehrere Vorteile auf: Die Pixel eines OLED-Bildschirms sind selbstleuchtend. Daher ist keine Hintergrundbeleuchtung wie bei einem LCD-Bildschirm erforderlich. Dies führt nicht nur zu einem geringeren Stromverbrauch, sondern auch zu einem höheren Kontrast und einer besseren Farbreinheit.^[2] Außerdem werden OLEDs umweltfreundlicher und billiger als LCD-Bildschirme hergestellt.^[3]

Um mit LCDs konkurrieren und diese letztlich sogar übertreffen zu können, hat die OLED-Forschung einen langen Weg zurückgelegt: Die bei herkömmlichen fluoreszenzbasierten OLEDs auf 25 % begrenzte interne Quantenausbeute (IQE) ist eine intrinsische Eigenschaft und folgt daraus, dass bei elektrischer Anregung nur eine von vier Anregungen zu einem Singulett-Exziton führt, das dann in Photonen und somit zur Lichterzeugung genutzt werden kann.^[8,9] Die übrigen 75 % der elektrisch erzeugten Energie werden als Wärme abgeleitet und gehen daher verloren. Daher hat die Entwicklung von phosphoreszierenden Emittern die Effizienz der Bauelemente erheblich verbessert.^[10] Die Verwendung von phosphoreszierenden Emittern, die Schwermetalle (Ir, Pt, Os und Au) in den organischen aromatischen Gerüsten enthalten, verbessert das Intersystem-Crossing (ISC) durch die starke Spin-Bahn-Kopplung (SOC).^[9,11] Dadurch lassen sich nicht nur Singulett-Exzitonen, sondern auch Triplett-Exzitonen nutzen, was zu IQEs von bis zu 100% führt.^[11,12] Dies ist jedoch mit dem großen Nachteil verbunden, dass die Schwermetalle teuer und weltweit nur begrenzt verfügbar sind. Um diese Herausforderung zu bewältigen, wurden rein organische aromatische Verbindungen mit einer kleinen Energielücke ΔE_{ST} zwischen dem niedrigsten Singulett- und Triplett-Zustand als Emitter verwendet.^[16] Auf diese Weise lassen sich nicht-strahlende Triplett-Exzitonen durch einen Reverse-Intersystem-Crossing-Prozess (rISC), der durch thermische Energie aus der Umgebung unterstützt wird, in emittierende Singulett-Exzitonen umwandeln. Dies wird als thermisch aktivierte verzögerte Fluoreszenz (engl. Thermally Activated Delayed Fluorescence TADF) bezeichnet und ermöglicht die Herstellung kostengünstiger OLEDs, die auch einen IQE von bis zu 100 % erreichen können, ganz ohne den Einsatz von teuren und begrenzten Ressourcen.^[16]

Herkömmliche mehrschichtige OLED-Bauelemente sind aus Gründen der Stabilität und Effizienz weit verbreitet.^[21] Allerdings sind, wie es der Name bereits impliziert, in einem solchen Bauelement viele verschiedene Schichten enthalten, was auch zu höheren Kosten und längerer Produktionszeit führt. Um dem entgegenzuwirken hat unsere Gruppe eine effiziente und langlebige OLED auf der Grundlage des TADF-Materials 5,10-Bis(4-(9*H*-carbazol-9-yl)-2,6-dimethylphenyl)-5,10-dihydroboranathrene (CzDBA) in einer unkonventionellen einschichtigen Bauelement-Konfiguration hergestellt.^[26] Um daran anknüpfen zu können, ist ein umfassendes Verständnis der Auswirkungen von Moleküldesign auf die photophysischen sowie die Geräteigenschaften essentiell: Die Analyse von Struktur-Eigenschafts-Beziehung (Photophysik und Geräteleistung) ist unerlässlich. Zu diesem Zweck werden in dieser Arbeit ebenfalls ausschließlich einschichtige OLEDs fabriziert und analysiert.

Da in jüngster Zeit besonders elektronen-defizitäre Bor-Akzeptoreinheiten in TADF-Materialien aufgrund ihrer ausgezeichneten photophysikalischen und elektrochemischen Eigenschaften und ihres elektronenaufnehmenden Charakters erforscht wurden, wird in dieser Arbeit daran angeknüpft: Ziel dieser Arbeit ist die Analyse dreier Moleküle, die aus der gleichen Akzeptoreinheit mit dreifach koordiniertem Boratom aufgebaut sind. Dies reicht von der Synthese bis hin zur Untersuchung der Struktur-Eigenschafts-Beziehungen, sowohl in Bezug auf die Photophysik als auch die Leistung in einer OLED. Alle drei Moleküle sind blaue Emitter und weisen denselben 5-(5,9-Dioxa-13*b*-boranaphtho[3,2,1-*de*]anthracen-7-yl)-(Dioxaboraanthracen DBA)-Akzeptoranteil auf.

Abbildung 11.1 zeigt die chemischen Strukturen der drei untersuchten Materialien: 5-(5,9-dioxa-13*b*-boranaphtho[3,2,1-*de*]anthracen-7-yl)-10,15-diphenyl-10,15-dihydro-5*H*-diindolo[3,2-*a*:3',2'*c*]carbazol (DI-DBA), 10-(5,9-Dioxa-13*b*-boranaphtho[3,2,1-*de*]anthracen-7-yl)-10*H*-spiro[acridin-9, 9'-Fluoren

(SpiroAc-DBA) sowie 9-[1,4]Benzoxaborino[2,3,4-*kl*]phenoxaborin-7-yl-1,3,6,8-tetramethyl-9*H*-carbazol (TMCz-DBA). Durch Variation des Donoranteils bei gleichzeitiger Beibehaltung des Akzeptoranteils lassen sich die Auswirkungen der Donorstruktur auf die HOMO- und LUMO-Niveaus, die photophysikalischen Eigenschaften sowie auf die Ladungstransport-Eigenschaften und die Leistung der Bauelemente untersuchen.

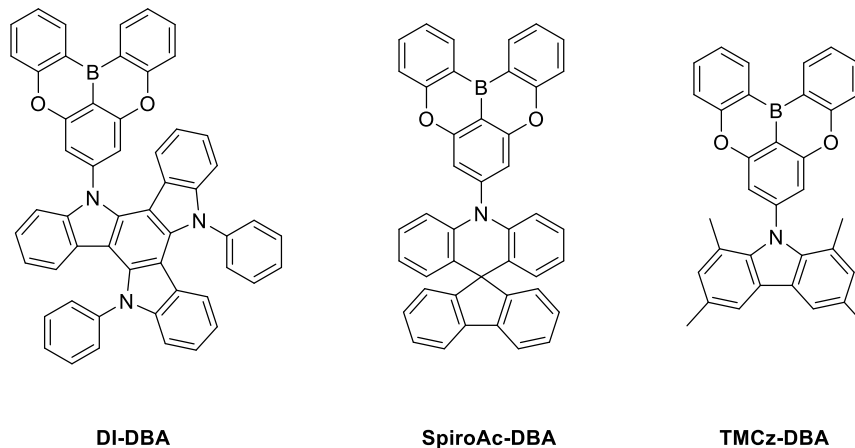


Abbildung 11.1. Zielmoleküle DI-DBA, SpiroAc-DBA and TMCz-DBA.

TD-DFT-Berechnungen (zeitabhängige Dichtefunktionstheorie, engl. Time-dependent density function theory) wurden für diese drei Moleküle durchgeführt, um Einblicke in die HOMO- und LUMO-Ebenen sowie die Energielücke zwischen dem niedrigsten angeregten Singulett- und Triplett-Zustand ΔE_{ST} zu erhalten.

Die ermittelten HOMO-Energien deuten darauf hin, dass der Transport von positiven Ladungsträgern (Elektronenlöchern) nicht durch Elektronenloch-Fallen limitiert ist. Die LUMO-Energien hingegen legen nahe, dass der Transport von negativen Ladungsträgern (Elektronen) durch Fallen begrenzt sein wird. Die DFT-Berechnungen haben für alle drei Emitter niedrigen ΔE_{ST} -Werte (<0.1 eV) gezeigt. Daher ist durch thermische Aktivierung für die Moleküle ein effizienter *reverse intersystem crossing* (rISC) Prozess möglich, was die Moleküle zu vielversprechenden Kandidaten für das TADF-Phänomen macht. Die photophysikalischen Untersuchungen von Dünnschichtproben zeigten, dass TMCz-DBA Licht im tiefblauen Bereich emittiert, während SpiroAc-DBA und DI-DBA himmelblaue Emitter sind. Um den photolumineszenten Zerfall der Emitter zu analysieren, wurden zeitaufgelöste Photolumineszenzspektren (engl. Time-Resolved Photoluminescence TRPL) der Filmproben gemessen. Diese zeigten die längste Lebensdauer für das SpiroAc-DBA, bei dem auch noch nach $50 \mu\text{s}$ ein nachweisbares Signal erhalten wurde. Dies zeigt die verzögerte Fluoreszenz des Materials, die auf Zeitskalen im μs -Bereich stattfindet, während die prompte Fluoreszenz deutlich schneller auf Zeitskalen im ns-Bereich abläuft. Die Lebensdauern der prompten und verzögerten Fluoreszenz wurden durch Anpassung der prompten und verzögerten Fluoreszenzanteile an zwei separate exponentielle Zerfallskurven abgeleitet: Diese zeigten sowohl für prompte als auch für verzögerte Fluoreszenz die höchste Lebensdauer für SpiroAc-DBA unter den drei verschiedenen Emittern mit 34 ns bzw. $1,86 \mu\text{s}$.

Um die horizontale Dipolorientierung zu bestimmen, wurden winkelabhängige Emissions-Messungen durchgeführt. Diese ergaben besonders hohe horizontale Dipolorientierungen mit 83 % für DI-DBA und 78 % für SpiroAc-DBA. Dies ist ebenfalls ein Indiz dafür, dass es sich bei den Materialien um vielversprechende Emitter für die Anwendung in OLEDs handelt: Eine hohe horizontale Orientierung

der emittierenden Übergangsdipolmomente kann die Effizienz der Lichtauskopplung erhöhen und somit auch die Effizienz der OLED.

Ein wichtiger Faktor bei der Bestimmung der Effizienz einer OLED-Vorrichtung ist die Untersuchung des Gleichgewichts des Ladungstransports. Im Idealfall sollten Elektronenlöcher und Elektronen bei gleicher Spannung eine ähnliche Stromdichte aufweisen; der Ladungstransport für Löcher und Elektronen sollte ausgeglichen sein. Bei allen Proben war jedoch der Löchertransport um mindestens eine Größenordnung höher als der Elektronentransport und daher der Ladungstransport nicht ausgeglichen.

Schließlich wurden die einschichtigen OLEDs hergestellt und analysiert, um die Struktur-Eigenschafts-Beziehungen zu verstehen. Es wurde festgestellt, dass die OLED mit DI-DBA die niedrigste Einschaltspannung von 2,3 V sowie die niedrigste Betriebsspannung von nur 2,8 V zeigt. Außerdem erzielte sie die beste Effizienz und ist somit in der einschichtigen OLED-Bauweise der vielversprechendste Emitter.